ASSESSMENT OF TIME REVERSAL METHODS USED FOR RF HYPERTHERMIA IN CANCER TREATMENT

A Dissertation

Presented to

the Faculty of the Department of Electrical and Computer Engineering

University of Houston

In Partial Fulfillment

of the Requirements for the Degree

Doctor of Philosophy

in Electrical Engineering

By

Kuang Qin

August 2017

ASSESSMENT OF TIME REVERSAL METHODS USED FOR RF HYPERTHERMIA IN CANCER TREATMENT

Kuang Qin

Approved:

Co-Chair of the Committee
Jarek Wosik, Research Professor,
Electrical and Computer Engineering

Co-Chair of the Committee
David R. Jackson, Professor,
Electrical and Computer Engineering

Committee Members:

Ji Chen, Professor,
Electrical and Computer Engineering

John H. Miller, Jr., Professor,
Physics

Steven M. Anlage, Professor,
Physics,
University of Maryland

Suresh K. Khator, Associate Dean,
Cullen College of Engineering

Badrinath Roysam, Professor and Chair,
Electrical and Computer Engineering

Acknowledgement

This dissertation work would not have been able to conclude without the guidance and the help of many individuals who have directly or indirectly extended their valuable contributions. I am grateful to all of those with whom I have had the pleasure to work during this and other related projects.

First of all, I would like to extend my heartfelt gratitude to my advisor, Dr. Jarek Wosik, for his supervision, encouragement, and support during the progression of my Ph.D. work. As my teacher and mentor, he has not only shared his valuable perceptions in relevance to the research, but also trained me in technical and experimental skills, problem solving abilities, and interdisciplinary ways of thinking.

I am feeling lucky to receive helpful suggestions from my committee members in different research areas in which they are expert. I am highly obliged to Dr. Steven M. Anlage for his friendly reception and for the access to the equipment during my stay at University of Maryland to complete the experimental part of my research work. In addition, he provided me a different perspective with enlightening ideas to look at my research project. I am grateful to Dr. David Jackson for his remarkable insights into the analytical model part. He proved to be a reckoner in solving my theoretical and scientific problems during the research. I express my sincere appreciations to Dr. Ji Chen and Dr. John H. Miller for serving on my committee.

I would also like to thank Ms. Min Zhou from Dr. Anlage's group from University of Maryland who aided me greatly in the experimental part of this research, and Dr. Bo Xiao, from Dr. Anlage's group as well, whose preliminary work were really noteworthy. I genuinely appreciate Ms. Xinyue Zhang's help with the literature search and the formatting

of the dissertation. I am grateful to all my colleagues for their perceptive comments and constructive criticisms throughout my graduate program at the University of Houston.

Last but not least, I would like to express my utmost indebtedness to my family members who have always been supportive. With your love, encouragement, and guidance, I learned to be a better man that can bring inspiration and happiness to others.

ASSESSMENT OF TIME REVERSAL METHODS USED FOR RF HYPERTHERMIA IN CANCER TREATMENT

An Abstract

of a

Dissertation

Presented to

the Faculty of the Department of Electrical and Computer Engineering

University of Houston

In Partial Fulfillment

of the Requirements for the Degree

Doctor of Philosophy

in Electrical Engineering

By

Kuang Qin

August 2017

Abstract

Radio frequency (RF) hyperthermia, for which cell temperatures are increased to 41-45 °C, is a well-recognized method for treatment of malignant tumors. However, it suffers from the lack of spatial selectivity towards the target when non-invasive external sources are used. An optimized hyperthermia method, time reversal (TR) technique, is introduced to enhance specific heating on the target while reducing the non-specific heating elsewhere.

TR is applied to electromagnetics (EM) recently due to its intrinsic temporal and spatial focusing properties coming from the linear reciprocity of the Maxwell's equations. It utilizes the time reversal mirror (TRM) to record the EM waves emitted from a source and reemit the time-reversed version back to the source. By collecting the scrambled information dispersed in the reflection and scattering, the original source signal is rebuilt and a high-intensity focusing is observed at the source location. Owing to its focusing properties, EM TR has been applied in areas such as wireless communication and geophysics. In this dissertation the possible application of TR in hyperthermia is assessed and investigated.

A simple analytical model is proposed to analyze the TR problem in a pure EM way. The model converts the spatial focusing problem into a constrained optimization based on an asymptotic study and provides information for the choices of signal types, frequencies, bandwidths, and number of antennas.

In addition, two non-invasive focusing methods are discussed. The first approach is to mark the target with an active virtual source. The real signals used for selective heating are obtained from the simulation on the personalized permittivity map generated from MRI

and CT. The other way is to place one or more passive nonlinear element, such as a ferromagnetic material, instead of an active source to spatially encode the tumor location. The feasibility of these two methods is evaluated by simulations in CST MICROWAVE STUDIO® for a reverberating system. The follow-up experiments conducted in the same environment clearly demonstrates the intensity and selectivity of the heating effects from the EM TR techniques.

Table of Contents

List of Figures

List of Tables

Chapter 1 Introduction

The World Health Organization (WHO) reports that cancer caused 8.8 million death in 2015 and predicts that in 2035 the death number will increase to more than 14 million [1]. Cancer is the second major cause of death worldwide, surpassed only by ischemic heart disease and stroke. The research reported by the International Agency for Research on Cancer (IARC) shows that, in 2012, the total number of cancer incidents was more than 14 million [2], among which the most common cases in males were lung cancers. Lung cancer is the biggest killer among all cancer. Approximately 25 percent cancer deaths are from lung cancer, more than the sum of deaths caused by colon, breast, and prostate cancers [3]. The diagnosis rate for lung cancer at an early stage is only 16 percent [4]. Given the fact that the lung is too sophisticated to undergo frequent surgeries, it is indispensable to innovate non-invasive methods in cancer diagnosis and therapeutics.

The traditional cancer treatment offers a combination of surgery, radiotherapy and chemotherapy, which aims to cure or prolong life, while reducing suffering of cancer patients. However, these therapeutic modalities barely increase the survival rate [5]. Instead, the patients probably suffer from the painful side effects. The low survival rate of cancers results from the following: (i) the difficulties in diagnosis and prognosis for neoplasms. Mostly the malignant tumor cells are seated deep from the skin, which are hard to be spotted and targeted; (ii) the genetic diversity of cancers. The therapeutic modality should be specific and feasible to each individual even with the same cancer; (iii) The drug resistance properties of the cancer stem cells [6], which means they can prevent themselves from anticancer agents, at the same time the anticancer drugs are able to potentially damage the healthy cells.

The last couple of decades have witnessed the rapid development of cancer treatment. Thermal therapy, specifically hyperthermia, is generally combined with radiation therapy and chemotherapy to treat cancer [7, 8]. In this method, the stem cancer cells are heated by external sources over a threshold temperature for a period of time. The purpose of hyperthermia is to kill or damage cancer cells and sensitize the survival cancer cells to radiation or other cancer therapies. There are three primary types based on different kinds of cancers: local, regional, and whole-body hyperthermia [9]. Several research results illustrate that applying hyperthermia as an adjuvant therapy can effectively reduce the size of tumors and improve the effect of other combined treatments [10-12]. One of the most popular thermal therapies is radio frequency (RF) hyperthermia, taking the advantage that RF waves can penetrate the human tissues to heat the malignant tumors. However, there comes a drawback that RF hyperthermia lacks of selectivity toward the cancer tissue. In this case, several focusing strategies for hyperthermia are introduced to enhance specific heating on the target while reducing the non-specific heating elsewhere.

Either RF or microwave thermal ablation are techniques in which EM energy is applied locally directly targeting cancer tissue. The ablation therapy is aiming at the eradication or substantial destruction of the tumor in a minimally invasive fashion without damaging adjacent vital structures [13]. The RF or microwave energy is guided through an electrically conducting probe inserted into the tumor, usually with a catheter. When the EM energy is deposited, the heating is only induced locally in a small area around the tip of the probe. The mechanism of heating with ablation is the resistive loss from the Joule's first law. However, the major disadvantages are that it is an invasive method, and it cannot be combined with drug delivery.

Currently the adaptive phased array [14] is the most well-developed approach to optimizing hyperthermia non-invasively using external sources. By adjusting the magnitude and phase of each element in the array, selective heating can be delivered after optimization. The method requires an adaptive optimization algorithm and takes several iterative runs to reach the final state that the heating is focused at the target location satisfying certain constraints. The parameters that used in the optimization criteria could be the specific absorption rate (SAR) [15-19], the temperature [20-24], or the energy [25].

Another approach is able to attain good focusing in hyperthermia is the Ultra-wideband (UWB) method. It is originated from a communication technology for the high-speed data transfer [26]. The focusing properties of the UWB method comes from the compensation of the propagation effects, including the delay in the time domain and the dispersion in the frequency domain. The system is implemented by passing the UWB pulse through designed finite-impulse response (FIR) filters [27, 28].

The time reversal (TR) technique, which was first proposed in late 1980s [29], achieved its focusing properties from the linear reciprocity, in time, of the wave equation. It takes advantage of the scrambled information of the complex media, which is included in the receiving signal, or the acoustic term “sona”, of each time reversal mirror (TRM) to achieve focusing at the target location. Compared to the traditional phased array or UWB method, TR requires neither calculation of the E-fields of each individual antenna of the array, nor a FIR filter design process.

In the past few decades, focusing with TR has been studied for acoustic and ultrasonic waves, e.g., in underwater communication [30] and lithotripsy [31]. More

recently, EM TR applications have been investigated in areas such as wireless communications [32, 33], imaging [34], and biomedical engineering [35, 36].

1.1 Research Objectives and Original Contribution

The main goal of this research project is to assess the focusing properties of electromagnetic TR methods in RF focused hyperthermia. It is analyzed from two perspectives: temporal and spatial focusing. The temporal focusing is about how well the original signal is reconstructed after the TR process, hence the similarity between the original and reconstructed signal is to be quantified. Moreover, the objective in the spatial focusing analysis is to calculate and improve the spatial resolution. To apply hyperthermia in cancer treatment, the heating effects of TR need to be investigated in both homogeneous and inhomogeneous media. Finally, a comparison between TR and existing focusing strategies are discussed. Original contributions in this dissertation are as follows.

- Based on the real clinical scenarios in the treatment of the head and neck tumor, an analytical model resembling the human neck tissue is proposed. The neck is modelled as an infinite length dielectric cylinder and the TR process is converted into a 2D line current source scattering problem. Both the time-forward and time-reverse Green's function could be solved analytically by applying basic electromagnetic theories.
- The spatial focusing limit is investigated from an asymptotic study featuring a closed time-reversal cavity (TRC). From the results of the asymptotic energy distribution, the focal spot size is defined and spatial resolution is hence calculated.

- The parametric study, such as carrier frequency, bandwidth and the shape of the TR source signal, is converted into an optimization problem with several energy constraints summarized from the clinical concerns. The carrier frequency is optimized by solving the constrained optimization problem. The effect of a broadband signal compared to a single frequency one is qualitatively discussed.
- From the energy distribution results contributed from a finite number of TRMs, the quality of the spatial focusing is analyzed. The position of the focal point is confirmed to be determined by the phase of each TRM, while the magnitude of that regulates the shape of the spot. Keeping the phase information the same to fix the target location, a magnitude correction of each TRM is introduced to optimize the hot spot under certain energy constraints.
- Full-wave simulations are carried out regarding the TR process in a two-channel reverberating and a multi-channel ballistic system using the time-domain solver in CST MICROWAVE STUDIO®. The temporal and spatial focusing is assessed from TR with an active source. The feasibility of focusing from TR with a passive nonlinear circuit is evaluated in combination with CST DESIGN STUDIO™.
- The experiments are designed and conducted to test the temperature change and the selectivity of the heating effects from EM TR. A gelled phantom, which has similar permittivity, conductivity and thermal conductivity properties to human tissues, is employed to build a temperature profile over the focusing area. The 1D and 2D temperature distribution are measured and analyzed in the gelled phantom.

1.2 Dissertation Overview

This dissertation is focused on the assessment of TR techniques for RF hyperthermia in cancer treatment. It is further extended into 7 chapters from theoretical, simulating and experimental points of view. Chapter 1 gives a general introduction to the RF hyperthermia as an adjuvant therapy in cancer treatment, followed by the state-of-the-art focusing strategies listed. Served as an innovative tool for focused hyperthermia, TR is thereafter presented.

Chapter 2 is a review of the EM theories related to the energy flow and thermal effects in biomatters. From the Maxwell's equation, EM waves behave differently depending on the material properties, leading to the difference in penetration depth and specific absorption rate (SAR). The fundamental model for the thermal effects is further explained in the bioheat equation. At the end of the chapter, the definition, development, methods and challenges of hyperthermia as a clinical application in cancer treatment are elaborated.

Chapter 3 provides an overview of the existing focusing strategies, including RF ablation, phased array, and Ultra-wideband (UWB), followed by an introduction to the TR techniques. It illustrates the TR technique in detail from its history, theory, methods and applications.

In Chapter 4, a simple analytical model is proposed to inspect the TR problem from the EM perspective. Simulating the clinical situation that a tumor is located in the neck region, the model quantifies the focusing properties of TR, provides the information about the spatial resolution, and further guides us for the choices of signal types, frequencies, bandwidths, and the number of antennas.

Chapter 5 discusses two methods to focus the EM energy non-invasively with TR. The first method is to utilize the full-wave simulation data over a personalized permittivity map to control the amplitude and phase of the practical antennas. The permittivity map could be created from the existing biological models incorporating the computed tomography (CT) and magnetic resonance imaging (MRI) data. The other approach is to spatially encoding the tumor site with a nonlinear beacon that emits new frequency components when an EM waveform is incident. The related simulations prove the feasibility of the two methods.

Chapter 6 describes the experiments in a wave-chaotic system to test the thermal effects of EM TR. It is designed to measure temperature not only at the source location, but also several other points near the target, so as to build a temperature distribution profile around the target area. Such profile is used to evaluate the selectivity of the heating effect from TR technique. The clinical prospects are also explored at the end of the chapter.

Chapter 7 concludes the assessment of TR from three perspectives. In theory, an analytical model is developed to guide the TR focusing procedure. Simulations show the feasibility of two non-invasive focusing methods. And experimentally the thermal effect and its selectiveness of TR are further proved. A brief discussion including the comparison between TR and phased array is illustrated afterwards, followed by the proposed future work of developing a clinical RF hyperthermia system featuring TR.

Chapter 2 EM Interaction with Human Tissues

2.1 Properties of Materials

The propagation of electromagnetic waves in human tissues is described by the time-harmonic steady state Maxwell's equations,

$$\begin{aligned} \nabla \times \mathbf{E} &= -\frac{\partial \mathbf{B}}{\partial t} \\ \nabla \times \mathbf{H} &= \mathbf{J} + \frac{\partial \mathbf{D}}{\partial t} \\ \nabla \cdot \mathbf{D} &= \rho \\ \nabla \cdot \mathbf{B} &= 0, \end{aligned} \tag{2.1}$$

with properties of materials in the constitutive relationships as follows:

$$\begin{aligned} \mathbf{B} &= \mu \mathbf{H} \\ \mathbf{D} &= \varepsilon \mathbf{E} \\ \mathbf{J} &= \sigma \mathbf{E}. \end{aligned} \tag{2.2}$$

So the permittivity, conductivity and permeability of human tissues play important roles in the interaction with EM waves. These properties of materials will be illustrated accordingly to help better understand the EM applications in cancer diagnostics and therapy.

2.1.1 Permittivity and Conductivity

The permittivity shows the resistance when developing an electric field. To be more exact, it indicates how much charge is needed to form one unit of electric flux in a particular medium. The relative permittivity ε_r, or dielectric constant, is defined as the ratio of the material's absolute permittivity to the permittivity of the free space ε_0

$$\varepsilon_r = \varepsilon / \varepsilon_0 , \tag{2.3}$$

where ε_0 is approximately 8.85×10^{-12} F/m.

The permittivity demonstrates the response of material to the electric field, which normally depends on the frequency of the externally applied field. There will be a loss introduced as polarization of material cannot pace up with the alternating field due to the frequency dependence. Hence the permittivity becomes complex

$$\varepsilon = \varepsilon' - j\varepsilon''. \tag{2.4}$$

The real part stands for the dielectric constant, which is proportional to the stored energy within the medium. The imaginary part comes from the polarization loss, which is related to the dissipation of energy. The loss tangent is the ratio between these two parts

$$\tan\delta = \frac{\varepsilon''}{\varepsilon'}. \tag{2.5}$$

The dielectric permittivity spectrum [37] from RF to UV is shown in Figure 2-1. The main source of polarization loss are from ionic and dipolar relaxation, atomic friction, and electronic resonances respectively as the frequency increases.

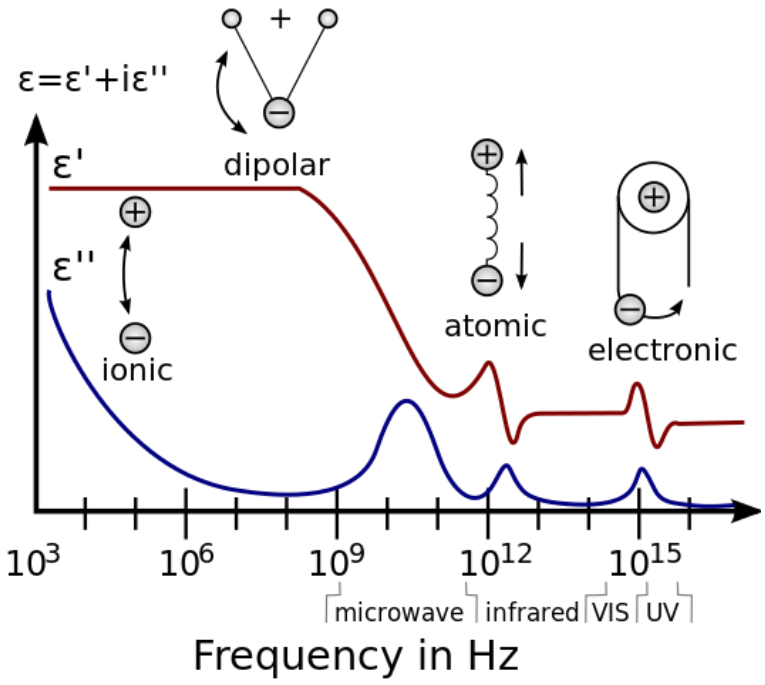

Figure 2-1 Frequency response of various dielectric mechanisms

The Debye model, introduced by Peter Debye in 1913, explains both the molecule and atom effects. So in RF and microwave region, it can be used to describe the complex permittivity, including dielectric constant and polarization loss, as a function of frequency

$$\varepsilon(\omega) = \varepsilon_{\infty} + \frac{\varepsilon_s - \varepsilon_{\infty}}{1 + j\omega\tau}, \tag{2.6}$$

where ε_{∞} is the permittivity at frequency infinity, ε_s is the static, low frequency permittivity, and τ is the delay constant. Here is an example modeling the complex relative permittivity of distilled water and human skin [38] using the Debye model as shown in Figure 2-2. Generally, for a dielectric material, the real part decreases and the imaginary part increases as the frequency goes up. Most of the human tissues have similar dielectric properties to water.

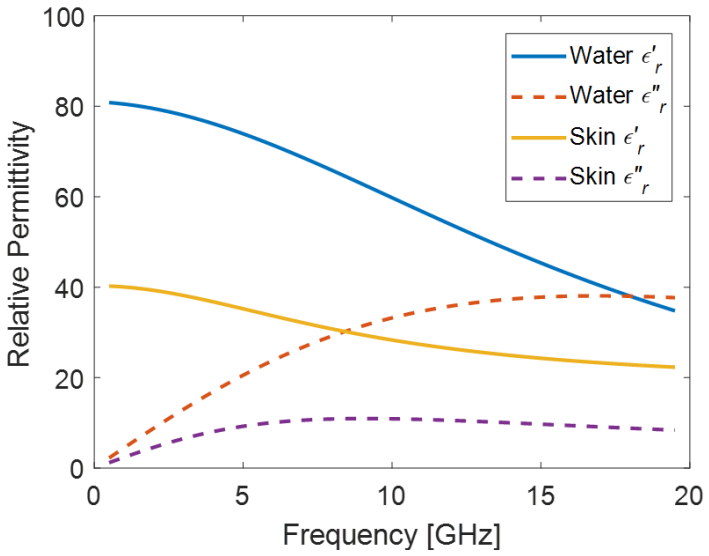

Figure 2-2 Modelling the real and imaginary part of the relative permittivity for distilled water and human skin using the Debye model

Cole-Cole model is a modification of the Debye model [39] and the complex permittivity is expressed now as

$$\varepsilon(\omega) = \varepsilon_{\infty} + \frac{\varepsilon_s - \varepsilon_{\infty}}{1 + (j\omega\tau)^{1-\alpha}}. \quad (2.7)$$

The correction parameter α, is taken from 0 to 1. When $\alpha = 0$, the Cole-Cole model reduces to the Debye model. This model has often been used to describe the permittivity in polymers, as well as biological tissues [40].

Conductivity shows the degree to which a specified material conducts an electric current. The materials can be classified into insulators, semiconductors, and conductors based on the conductivity. A list of dielectric constant and conductivity values of human hand and head tissues at 930 MHz [41] are shown in Table 2-1. Most of the conductivity values are within the range between 10^{-2} to 10^{0} S/m, except for blood, which is above 1 S/m.

Table 2-1 Dielectric constant ε_r' and conductivity σ of human tissues at 930 MHz

Tissue Type	Dielectric Constant ε_r'	Conductivity σ [S/m]
Skin	48.0980	0.6657
Bone	13.2700	0.0869
Muscle	57.5960	0.7834
Fat	5.6000	0.0403
Blood	64.8200	1.3320
Cartilage	46.0430	0.5690
Cerebrospinal Fluid (CSF)	36.0650	0.4329
White Matter	42.8100	0.4290
Grey Matter	58.5500	0.7150

If we take a look back at the Maxwell's equations, both permittivity and conductivity appears in the Ampere's Law,

$$\nabla \times \mathbf{H} = \sigma \mathbf{E} + j\omega\varepsilon \mathbf{E} . \tag{2.8}$$

Consider it in a homogeneous source-free region in the frequency domain, the effective permittivity can be defined as

$$\varepsilon_c = \varepsilon - j\frac{\sigma}{\omega} . \tag{2.9}$$

The real part of ε_c represents the dielectric constant and the imaginary part of effective permittivity now includes both polarization and conductive losses. This allows us to solve a problem involving a lossy material using the exact same approach as the corresponding free-space problem, by simply substituting the material properties.

2.1.2 Permeability

In electromagnetism, permeability is the property of a material, which shows the ability of it to be permeated by magnetic flux. Specifically, permeability is the level of magnetization of a particular material in a magnetic field. The relative permeability μ_r, is the ratio of the permeability of a specific medium to the permeability of free space μ_0

$$\mu_r = \mu / \mu_0 , \tag{2.10}$$

where μ_0 has the exact value $4\pi \times 10^{-7}$ H/m.

Depending on the permeability, materials are divided into four categories. Their B-H curves, which shows the relationship between magnetic flux density (B) and magnetic field strength (H), are shown in Figure 2-3. Nonmagnetic materials has $\mu = \mu_0$, such as air and most of the biological tissues [42]. The permeability of diamagnetic materials is less μ_0, while that of paramagnetic materials is larger than μ_0, as one is opposing to the externally applied magnetic field, the other is strengthening, relatively. Different from these three types that has linear B-H relation, ferromagnetic materials are strongly

nonlinear. For smaller H-field, the above relation is almost linear with the permeability far greater than μ_0.

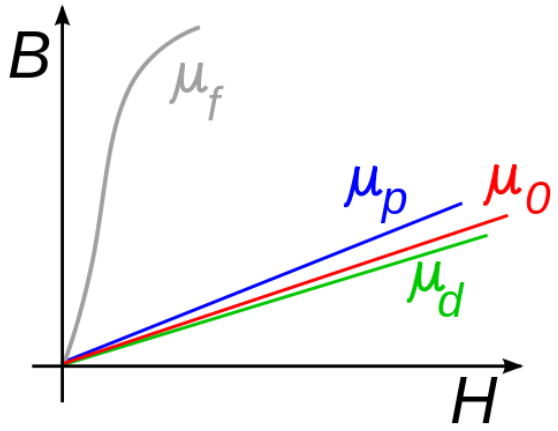

Figure 2-3 Schematic B-H curves of the following materials: ferromagnetic (μ_f), paramagnetic (μ_p), free space (μ_0) and diamagnetic (μ_d)

2.2 Propagation and Energy Flow

2.2.1 EM Wave Propagation

For guided waves in transmission line structures, the propagation constant γ is defined by the ratio of the field A_0 at the source of the wave to the field A_z after wave propagating to some distance. For example, the E-field of a plane wave propagating along the *z*-axis can be found as

$$E(z) = E_0 e^{-\gamma z}. \tag{2.11}$$

It is commonly expressed as

$$\gamma = \alpha + j\beta = j\omega\sqrt{\mu\varepsilon_c} = j\omega\sqrt{\mu(\varepsilon - j\frac{\sigma}{\omega})}, \tag{2.12}$$

where α is the attenuation constant in nepers/m, β is the phase constant in radians/m, which describes the magnitude and phase changes respectively as the wave propagates over the space.

Taking the square on both sides of (2.12) and equating the real and imaginary part, we expand the α and β as follows [43]:

$$\begin{aligned}\alpha &= \omega\sqrt{\frac{\mu\varepsilon}{2}\left(\sqrt{1+(\frac{\sigma}{\omega\varepsilon})^2}-1\right)} \\ \beta &= \omega\sqrt{\frac{\mu\varepsilon}{2}\left(\sqrt{1+(\frac{\sigma}{\omega\varepsilon})^2}+1\right)}.\end{aligned} \tag{2.13}$$

The wavelength λ in the lossy media should be always real, calculated from the phase constant, the imaginary part of the propagation constant

$$\lambda = \frac{2\pi}{\beta}. \tag{2.14}$$

In a travelling plane wave, the vector Helmholtz equation in a source-free homogeneous region for electric and magnetic fields is derived from the Faraday's Law and Ampere's Law in (2.1) as

$$\begin{aligned}\nabla^2\mathbf{E} + k^2\mathbf{E} &= 0 \\ \nabla^2\mathbf{H} + k^2\mathbf{H} &= 0,\end{aligned} \tag{2.15}$$

where k is the wavenumber given by

$$k = k' - jk'' = \omega\sqrt{\mu\varepsilon_c} = \omega\sqrt{\mu(\varepsilon - j\frac{\sigma}{\omega})}. \tag{2.16}$$

It is the spatial frequency of a wave, showing the number of waves in radians per unit length. The real part denotes the wave propagation and the imaginary part accounts for the loss.

The wavenumber k is often confused with the propagation phase constant β. They are equivalent to each other for TEM wave (transverse EM wave) which travels in

transmission lines such as coaxial cable or twin leads. However, it is not valid for non-TEM wave or in a lossy media.

2.2.2 Penetration Depth

Penetration depth is the depth below the surface of the material, where the intensity of radiation reduces to 1/e (about 0.37) of the value at the surface, which is given by the reciprocal value of the attenuation constant in (2.13)

$$\delta = \frac{1}{\alpha} = \left(\frac{1}{\omega}\sqrt{\frac{2}{\mu\varepsilon}}\right)\left(\sqrt{1+(\frac{\sigma}{\omega\varepsilon})^2}-1\right)^{-\frac{1}{2}}. \tag{2.17}$$

It is related to the energy of EM radiation that can reach the deep seated tumor in cancer therapy. The penetration depth of some typical human tissues, such as skin, fat and blood are shown in Figure 2-4. The dielectric constant ε_r' and conductivity σ data is from Table 2-1 and considered constant over the frequency range.

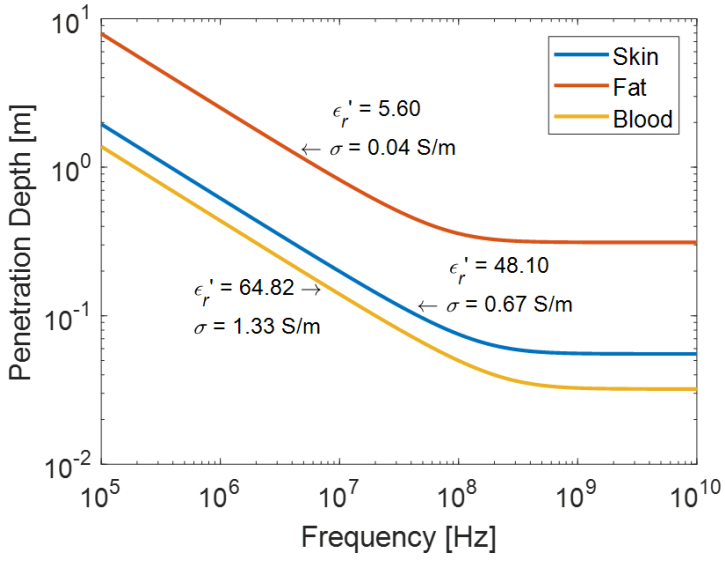

Figure 2-4 Penetration depth in typical human tissues

First the penetration depth decreases linearly as the frequency increases. After a certain point, it becomes a constant in the higher frequency ranges. So it is a good choice

to apply hyperthermia in RF because the EM waves in this frequency range can penetrate through the human tissues. The slope of these curves are identical, roughly -1/2 as it occurs in the power term of (2.17). However, the offsets of these curves depend on the conductivity and dielectric constant. Since the human tissues are generally non-conductive, the conductivity σ will determine the low frequency penetration depth, while the dielectric constant ε_r' will have more influence on the high frequency behavior [44].

When the conductivity of the material is high enough, the dielectric part is negligible compare to the conductive part. The penetration depth will become the so-called skin depth, because the electric current flows mainly at the "skin" of the conductor. The skin depth is inversely proportional to the square root of the frequency shown as

$$\delta = \sqrt{\frac{2}{\omega\mu\sigma}} \tag{2.18}$$

2.2.3 Specific Absorption Rate

In a source-free homogeneous region, the conservation of energy for EM waves is described in the integral form of Poynting's theorem

$$\oint_S \overrightarrow{\mathscr{S}} \cdot \mathbf{n}\, dS = -\int_V \sigma \overrightarrow{\mathscr{E}}^2\, dV - \frac{\partial}{\partial t}\int_V \left(\frac{1}{2}\varepsilon \overrightarrow{\mathscr{E}}^2 + \frac{1}{2}\mu \overrightarrow{\mathscr{H}}^2 \right) dV\,, \tag{2.19}$$

where the instantaneous Poynting vector in the time domain is defined as

$$\overrightarrow{\mathscr{S}} = \overrightarrow{\mathscr{E}} \times \overrightarrow{\mathscr{H}}\,, \tag{2.20}$$

and it indicates the power flow density in W/m^2 at a single temporal and spatial point on the surface *S*. Hence in (2.19), the left hand side denotes the total instantaneous power flowing out of surface *S*. The first integration term on the right-hand side shows the instantaneous energy dissipated from ohmic loss within the volume *V* enclosed by surface

S. The integral in the second term represents the stored electric and magnetic energy in volume *V*.

In the biomedical applications, we are concerned about the thermal and heating effects of EM waves, which is seen under the RF exposure after a period of time. Therefore it is important to check the time-averaging power delivered to and dissipated in the tissues. The complex Poynting's theorem is given by

$$\oint_S \mathbf{S}\cdot\mathbf{n}\, dS = -\int_V \left(\frac{1}{2}\sigma|\mathbf{E}|^2\right) dV - 2j\omega\int_V \left(\frac{1}{4}\mu|\mathbf{H}|^2 - \frac{1}{4}\varepsilon|\mathbf{E}|^2\right) dV\,. \tag{2.21}$$

The left hand side shows the total complex power, which is equivalent to the time-averaging power flowing out of *S*. On the right-hand side, the first term is the time-average power dissipated in watts due to conductive losses, in addition to the second term that determines the reactive power consumed in VARs related the stored energy in volume *V*.

The specific absorption rate (SAR) [45] is hereby defined as the dissipated power per unit mass (W/kg) as follow

$$\text{SAR} = \frac{\sigma}{2\rho}|\mathbf{E}|^2\,, \tag{2.22}$$

where σ is the conductivity in S/m, and ρ is the density of the medium in kg/m^3. As SAR is used to measure the energy absorption rate by the human body with exposure to an EM field. Depending on the region where power absorption takes place, SAR concept can be applied to whole-body and to small localized volumes, defined as average and peak SAR, respectively. The whole-body SAR is related to the elevations of the body temperature, overall heating, and possible tissue damage, while the local peak SAR represents the power absorbed in a confined body region. The local SAR is averaged over a specific tissue mass, typically 1g or 10g, in a small sample volume cube. In United States, FCC regulates that

the local SAR averaged over 1g is below 1.6 W/kg averaged. And in Europe, Australia, Japan, and other parts of the world, the SAR averaged over 10 g is limited to 2 W/kg developed by the IEC [46]. In order to successfully heat the tumors, the local SAR must be controlled within the range of about 50 to 350 W/kg [47].

SAR is the key feature to analyze when validating potential health hazards, such as the use of mobile phone [41, 48-51], the EM field exposure [52, 53] and the induced heating in MRI [54]. It is also commonly applied to optimize the innovative therapeutic approaches [16, 19, 55] and regulate safety standards [46, 56], etc.

2.3 Bioheat Equation

In order to localize heating in biomedical procedures, the accurate knowledge of heat distribution is highly demanded. However, such knowledge can be acquired by measuring the temperatures *in vivo* during the heating process, which is risky and inaccurate because it is an invasive method on limited number of discrete locations. Therefore, the modelling of bioheat transfer, which enables the simulation of human tissues' interaction with the EM waves without extensive human test, is essential to study the thermal therapy in cancer treatment.

A famous study in the modelling of heat transportation is done by Pennes [57] for the perfused tissue. The bioheat equation that takes into account heat production in biological tissue due to metabolic processes and heat flow due to perfusion of blood is expressed in the following form

$$\rho c \frac{\partial T}{\partial t} = \nabla \left(k \cdot \nabla T \right) + \omega_b c_b (T - T_b) + Q_m + \sigma \left| \mathbf{E} \right|^2 , \tag{2.23}$$

where T is the temperature of the tissue (°C), ρ the density of the tissue (kg/m^3), c the specific heat of the tissue (J/kg/°C), k the thermal conductivity of the tissue (W/m°C), ω_b

the blood volumetric perfusion rate (kg/m^3/s), c_b the specific heat of blood (J/kg/°C), and T_b the average temperature of blood (°C). Q_m is the mechanism for basal metabolic heat generation (W/m^3), σ the conductivity of the tissue (S/m) and E the vector electric field (V/m) acting as the heating source.

Generally, the total heating on the left hand side of the equation consists of the heat loss from thermal conduction, the heat loss from blood flow, the metabolic heating, and the Joule's heating due to the EM source representing each term on the right-hand side, respectively. So the rate of temperature change is related to the SAR as

$$\frac{\Delta T}{\Delta t} = \frac{(\mathrm{SAR} + P_m - P_c - P_b)}{c}, \tag{2.24}$$

where $\Delta T/\Delta t$ denotes the temperature change over time, P_m the metabolic heating rate, P_c the rate of heat loss due to thermal conduction, P_b the rate of heat loss due to blood flow, and c the specific heat. At the initial state of the EM exposure, the steady-state condition satisfies that

$$P_m = P_c + P_b. \tag{2.25}$$

Hence SAR can be related to slope of temperature *versus* time curve as

$$\mathrm{SAR} = c\frac{\Delta T}{\Delta t}. \tag{2.26}$$

Accordingly SAR can be determined from the ratio of the initial increase in the tissue temperature to a short period of time right after the EM source is applied.

2.4 Hyperthermia in Cancer Treatment

2.4.1 Introduction

Generally, hyperthermia is a symptom when human body generates or absorbs much more heat than dissipates, body's thermoregulation system fails to handle the extra

heat, which leads to an elevation of body temperature. However, hyperthermia can be used to treat cancer as well. With cautiously controlled part of or whole body temperature, the aim to damage or kill the stem cancer cells can be achieved. Hyperthermia was studied to be applied as therapy from 1970s. Over decades of studies on cell cultures *in vitro* and clinical trials on tumors *in vivo*, the results show a significant improvement of response, which convinces the clinical application of hyperthermia [8].

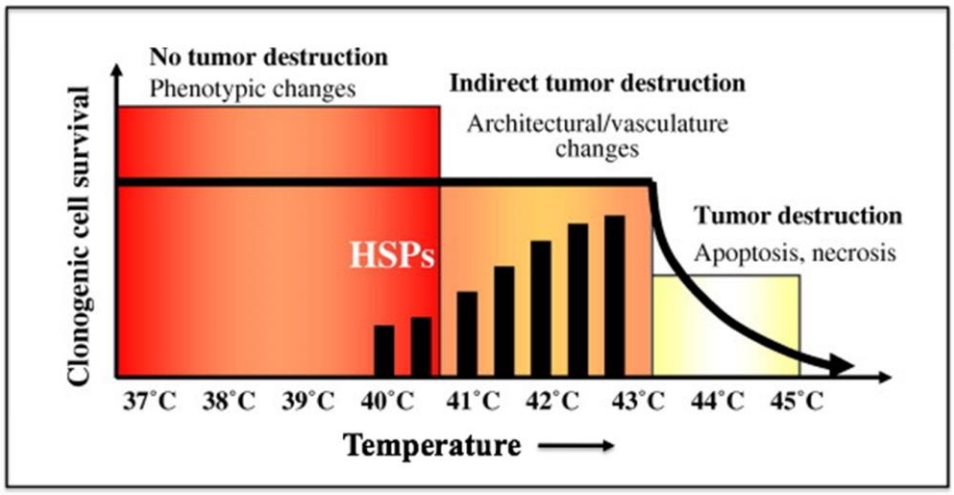

Figure 2-5 Tumor destruction temperature range

Normally, during hyperthermia treatment, the tumor area is exposed to the temperature between 41°C to 45°C for a period of time [58]. Figure 2-5 shows the temperature range of the tumor destruction [59]. Protein in cells is aggregated and unfolded under this high temperature environment. Because great amount of DNA is packed within protein and there is plenty of different functional protein in stem cancer cells, abnormal aggregation and unfolding of protein leads to cell damage or even necrosis [60]. Temperature, dose of heat treatment and the characteristics of cancer tissue have great influence on the effectiveness of hyperthermia treatment [61]. During the treatment, the temperature of the cancer and surrounding tissues needs to be monitored and confirmed

among the desired range [8]. The heat of hyperthermia therapy is transferred from external devices with different techniques, such as ultrasound, radiofrequency or microwaves [62].

In today's cancer treatment, hyperthermia is always applied with other cancer therapies, such as radiotherapy, chemotherapy, surgery, immunotherapy, and so on. There are several biological rationales explaining why combining hyperthermia with other therapies is able to give better performance than using hyperthermia alone. The survival rate of cells is dependent on the environment temperature and the exposed period to the high temperature, which means with higher temperature and longer hyperthermia period, the survival rate becomes lower. With hyperthermia therapy, the microenvironmental factors of cancer cells, such as oxygen content, pH level and nutrition, are changed to be detrimental [58]. Moreover, the aggregation and unfolding of protein in nucleus because of high fever significantly reduces the drug resistance of cancer cells and increase the sensitivity to radiation. In this case, hyperthermia therapy is able to sensitize tumor cells to response to other treatments like radiotherapy and chemotherapy.

2.4.2 Types

Depending on the size, location and depth of the tumor, hyperthermia therapy can be divided into three types, local, regional and whole-body hyperthermia (WBH). The heat of the three hyperthermia types can come from systems with different external sources, such as microwaves, radiofrequency, ultrasound, hot water perfusion and so on [9].

In local hyperthermia, heat is specifically delivered to the tumor area with various techniques. This kind of hyperthermia treatment is well studied due to an uncomplicated principle that when the temperature of the tumor area is elevated to 42°C for one hour and there are reports that the cancer cells are directly killed [58]. In addition, cancer cells are

more sensitive to temperature change than normal cells because of poor blood circulation. There are three parts in a system for local hyperthermia system, such as a generator, a superficial and interstitial applicator, and a miniature temperature sensor in the tumor. In general, microwaves, radio waves or ultrasound are utilized in this system to generate heat. Through the local hyperthermia procedure, it is indispensable to build cooling systems in order to prevent skin and healthy tissues nearby from burning or blistering. Water bolus is frequently used in local hyperthermia, because it is able to keep the temperature of skin at normal body temperature without blocking EM waves applied on targeted tumor area [61].

Regional hyperthermia is far more complicated compared with local hyperthermia. It is used to deal with deep-seated tumor in abdominal cavity or pelvis. As the heat is delivered to a larger part of body, applying regional hyperemia is supposed to conduct preliminary investigation, propose detailed plan and carefully monitor temperature change. There exist three major methods of regional hyperthermia, deep regional hyperthermia, thermal perfusion and continuous hyperthermic peritoneal perfusion (CHPP) [9]. The energy of EM waves can be absorbed by other tissues when the tumor is deep-seated, hence external applicators such as radiofrequency capacitive heating apparatus are required in deep regional hyperthermia. Thermal perfusion therapy is always used in cancer of arms and limbs (e.g. melanoma) or liver and lung. In this treatment, blood from tumor area is drained, heated in an extracorporeal way and commonly perfused back with anticancer drugs. CHPP is frequently used with surgery to treat peritoneal carcinomatosis, colorectal metastases or stomach cancer. Through CHPP procedures, the anticancer drug fluid from a heated device is delivered to flow through the cancer area [63].

WBH is mostly applicable in metastatic cancer with conventional chemotherapy or radiotherapy. There lists three primary methods of WBH, which are surface heating, extracorporeal induction and radiant or electromagnetic induction [64]. In the process of WBH, patient's body temperature is heated up to 42°C by thermal chambers, heated blankets or infrared radiators. Before applying WBH, it is essential to assure that the patient is in good condition, because of serious side effects such as influences on tissue metabolism and blood pressure.

2.4.3 Challenges

As an adjuvant therapy, hyperthermia gives outstanding performance in cancer treatment. However, there exist a large quantity of challenges which need to be overcome by more clinical trials and experimental research. In the existing literature, although some methods of local hyperthermia can reach deep-seated tumor, the results do not meet the expectation. It is still necessary to look for technology of depth-heating to deep-seated tumor. Moreover, the existing methods suffer from a lack of focusing and selectivity of energy as well. In order to control heated system parameters, there needs plenty of experiments and calculations. In addition, the heating process of hyperthermia is not capable of repeating. Owing to different patients and cancer types, hyperthermia therapies show high level of personalization. Furthermore, because of interdependency between technology, physiology, and biology, it is complicated when processing the treatment.

Chapter 3 Focusing Strategies in Hyperthermia

3.1 Thermal Ablation

As a cancer treatment, ablation therapy is the removal or destruction of tumor tissue by applying chemical or thermal methods. In thermal ablation, tumor is exposed to extreme temperatures in order to irreversibly damage the cancer cells. Compared with surgery, thermal ablation is less invasive and has less influences on the surrounding tissues. In addition, for patients that are risky to conduct surgery or other conventional therapies, thermal ablation is used alternatively and even can increase the possibility to carry out these conventional therapies.

Thermal ablation is a minimally invasive tumor therapy, because of the advanced imaging technologies and accurately focusing heat on the targeted tumor tissue. Multiple energy sources are used to heat tumor to more than 50°C, which leads to irreversible injuries [65]. There are several thermal technologies frequently used, lasers, RF, microwave and high-intensity focused ultrasound (HIFU). Different from hyperthermia therapies, each ablation technique has an "applicator", which is inserted into the tumor tissue in a minimally invasive way and monitored by imaging devices. The heat is transferred by thermal conduction from the surrounding region of the applicator to the overall tumor [66], which means the heating from the ablation techniques are localized. Typically, thermal ablation is used to treat inoperable cancer, such as liver, prostate or uterus, because it has capability of preserving the nearby organ function. However, it is barely used for a tumor with large volume. Nowadays, RF and microwave ablation are gaining increasingly research and clinical interests as they have been proved as reliable treatment modalities that enables tissue heating and coagulation necrosis [67, 68].

3.1.1 RF Ablation

Most RF devices used in RF ablation are operated in the range of 460-480 kHz [69] with output energy around 200W. The applicator of RF ablation is small probe shown in Figure 3-1, which can deposit RF energy and heat the tumor area to a high temperature, usually more than 60°C, during a short period of time in order to kill and destruct the stem cancer cells. There are various types of probes are designed, such as multi-prong electrodes, expandable electrode, bipolar electrode and *etc*. [58]

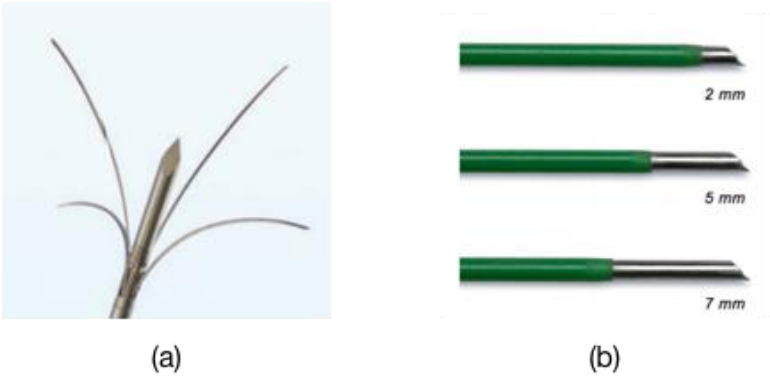

Figure 3-1 RF ablation probes (a) multi-prong electrodes from RITA medical systems (b) straight trigeminal RF electrode from COSMAN

During RF ablation, the healthy tissues around tumor are probably damaged by RF energy. The procedures of RF ablation are shown in Figure 3-2 [70]. The first step is to place the RF probe into the tumor tissue. The prongs are extended and the RF energy is exposed. Then, the stem cancer cells are heated and got damaged. Through the procedures, it is obvious that surrounding tissues are heated by the probe as well. Therefore, imaging devices such as ultrasound and CT scanner are supposed to be used to monitor the probes injected into the tumor so as to make sure that the size of surrounding healthy tissue damaged by RF ablation is adequate.

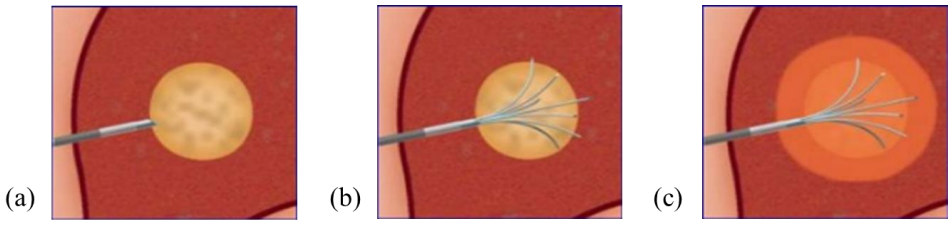

Figure 3-2 Procedures of RF ablation: (a) probe insertion; (b) extension of prongs; (c) RF current applied

3.1.2 Microwave Ablation

Compared to RF ablation, microwave ablation (MWA) has the advantage of applying on larger and deeper tumor during a much shorter period of time. Therefore, it has witnessed a rapid development of MWA on percutaneous, laparoscopic, and open surgical access [71]. In MWA, antennas are used as applicator, which is connected with a coax cable, to emit microwaves with frequency of 915 MHz or 2.45 GHz. Because of the shorter wavelength, it only needs a small antenna to transmit and directly focus the energy to the tumor tissues. The microwave antenna is places by the guidance of CT scanner or ultrasound as well. As shown in Figure 3-3, the antenna is connected to the microwave generator by a coaxial cable and placed in the tumor deep-seated in the liver [72].

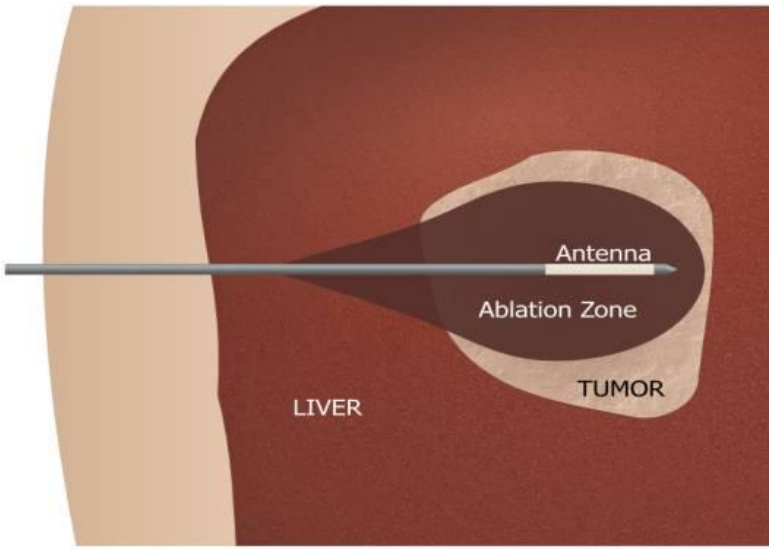

Figure 3-3 MWA application of liver cancer

3.1.3 Limitations

As illustrated before, in RF ablation, healthy tissues close to the tumor issue may got damaged or killed as well. With inappropriate use of RF ablation, it has a high probability to cause induced necrosis. Therefore, when applying the RF method, it needs assist from physicist with knowledge of RF principles in clinical trials to ensure the safety of the treatment while achieving the best performance. In addition, the RF ablation is not able to treat tumors with larger size or deep-seated because heat is only conducted to a limited size of area. Consequently, it may easily lead to the high recurrence rate of cancer cells. Another limitation of RF ablation comes from the electrical current path. Since the current omnidirectionally flow from the probe to the grounding pad, it may generate heterogeneous energy and cause collateral damage. Moreover, because of the current flow, skin near the grounding pad may get burns, bubbling or charring.

Although MWA has more benefits than RF ablation, there still exist several limitations. One of the major limitations is the energy lost. Due to the dielectric and impedance mismatching, thermal energy may dissipate and reflect during the transfer [73]. As the antenna is attached to a coax cable, when delivering energy, the cable gets heated as well. Hence, this energy lost results in melt of the inner dielectric insulator and the outer plastic sheath. Furthermore, there is a lack of unidirectional antenna which is able to focus the thermal energy directly to the tumor tissue instead of blood pool surrounding. For example, if the tumor is close to large vessels, most of the thermal energy may transfer to the circulating blood pool. Therefore, it is difficult to eradicate that tumor. Under these circumstances, MWA is not suitable for tumor near vessels or heart tissue. Additionally, it

is complex to design specific antennas for different kinds of tumors. Until now, more researches and experiments need to be done to make thermal conduction more efficient.

In conclusion, there are several major limitations of thermal ablation. As illustrated before, all kinds of thermal ablation consist of applicators, which means thermal ablation is an invasive treatment. Also, with thermal ablation, there occurs heterogeneous heating which may cause tissue bubbling or charring, even other collateral damage. Plus the performance is poor near the blood vessels due to the heat loss from the perfusion. Additionally, there is a significant energy lost because of the impedance mismatch, which reduces the efficiency of thermal ablation.

3.2 Phased Array

The adaptive phased array approach was introduced to apply hyperthermia non-invasively by Fenn in 1991 [74]. A phased array consists of multiple antenna elements that typically transmit or receive signals in a certain phased delay between the elements. Theoretically, the desired field distribution in the human tissue could be generated by adjusting the magnitude and phase of each element in an adaptive phased array. In order to deliver as much power as possible into the tumor site, the receiving sensors are positioned as close as possible to the human body. At the same time fillers are placed between the antennas and the skin of the body is to lower the heating effect from the antenna contact. Figure 3-4 shows a clinical RF hyperthermia system, BSD-2000 annular phased array, developed by Pyrexar® Medical Inc. [70] It uses an annular phased array configuration of up to 8 dipole antennas operating at 75 – 140 MHz to shape and focus thermal energy on targeted treatment area deep inside the pelvis, abdomen, limbs or chest.

Figure 3-4 Pyrexar® BSD-2000 annular phased array for RF hyperthermia

To avoid undesired hot spots, it is necessary to optimize the field distribution to thermally heat a deep-seated tumor with a focused EM field while nullifying the EM field on the surface of the body under specific energy constraints. The flow chart of the optimization process is shown in Figure 3-5.

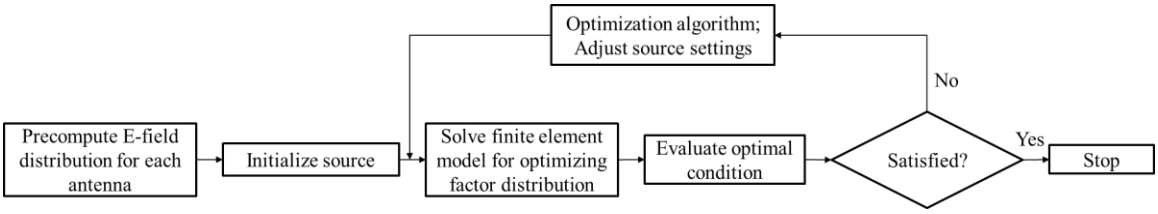

Figure 3-5 The optimization process of an adaptive phased array

First the field distribution in the interested region from each antenna is precomputed so as to come up with an initial source configuration. With the initial guess, the total field is solved from the finite element model to get the optimizing factor distribution, followed by an optimal condition check. If the condition is satisfied, the optimization process is finished. If not, the source settings are adjusted by performing optimization algorithms. Most optimization algorithms are aiming at maximizing the ratio of SAR in the tumor to the SAR in normal tissues [15-19]. More intuitively, temperature-based optimization is

directly evaluated from the bioheat equation [57] that takes into account the heat loss during the exposure, e.g. from thermal conduction and blood perfusion. It is required that the temperature in the tumor should be set to the hyperthermia level while the healthy tissue temperature should stay below 42 °C [20-24].

3.3 Ultra-wideband (UWB)

Ultra-wideband (UWB) is a communication technology for the short-range high-data application [26]. It utilizes low power ultra-narrow pulses in the time domain which results in an ultra-wide bandwidth in the frequency domain. UWB has been employed in the human body imaging of particular organs, such heart, lung, breast, and organs involved in the speech and the respiratory system [75]. Compared to the other narrowband systems, UWB systems have the advantages of reduced fading, low power and small interference.

UWB systems use an antenna array to focus the energy. The magnitude and phase is determined by compensating the propagation effects, including the delay in the time domain and the dispersion in the frequency domain, from each antenna to the target location. The system is implemented by passing the UWB pulse through designed finite-impulse response (FIR) filters [27, 28] as shown in Figure 3-6.

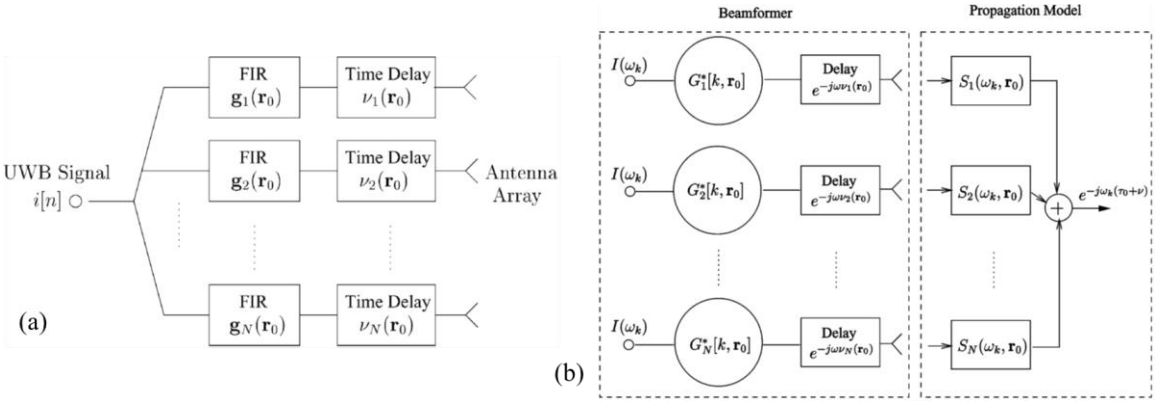

Figure 3-6 FIR design of a UWB system: (a) time domain; (b) frequency domain

3.4 Time Reversal (TR)

3.4.1 History

In 1989, the first work regarding the time reversal (TR) technique was found in acoustics by Fink *et al*. [29] Time-reversal mirrors (TRM) are utilized to obtain self-focusing for an acoustic source in an inhomogeneous media. In 1992, TR is introduced as a new focusing technique for hyperthermia by Fink *et al.* [76], Wu *et al.* [77], and Cassereau *et al.* [78] after the research and experiments in ultrasonics. These three papers are often referred as the fundamentals of TR concepts. The biomedical application of ultrasonic TR is further illustrated in lithotripsy [31] and transskull therapy [79] by Thomas *et al.* at the year of 1996. Since then, methods based on time-reversal have attracted a considerable attention in acoustics and ultrasonics. Until very recently, the first TR experiment in EM was conducted by Lerosey *et al.* [80] in 2004. It shows the temporal and spatial focusing of EM waves in a reverberating cavity. It opens up a wider application area for TR in RF and microwave frequency. The systematic theory of time-reversal cavity (TRC) in EM was proposed by Carminati *et al.* [81] in 2007. Up to today, TR is a promising technique that has not been fully developed yet and there is much room for further research.

3.4.2 Methods

The procedure of TR is shown in Figure 3-7. First, an original pulse is transmitted from Port 1. Next, after it goes through multiple paths of reflection and scattering in the complex media, the receiving signal, noted as “sona” from the first TR study in acoustics, is recorded at Port 2. The “sona” contains all the information of the complex media regardless of the loss. The “sona” signal is then time-reversed and transmitted from Port 2. Finally, back at Port 1, there should be a time-reversed version of the original signal fully

reconstructed. Also most of the transmitted power will concentrate in exactly the same location at where the original source was launched.

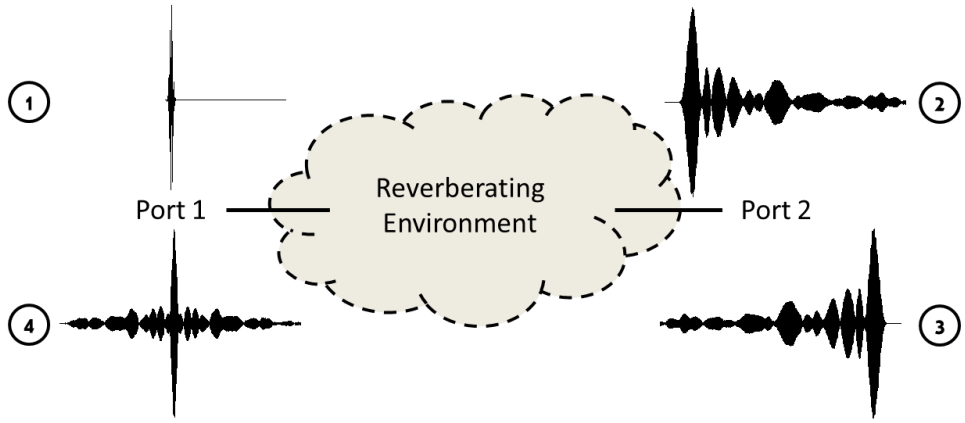

Figure 3-7 The procedure of TR

3.4.3 Theory

As for the focusing in the complex media, any kind of wave sent to the target is reflected and scattered during the propagation. The waves is dissipated in the lossy media and even if there is no loss it gets dispersed, which is generally considered as the loss of the information. However, the information is not irretrievably lost, instead it is scrambled into the disordered interference patterns [82]. TR offers a way to make the use of these scrambled information and is further illustrated in detail as the following. Starting from the wave equation, the time-forward step in the TR process in a TRC that encloses a homogeneous medium is described as

$$(\nabla^2 - \frac{1}{c^2}\varepsilon_r \frac{\partial^2}{\partial t^2})\mathbf{E}(\mathbf{r},t) = \Phi(t)\delta(\mathbf{r}-\mathbf{r}'), \tag{3.1}$$

where **r'** is the source position located in the volume *V* surrounded by cavity surface *S*, **r** the observation point, *c* the speed of light in the vacuum, ε_r the relative permittivity. The

right-hand side represents the Dirac distribution at the source point and $\Phi(t)$ is the source function.

Assuming the observation point $\mathbf{r}$ is on the surface of the TRC in the far-field region, the field from the source propagation in the time domain, namely the "sona" signal, is deduced from the Green's function

$$\mathbf{E}(\mathbf{r},t)=\frac{1}{4\pi|\mathbf{r}-\mathbf{r}'|}\Phi(t-\frac{|\mathbf{r}-\mathbf{r}'|}{c}). \tag{3.2}$$

The time-reverse step of the TR process is to transmit the fields measured during the time-forward step on the surface of the cavity in a time-reversed order. The TR operation is performed by the transform t to $T-t$, where T represents the total measured time after which the "sona" field vanishes. Since $\mathbf{E}(\mathbf{r}, t)$ is a real function, $\mathbf{E}(\mathbf{r}, -t)$ is equivalent to complex conjugation of $E^*(\mathbf{r}, \omega)$ in the frequency domain. Following the proposals of the existing TR theory [78, 81], the solution of the time-reversed electric field $\mathbf{E}_{\mathbf{tr}}(\mathbf{r}, t)$ is calculated from the temporal convolution between the transformed excitation waveform $\Phi(T-t)$ and the difference between reverse Green's function $G(\mathbf{r}, \mathbf{r}', -t)$ and the forward Green function $G(\mathbf{r}, \mathbf{r}', t)$

$$\mathbf{E}_{\mathbf{tr}}(\mathbf{r},t)=\Phi(T-t)\otimes[G(\mathbf{r},\mathbf{r}',-t)-G(\mathbf{r},\mathbf{r}',t)]. \tag{3.3}$$

The kernel distribution $K(\mathbf{r}-\mathbf{r}', -t)$, regardless of the source function, is defined as

$$K(\mathbf{r}-\mathbf{r}',-t)=G(\mathbf{r},\mathbf{r}',-t)-G(\mathbf{r},\mathbf{r}',t), \tag{3.4}$$

which has a simple form in the homogeneous medium

$$K(\mathbf{r}-\mathbf{r}',t)=\frac{1}{4\pi|\mathbf{r}-\mathbf{r}'|}\left[\delta(t+\frac{|\mathbf{r}-\mathbf{r}'|}{c})-\delta(t-\frac{|\mathbf{r}-\mathbf{r}'|}{c})\right]. \tag{3.5}$$

This equation implies that the focusing of TR comes from two impulse spherical waves that converge to and diverge from the source location respectively, with an arrival time

difference of $\frac{2|\mathbf{r}-\mathbf{r}'|}{c}$. This is directly related to the theoretical limitations of the TR process. Taking the Fourier transform of kernel distribution over time, we obtain

$$K(\mathbf{r}-\mathbf{r}',\omega)=\frac{1}{j\lambda}\frac{\sin(\frac{2\pi|\mathbf{r}-\mathbf{r}'|}{\lambda})}{\frac{2\pi|\mathbf{r}-\mathbf{r}'|}{\lambda}}, \tag{3.6}$$

where λ is the wavelength. The spatial focusing resolution from a self-focusing process in a homogeneous medium is $\lambda/2$, which is consistent with the classical diffraction limit in optics. However, the results are derived based on the far-field assumption. A remarkable $\lambda/30$ spatial resolution has been demonstrated by Lerosey *et al.* [83] in the near-field.

3.4.4 Applications

Owing to its intrinsic spatio-temporal focusing property, TR has been applied in a variety of areas. In the early-stage study in acoustics and ultrasonics, TR is involved in sonar for underwater communication [30]. It also gains acceptance in the non-destructive evaluation (NDE) [84], such as flaw detection [85], nonlinear damage detection[86], and structural health monitoring [87]. As the research of TR acoustics develops, it has attracted a considerable attention in biomedical engineering [88], including lithotripsy [31] and high-intensity focused ultrasound (HIFU) [89]. More recently, TR finds its place in high frequency ranges such as wireless communications [32, 33, 90], geophysics [91, 92], and imaging [34]. Furthermore, simulation results have shown that TR is a promising method in cancer detection [93] and hyperthermia [35, 36, 94].

Chapter 4 TR Analytical Model

4.1 Existing Analytical Methods

The acoustic theory of TR was first proposed by Cassereau and Fink [78] following their ultrasonic TR experiments [77]. The authors discuss the basic theory of the closed time-reversal cavity (TRC) from the wave equation. In a homogeneous medium, as long as the field is enclosed inside of the cavity, the reconstructed result does not depend on the enclosure shape. Within the cavity, the field distribution has the spherical symmetry and the maximum spatial resolution is $\lambda/2$ limited by diffraction. Also the self-focusing is discussed in an inhomogeneous medium, showing that the focusing will be dependent on the time domain signal properties. A theoretical model in the weakly inhomogeneous medium is also described, indicating that time-reversal improves the focusing quality due to a correction term.

In a later development, a few another publications were specifically devoted to the TR theory of EM waves. In optics, Carminati *et al.* [81], developed a theory about the self-focusing TRC model in EM based on vector diffraction theory in frequency domain. The time-reversed electric field is related to the imaginary part of the outgoing dyadic Green function in the same medium. With microwaves, the TR operator, along with the decomposition of was explained in detail by Prada *et al*. [95]

Recently, a mutual impedance model was presented by Rosny *et al.* [96], claiming that the coupling between antennas would modify the focal spot. It starts with the relationship between TR and phase conjugate, clarifying that time reversing the odd monochromatic field is not equivalent to phase conjugate it. Then a six-dimension Green's

function is defined, with which impedance matrices related to TR are built. The far-field TR and TR by only electrical dipoles are discussed as examples.

4.2 Motivation

For biomedical application more specialized model is needed when body parts such as torso, neck or breast has to be described. In first approximation for such parts a cylindrical symmetry can be assumed what makes any calculations simpler. In general, we searched for a model, which could allow performing the TR process step by step, and, in addition, such model should provide analytical solutions when using only basic EM theory. In order to analyze and discuss the TR technique for biomedical application spatial focusing profile needs to be built from the field distribution calculated results, and, the most important figure of merit should be defined to quantify spatial and temporal focusing. Optimization study should be also conducted regarding the carrier frequency and the time domain signal shape. A set of parameters, such as loss, number of antennas, and bandwidth, is open for parametric studies.

4.3 EM Modelling of TR Process

4.3.1 Neck Model

To get a complete form analytical solution using the model, human tissues that have cylindrical symmetry, such as neck, breast, or torso, will be preferably considered. In this dissertation the neck model will be discussed in details as an example. The goal of our proposed model is to focus EM energy onto the tumor underneath the skin of the neck by using a set of time-reversal mirrors (TRM) outside around the neck. A torus consists of multiple antenna served as TRM is placed around the neck to apply TR in a real clinical therapy as shown in Figure 4-1 [97].

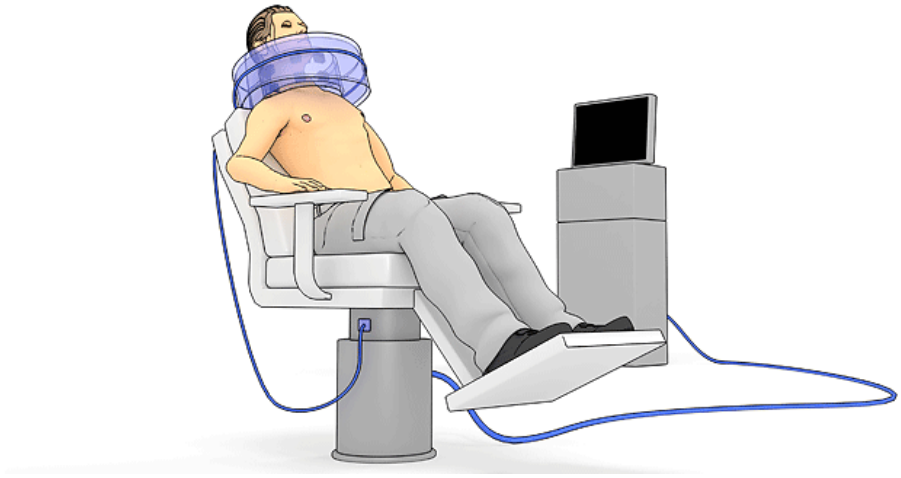

Figure 4-1 Clinical system for deep-seated tumors in head and neck region

Tumor inside the neck, the neck tissue, and torus surrounding the neck are creating a system, which needs to be analyzed. Following the configuration, the neck is modelled as a cylinder, with the tumor inside as a dipole antenna. Additionally, the torus outside is represented by dipole antennas as well, forming a ring concentric with the cylinder as shown in Figure 4-2.

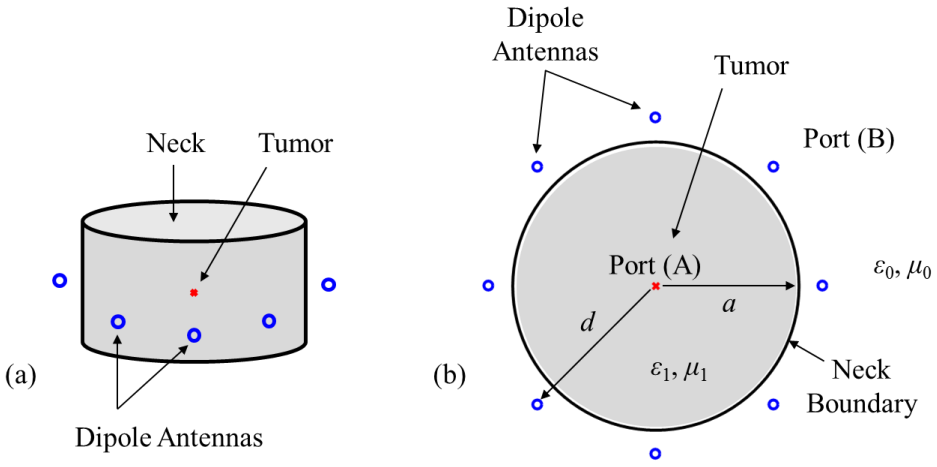

Figure 4-2 Neck modelled by a cylinder: (a) perspective view; (b) top view

The dipole inside the cylinder is denoted as Port (A), which acts as the original source. On the other side, the dipoles outside the cylinder, functioning as the TRMs, are tagged as Port (B). The cylinder has a radius of a, filled with homogeneous materials that

has permittivity ε_1 and permeability μ_1. The TRMs are put along a ring with radius d ($d > a$), i.e., the distance between the center of cylinder and each TRM is d. We assume outside of the cylinder the free space with permittivity ε_0 and conductivity μ_0.

The process of TR is performed in the following way: the original signal is transmitted at Port (A). The received signal which contains all the information from the reflection and scattering, called the "sona", is received at Port (B). The sona signal is then time-reversed and transmitted back at Port (B). According to the time-reversal characteristics of the Maxwell's equations, there should be focusing seen at Port (A) [98].

Based on the anthropometric data, the mean value of the neck circumference at the cricothyroid is 38 cm for male and 33 cm for female [99]. Therefore the radius of the cylinder is set to be 6 cm accordingly. The TRMs are positioned 1 cm away from the boundary of the cylinder. So the dimension of the neck model is that the cylinder has a radius of a = 6 [cm], surrounded by a ring of TRMs with a radius of d = 7 [cm].

From the work of Paulides *et al*. [100], a muscle-equivalent material [101] was employed to represent the neck. Hereby we are able to treat the homogeneous material inside the cylinder as muscle. To take into account its dispersion over frequency, the complex permittivity, including the dielectric constant and the polarization loss, is described by the 2nd order Cole-Cole model, plus the conductive loss

$$\varepsilon(\omega) = \varepsilon_\infty + \frac{\Delta\varepsilon_1}{1+\left(j\omega\tau_1\right)^{1-\alpha_1}} + \frac{\Delta\varepsilon_2}{1+\left(j\omega\tau_2\right)^{1-\alpha_2}} + \frac{\sigma}{j\omega\varepsilon_0}. \tag{4.1}$$

The parameters in (4.1) are selected from the muscle dielectric properties by Gabriel *et al.* [102, 103] shown in Table 4-1. The values of real and imaginary parts of the neck complex permittivity from 0 – 5 GHz are shown in Figure 4-3. The imaginary part is comparable to the real part at low frequencies as the conductive loss dominates. The loss reaches its

minimum at around 2 GHz. The cylinder is generally low loss at the frequency range from 1 GHz and up.

Table 4-1 Parameters of the 2nd order Cole-Cole model for the muscle in the neck

Material	ε_∞	$\Delta\varepsilon_1$	τ_1 [ps]	α_1	$\Delta\varepsilon_2$	τ_2 [ps]	α_2	σ [S/m]
Muscle	4.0	50.0	7.23	0.10	7000	353.68	0.10	0.2

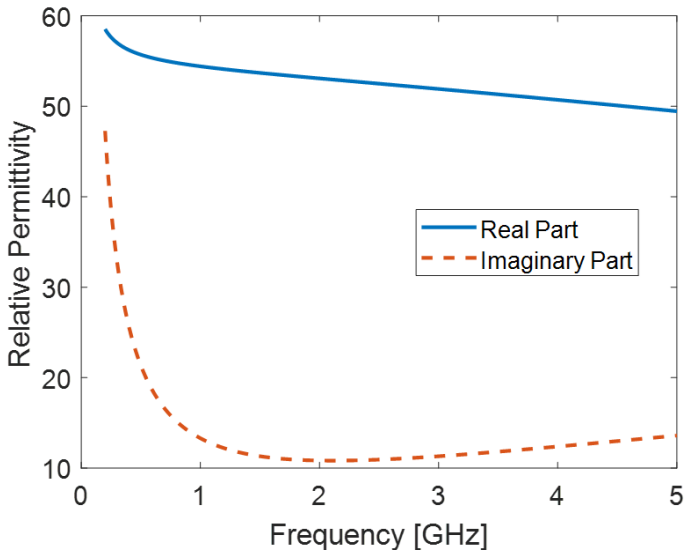

Figure 4-3 Complex permittivity of neck based on 2nd order Cole-Cole model

4.3.2 Dipole Scattering by a Dielectric Cylinder

If the length of the cylinder is extended to infinity, the field inside the cylinder could be solved analytically by turning it into a basic EM problem of that the incident wave from an electric dipole radiating in the free space is scattered by an infinite length dielectric cylinder as shown in Figure 4-4. The goal is to solve for the E-field $E(\rho, \phi, z)$ inside the cylinder ($\rho < a$).

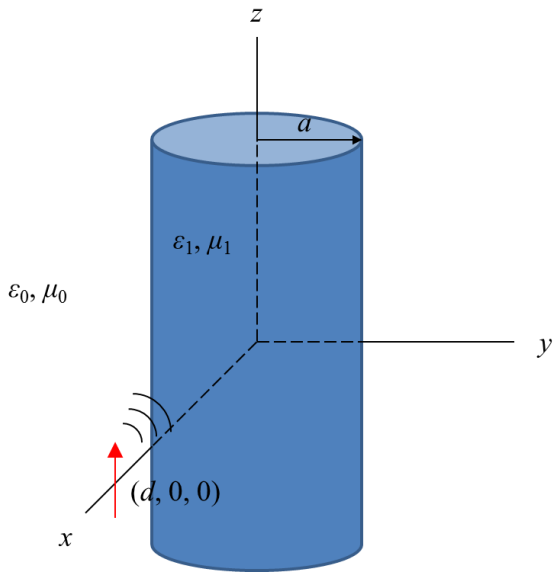

Figure 4-4 Dipole scattering by a dielectric cylinder

The A_z from a dipole radiating in free space at the origin is given by

$$A_{z0}^{i} = \frac{\mu_0}{8\pi j}\int_{-\infty}^{+\infty} H_0^{(2)}(k_{\rho 0}\rho)e^{-jk_z z}dk_z . \tag{4.2}$$

If the dipole is at (d, 0, 0), the magnetic vector potential is

$$A_{z0}^{i} = \frac{\mu_0}{8\pi j}\int_{-\infty}^{+\infty} H_0^{(2)}(k_{\rho 0}|\rho - d|)e^{-jk_z z}dk_z . \tag{4.3}$$

Using addition theorem ($\rho < d$), we have

$$A_{z0}^{i} = \frac{\mu_0}{8\pi j}\int_{-\infty}^{+\infty}\left(\sum_{n=-\infty}^{+\infty} H_n^{(2)}(k_{\rho 0}d)\,J_n(k_{\rho 0}\rho)\,e^{jn\phi}\right)e^{-jk_z z}dk_z . \tag{4.4}$$

There will be a scattered field when the incident field hits the boundary of the cylinder. Because it is a dielectric cylinder, the scattered field will have both A_z and F_z components,

$$\begin{aligned} A_{z0}^{s} &= \frac{\mu_0}{8\pi j}\int_{-\infty}^{+\infty}\left(\sum_{n=-\infty}^{+\infty} A_n(k_z)H_n^{(2)}(k_{\rho 0}\rho)\,e^{jn\phi}\right)e^{-jk_z z}dk_z \\ F_{z0}^{s} &= \frac{\mu_0}{8\pi j}\int_{-\infty}^{+\infty}\left(\sum_{n=-\infty}^{+\infty} B_n(k_z)H_n^{(2)}(k_{\rho 0}\rho)\,e^{jn\phi}\right)e^{-jk_z z}dk_z . \end{aligned} \tag{4.5}$$

Outside the dielectric cylinder, the total field is the incident plus the scattered field,

$$\begin{aligned} A_{z0} &= A_{z0}^{i} + A_{z0}^{s} \\ F_{z0} &= F_{z0}^{s}. \end{aligned} \tag{4.6}$$

Inside the dielectric cylinder, we consider the total field as follows:

$$\begin{aligned} A_{z1} &= \frac{\mu_0}{8\pi j}\int_{-\infty}^{+\infty}\left(\sum_{n=-\infty}^{+\infty} C_n\left(k_z\right) J_n(k_{\rho 1}\rho)\, e^{jn\phi}\right) e^{-jk_z z}\, dk_z \\ F_{z1} &= \frac{\mu_0}{8\pi j}\int_{-\infty}^{+\infty}\left(\sum_{n=-\infty}^{+\infty} D_n\left(k_z\right) J_n(k_{\rho 1}\rho)\, e^{jn\phi}\right) e^{-jk_z z}\, dk_z. \end{aligned} \tag{4.7}$$

Applying TE_z - TM_z decomposition results shown in (A.6) and (A.8), we can get the fields inside and outside the cylinder from (4.6) and (4.7) accordingly,

$$\begin{aligned} E_{z0} &= \frac{1}{j\omega\mu_0\varepsilon_0}\left(\frac{\partial^2}{\partial z^2} + k_0^{\,2}\right) A_{z0} & E_{z1} &= \frac{1}{j\omega\mu_1\varepsilon_1}\left(\frac{\partial^2}{\partial z^2} + k_1^{\,2}\right) A_{z1} \\ E_{\rho 0} &= \frac{1}{j\omega\mu_0\varepsilon_0}\frac{\partial^2 A_{z0}}{\partial\rho\partial z} - \frac{1}{\varepsilon_0\rho}\frac{\partial F_{z0}}{\partial\phi} & E_{\rho 1} &= \frac{1}{j\omega\mu_1\varepsilon_1}\frac{\partial^2 A_{z1}}{\partial\rho\partial z} - \frac{1}{\varepsilon_1\rho}\frac{\partial F_{z1}}{\partial\phi} \\ E_{\phi 0} &= \frac{1}{j\omega\mu_0\varepsilon_0\rho}\frac{\partial^2 A_{z0}}{\partial\phi\partial z} + \frac{1}{\varepsilon_0}\frac{\partial F_{z0}}{\partial\rho} & E_{\phi 1} &= \frac{1}{j\omega\mu_1\varepsilon_1\rho}\frac{\partial^2 A_{z1}}{\partial\phi\partial z} + \frac{1}{\varepsilon_1}\frac{\partial F_{z1}}{\partial\rho} \\ H_{z0} &= \frac{1}{j\omega\mu_0\varepsilon_0}\left(\frac{\partial^2}{\partial z^2} + k_0^{\,2}\right) F_{z0} & H_{z1} &= \frac{1}{j\omega\mu_1\varepsilon_1}\left(\frac{\partial^2}{\partial z^2} + k_1^{\,2}\right) F_{z1} \\ H_{\rho 0} &= \frac{1}{j\omega\mu_0\varepsilon_0}\frac{\partial^2 F_{z0}}{\partial\rho\partial z} + \frac{1}{\mu_0\rho}\frac{\partial A_{z0}}{\partial\phi} & H_{\rho 1} &= \frac{1}{j\omega\mu_1\varepsilon_1}\frac{\partial^2 F_{z1}}{\partial\rho\partial z} + \frac{1}{\mu_1\rho}\frac{\partial A_{z1}}{\partial\phi} \\ H_{\phi 0} &= \frac{1}{j\omega\mu_0\varepsilon_0\rho}\frac{\partial^2 F_{z0}}{\partial\phi\partial z} - \frac{1}{\mu_0}\frac{\partial A_{z0}}{\partial\rho} & H_{\phi 1} &= \frac{1}{j\omega\mu_1\varepsilon_1\rho}\frac{\partial^2 F_{z1}}{\partial\phi\partial z} - \frac{1}{\mu_1}\frac{\partial A_{z1}}{\partial\rho}. \end{aligned} \tag{4.8}$$

Match the boundary condition, we get 4 equations as follows:

$$\begin{aligned} E_{z0}(\rho = a^{+}) &= E_{z1}(\rho = a^{-}) \\ E_{\phi 0}(\rho = a^{+}) &= E_{\phi 1}(\rho = a^{-}) \\ H_{z0}(\rho = a^{+}) &= H_{z1}(\rho = a^{-}) \\ H_{\phi 0}(\rho = a^{+}) &= H_{\phi 1}(\rho = a^{-}). \end{aligned} \tag{4.9}$$

The 4 unknowns A_n, B_n, C_n, and D_n can be solved with the 4 equations in (4.9).

4.3.3 2D Simplification – Scattering from a Line Current

The problem can be simplified by substituting the dipole with an infinite length constant line current source. It becomes a 2D line current source scattering problem with no z variation as shown in Figure 4-5. There will be no F_z, only A_z component after scattering.

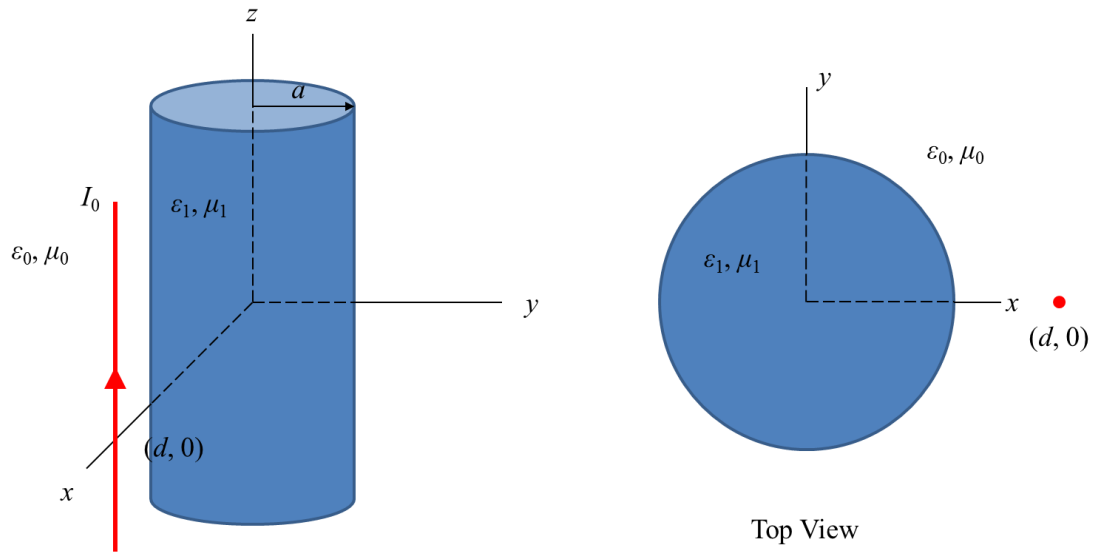

Figure 4-5 Line current source scattering by a dielectric cylinder

Similarly, the A_z from a constant line current source radiating at origin in free space is given by

$$A_{z0}^{i} = \frac{\mu I_0}{4j} H_0^{(2)}\left(k_0 \rho\right), \tag{4.10}$$

where I_0 is the magnitude of current per unit length in A/m flowing on the line source, which remains constant in the calculation.

Using addition theorem ($\rho < d$), the incident A_z from a line current at (d, 0, 0) is

$$A_{z0}^{i} = \frac{\mu I_0}{4j} \sum_{n=-\infty}^{+\infty} H_n^{(2)}\left(k_0 d\right) J_n\left(k_0 \rho\right) e^{jn\phi} \ . \tag{4.11}$$

Scattered field can be found with only A_z component,

$$A_{z0}^{s} = \frac{\mu I_0}{4j} \sum_{n=-\infty}^{+\infty} A_n H_n^{(2)}\left(k_0 \rho\right) e^{jn\phi} \ . \tag{4.12}$$

Total field outside cylinder is

$$A_{z0} = A_{z0}^{i} + A_{z0}^{s} \, . \tag{4.13}$$

Total field inside cylinder is

$$A_{z1} = \frac{\mu I_0}{4j} \sum_{n=-\infty}^{+\infty} B_n J_n\left(k_1 \rho\right) e^{jn\phi} \, . \tag{4.14}$$

From the vector potential we can get the E and H field,

$$\begin{aligned}
E_{z0} &= \frac{1}{j\omega\mu_0\varepsilon_0}\left(\frac{\partial^2}{\partial z^2} + k_0^{\,2}\right) A_{z0} & E_{z1} &= \frac{1}{j\omega\mu_1\varepsilon_1}\left(\frac{\partial^2}{\partial z^2} + k_1^{\,2}\right) A_{z1} \\
E_{\rho 0} &= \frac{1}{j\omega\mu_0\varepsilon_0}\frac{\partial^2 A_{z0}}{\partial\rho\partial z} & E_{\rho 1} &= \frac{1}{j\omega\mu_1\varepsilon_1}\frac{\partial^2 A_{z1}}{\partial\rho\partial z} \\
E_{\phi 0} &= \frac{1}{j\omega\mu_0\varepsilon_0\rho}\frac{\partial^2 A_{z0}}{\partial\phi\partial z} & E_{\phi 1} &= \frac{1}{j\omega\mu_1\varepsilon_1\rho}\frac{\partial^2 A_{z1}}{\partial\phi\partial z} \\
H_{z0} &= 0 & H_{z1} &= 0 \\
H_{\rho 0} &= \frac{1}{\mu_0\rho}\frac{\partial A_{z0}}{\partial\phi} & H_{\rho 1} &= \frac{1}{\mu_1\rho}\frac{\partial A_{z1}}{\partial\phi} \\
H_{\phi 0} &= -\frac{1}{\mu_0}\frac{\partial A_{z0}}{\partial\rho} & H_{\phi 1} &= -\frac{1}{\mu_1}\frac{\partial A_{z1}}{\partial\rho}.
\end{aligned} \tag{4.15}$$

It is given that tangential E and H field are continuous by matching the boundary condition,

$$\begin{aligned}
E_{z0}(\rho = a^+) &= E_{z1}(\rho = a^-) \\
H_{\phi 0}(\rho = a^+) &= H_{\phi 1}(\rho = a^-)
\end{aligned} \tag{4.16}$$

or

$$\begin{aligned}
A_{z0} &= A_{z1} \\
\frac{1}{\mu_0}\frac{\partial A_{z0}}{\partial\rho} &= \frac{1}{\mu_1}\frac{\partial A_{z1}}{\partial\rho}.
\end{aligned} \tag{4.17}$$

So we get 2 equations as follows:

$$\sum_{n=-\infty}^{+\infty} H_n^{(2)}(k_0 d) J_n(k_0 a) e^{jn\phi} + \sum_{n=-\infty}^{+\infty} A_n H_n^{(2)}(k_0 a) e^{jn\phi} = \sum_{n=-\infty}^{+\infty} B_n J_n(k_1 a) e^{jn\phi}$$
$$\frac{k_0}{\mu_0}\left[\sum_{n=-\infty}^{+\infty} H_n^{(2)}(k_0 d) J_n'(k_0 a) e^{jn\phi} + \sum_{n=-\infty}^{+\infty} A_n H_n'^{(2)}(k_0 a) e^{jn\phi}\right] = \frac{k_1}{\mu_1}\sum_{n=-\infty}^{+\infty} B_n J_n'(k_1 a) e^{jn\phi}. \quad (4.18)$$

Matching each term in the Fourier series, we have

$$H_n^{(2)}(k_0 d) J_n(k_0 a) + A_n H_n^{(2)}(k_0 a) = B_n J_n(k_1 a)$$
$$\frac{k_0}{\mu_0}\left[H_n^{(2)}(k_0 d) J_n'(k_0 a) + A_n H_n'^{(2)}(k_0 a)\right] = \frac{k_1}{\mu_1} B_n J_n'(k_1 a). \quad (4.19)$$

From (4.19) we get the solution for A_n and B_n,

$$A_n = \frac{\eta_0 J_n'(k_1 a) H_n^{(2)}(k_0 d) J_n(k_0 a) - \eta_1 J_n(k_1 a) H_n^{(2)}(k_0 d) J_n'(k_0 a)}{\eta_1 J_n(k_1 a) H_n'^{(2)}(k_0 a) - \eta_0 J_n'(k_1 a) H_n^{(2)}(k_0 a)}$$
$$B_n = \frac{\eta_1 H_n'^{(2)}(k_0 a) H_n^{(2)}(k_0 d) J_n(k_0 a) - \eta_1 H_n^{(2)}(k_0 a) H_n^{(2)}(k_0 d) J_n'(k_0 a)}{\eta_1 J_n(k_1 a) H_n'^{(2)}(k_0 a) - \eta_0 J_n'(k_1 a) H_n^{(2)}(k_0 a)}. \quad (4.20)$$

According to the Green's function, i.e., the E-field inside the cylinder ($\rho < a$) due to a 1 A current source, as a function of space and frequency can be written as

$$G(\rho, \phi, f) = -\frac{\omega\mu I_0}{4}\sum_{n=-\infty}^{+\infty} B_n J_n(k_1\rho) e^{jn\phi}. \quad (4.21)$$

Therefore, the Green's function can be used to solve for the E-field inside the cylinder in the 2D neck model.

4.3.4 Validation of the Model

If we set relative permittivity and permeability inside the cylinder equal to 1, the line current source radiating at (d, 0) will be "scattered" by a "free space" cylinder as shown in Figure 4-6(a). Another way to describe such problem is to consider a line current source radiating in the free space as shown in Figure 4-6(b). By reciprocity, the two methods, line current source scattering and radiating, should yield the same results. Therefore it is a very

good way to validate the analytical model by solving the same problem from two different perspectives.

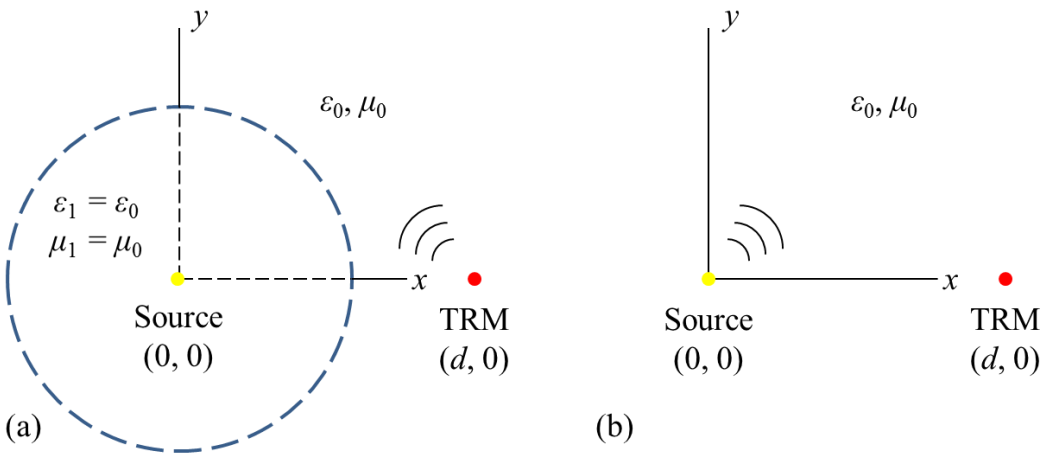

Figure 4-6 Free space problem: (a) line current source scattering by a free space cylinder; (b) line current source radiating in free space

The vector potential from a line current source radiating at the origin in the free space is shown in (4.10), therefore we can get the E-field from the radiation,

$$E_z^{rad} = -\frac{\omega\mu I_0}{4} H_0^{(2)}(k_0\rho). \tag{4.22}$$

The E-field at the observation point (d, 0) is

$$E_z^{rad}(d,0) = -\frac{\omega\mu I_0}{4} H_0^{(2)}(k_0 d). \tag{4.23}$$

We will look at the problem in the other way using the line current source scattering model. From (4.21), E-field at the origin due to the source at (d, 0) is

$$E_z^{sca}(0,0) = -\frac{\omega\mu I_0}{4} \sum_{n=-\infty}^{+\infty} B_n J_n(0). \tag{4.24}$$

We know that $J_n(0) = \begin{cases} 1, & n = 0 \\ 0, & n \neq 0 \end{cases}$, so we can modify the equation as:

$$E_z^{sca}(0,0) = -\frac{\omega\mu I_0}{4} B_0. \tag{4.25}$$

Set $\varepsilon_1 = \varepsilon_0$, $\mu_1 = \mu_0$, then $k_1 = k_0$, $\eta_1 = \eta_0$, the results in (4.20) now becomes

$$\begin{aligned} B_0 &= \frac{\eta_1 H_0^{'(2)}(k_0 a) H_0^{(2)}(k_0 d) J_0(k_0 a) - \eta_1 H_0^{(2)}(k_0 a) H_0^{(2)}(k_0 d) J_0^{'}(k_0 a)}{\eta_1 J_0(k_1 a) H_0^{'(2)}(k_0 a) - \eta_0 J_0^{'}(k_1 a) H_0^{(2)}(k_0 a)} \\ &= \frac{\eta_0 H_0^{'(2)}(k_0 a) J_0(k_0 a) - \eta_0 H_0^{(2)}(k_0 a) J_0^{'}(k_0 a)}{\eta_0 J_0(k_0 a) H_0^{'(2)}(k_0 a) - \eta_0 J_0^{'}(k_0 a) H_0^{(2)}(k_0 a)} \cdot H_0^{(2)}(k_0 d) = H_0^{(2)}(k_0 d). \end{aligned} \tag{4.26}$$

Hence the E-field from the scattering at the origin is

$$E_z^{sca}(0,0) = -\frac{\omega\mu I_0}{4} H_0^{(2)}(k_0 d). \tag{4.27}$$

The line current source scattering model has been validated since the two methods give the same results in (4.23) and (4.27).

4.4 Temporal Focusing Analysis

4.4.1 TR Process in Analytical Model

The TR process can be divided into two problems in the analytical model: the time-forward step and the time-reverse step.

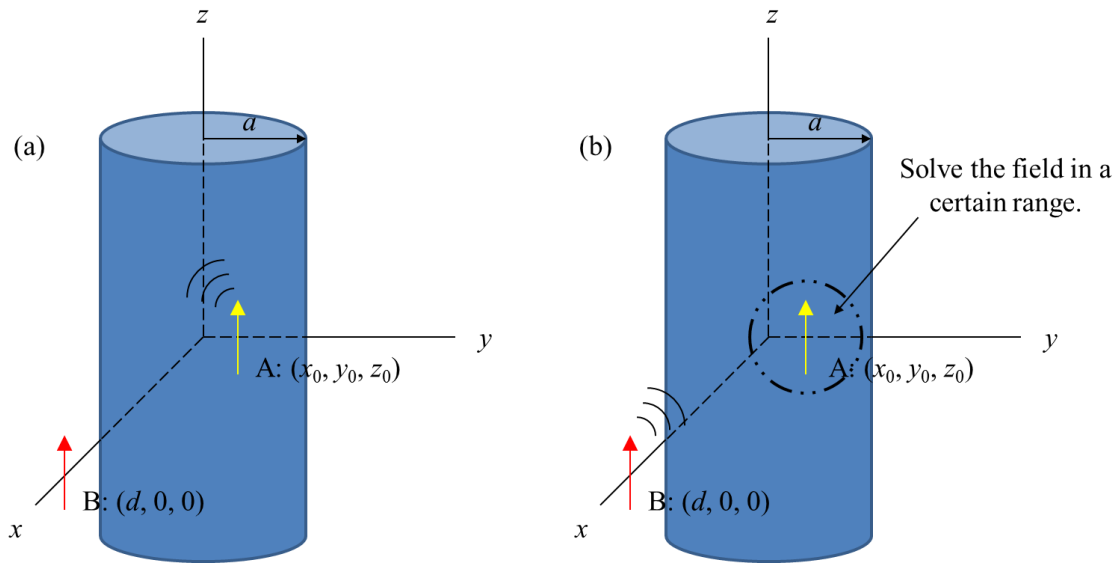

Figure 4-7 TR process in the analytical model: (a) the time-forward step; (b) the time-reverse step

In the forward step as shown in Figure 4-7(a), the antenna at Port (A) is transmitting the original signal. The goal is to find the received sona signal at Port (B). Instead of solving the problem directly in time domain, it is much easier to solve it in the frequency domain with the Green's function. The Green's function in the forward step is the E-field at Port (B) produced by a 1A current source applied at the transmitting antenna at Port (A).

On the other way, by changing the roles of the antennas, the backward step consists of transmitting the time-reversed sona signal back from Port (B) to Port (A) as it is shown in Figure 4-7(b). This time our aim is to find the reconstructed signal over the observation space at and around Port (A). In other words, we need to find the Green's function, or the E-field distribution of the receiving antenna at Port (A). The figure of merit can be defined to quantify how well the spatial focusing is correlated on the field distribution. Also the temporal focusing can be quantified by calculating the cross-correlation between the time domain reconstructed signal at Port (A) and the original signal sent from Port (A) in the forward step.

From reciprocity, the field at Port (B) due to the source at Port (A) is the same as the field at Port (A) due to the source at Port (B). So the Green's function from (A) to (B) is the same as the Green's function from (B) to (A). Hence the forward step problem becomes part of the backward step problem, which is a dipole scattering problem. The solution of the Green's function is shown in (4.21).

A flow chart in Figure 4-8 shows how the Green's function in the frequency domain is utilized to solve the time domain reconstructed signal back at the Port (A).

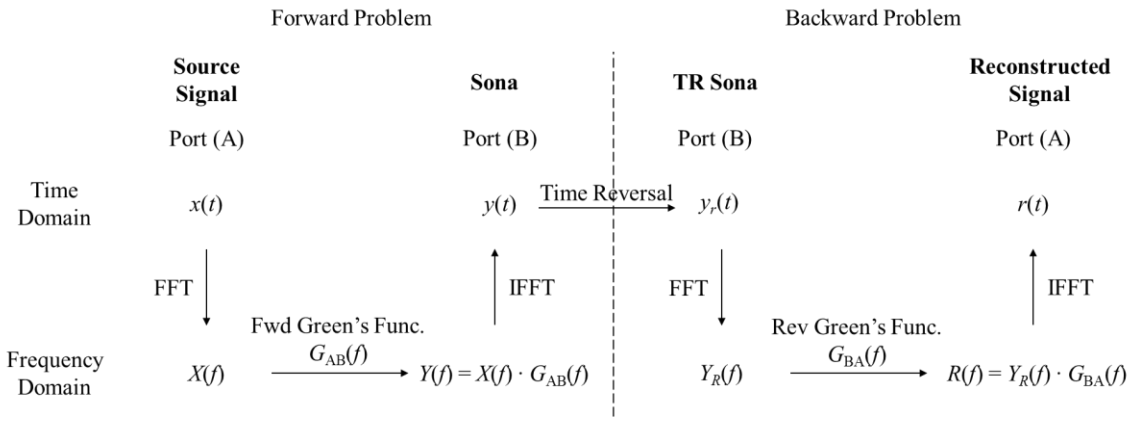

Figure 4-8 Flow chart of solving time domain reconstructed signal back at the source point

By taking the fast Fourier transform (FFT), the time domain signal $x(t)$ at Port (A) is transformed into the frequency domain signal $X(f)$. The sona signal at Port (B) in the frequency domain, $Y(f)$, is obtained by multiplying $X(f)$ by the forward Green's function $G_{AB}(f)$. The forward problem is solved by taking the inverse fast Fourier transform (IFFT) of $Y(f)$ to get the sona signal $y(t)$ in the time domain. Then the time-reversed sona $y_r(t)$, transformed into $Y_R(f)$ in the frequency domain by FFT, is transmitted from Port (B). The reconstructed signal $R(f)$ in the frequency domain can be calculated from the product of $Y_R(f)$ and $G_{BA}(f)$, the reverse Green's function from Port (B) to Port (A). After the IFFT, the final result $r(t)$ shows the reconstructed signal in the time domain at Port (A). The time domain reconstructed signal $r(t)$ is then compared to the original signal $x(t)$ to confirm the temporal focusing property of TR.

4.4.2 Properties of the Reconstruction

To evaluate the temporal focusing quality from TR in the 2D analytical model, a 28 ns Gaussian pulse at 2.4 GHz, with bandwidth 100 MHz is transmitted from the antenna at center of the cylinder. First a single antenna is placed on the x-axis 7 cm away from the source, working as a TRM. The forward step is done as shown in Figure 4-9.

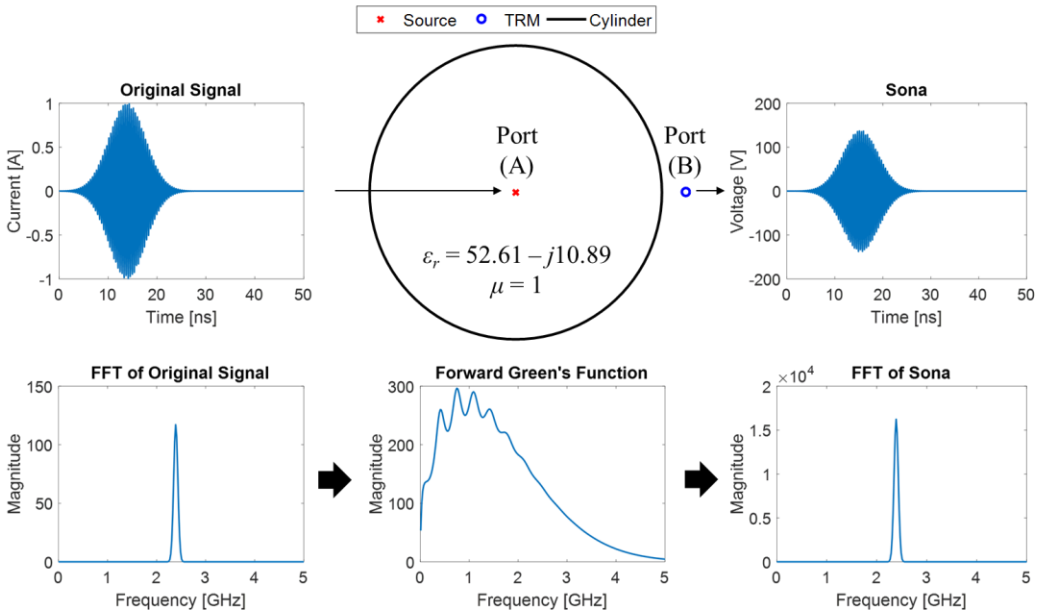

Figure 4-9 The forward step: the sona signal is solved from the forward Green's function in frequency domain

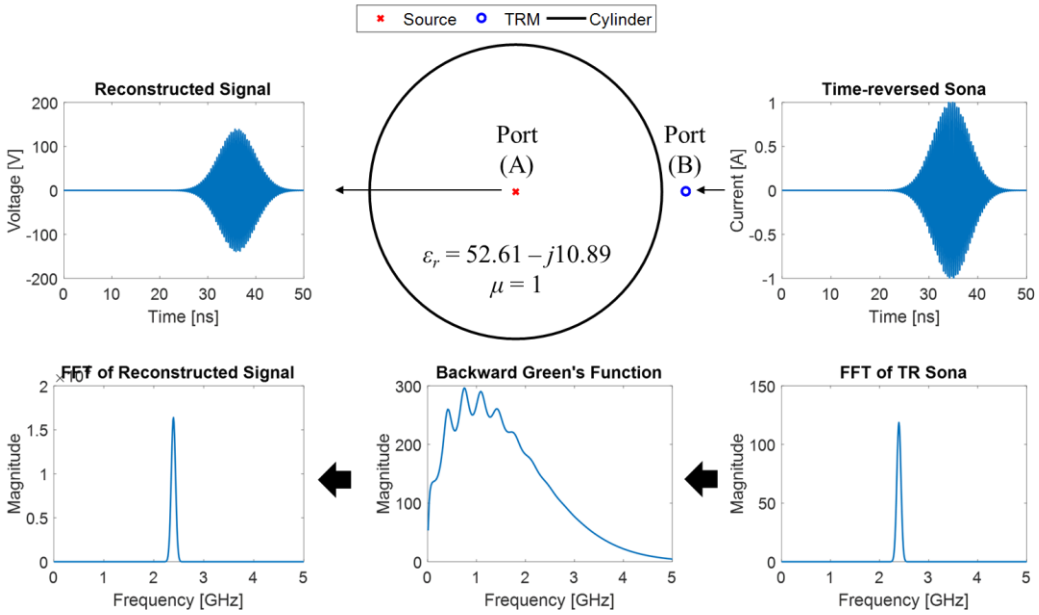

Figure 4-10 The backward step: the reconstructed signal is solved from the backward Green's function in frequency domain

The sona signal acts like the direct propagation of the source signal from Port (A) to Port (B), since the Green's function does not have much influence on the source signal spectrum. The received sona is in voltage because it is calculated from the electric field.

Considering the fact that the temporal focusing quality is determined by the resemblance of the shape in a relative sense, the amplitude of the signal is not necessarily to be quantified. Hereby the sona is time-reversed, normalized and converted back as a current source to be utilized in the backward step, which is shown in Figure 4-10.

By reciprocity, the backward Green's function is identical to the forward Green's function, again making neglegible modification to the TR sona during the backward step. After the entire TR process, it is seen that the time-revered version of the reconstructed signal has the similar shape to the original signal. To quantify the temporal focusing, the cross-correlation [76] between the original signal and the time-reversed reconstructed signal is calculated as shown in Figure 4-11.

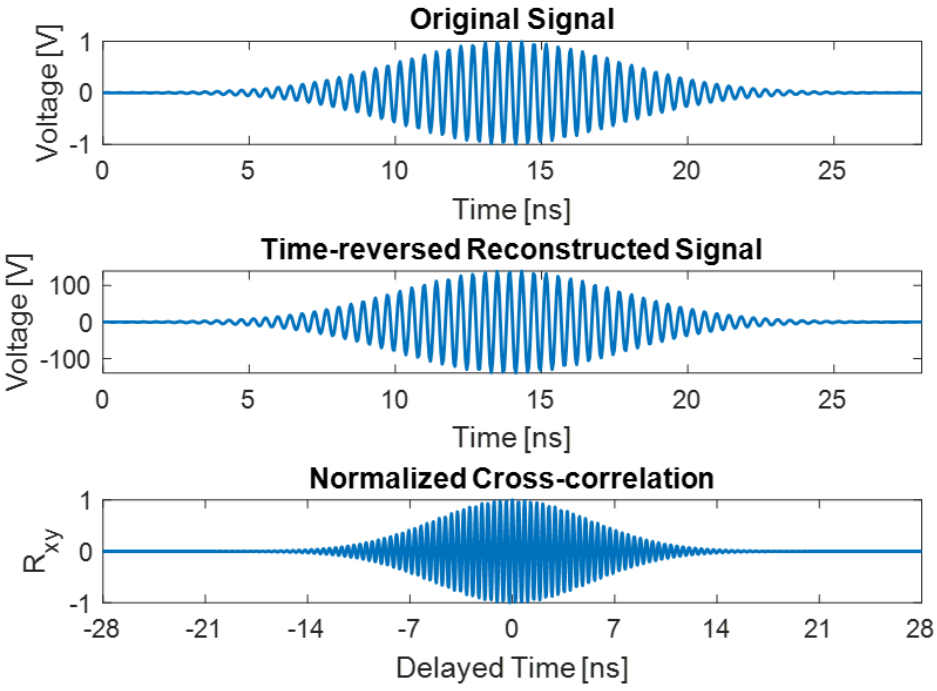

Figure 4-11 The original signal, the time-reversed reconstructed signal, and the normalized cross-correlation between them for a Gaussian shape pulse

The cross-correlation shows the peak at $\tau = 0$, which means the two signals are best correlated with no delay. Furthermore, the symmetry is recognized with respect to the *y*-axis, featuring the same correlation behavior on both sides. The temporal focusing property of TR is by this means proved assuming the results that the reconstructed signal has the similar shape to the original signal.

To better illustrate the temporal focusing of TR, an asymmetric signal, a damped sine wave

$$x(t) = \sin(2\pi ft)e^{-t/4} \tag{4.28}$$

at 2.4 GHz is used as the source signal. The reconstruction process is shown in Figure 4-12. It can be clearly seen that the reconstructed signal is the time-reversed version of the original signal even if it is asymmetric.

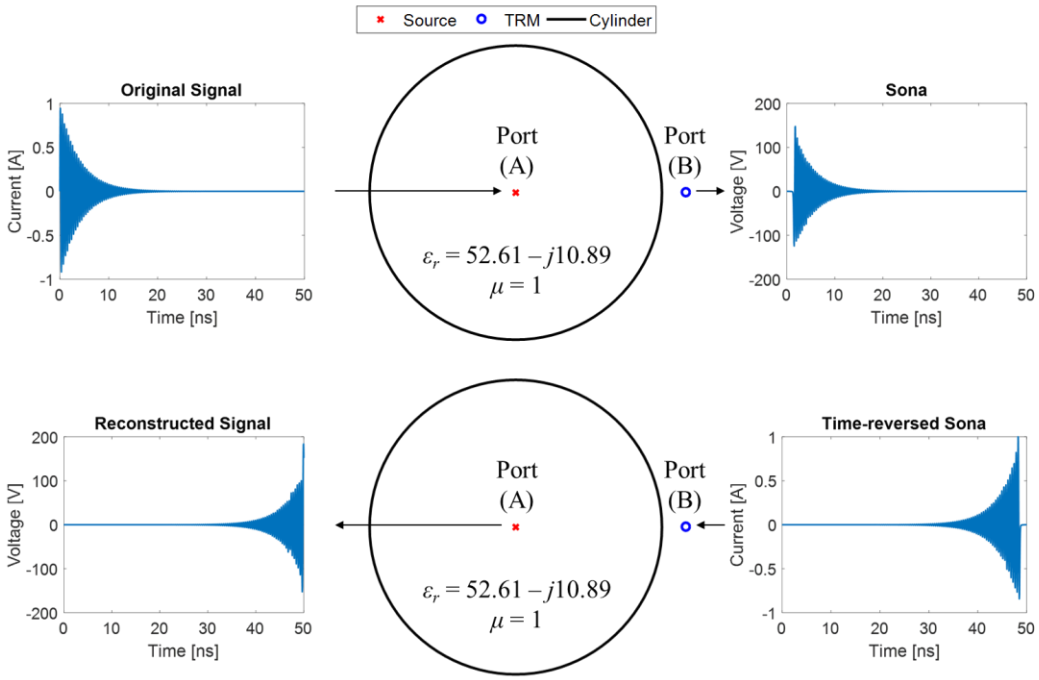

Figure 4-12 The reconstruction process of an asymmetric damped sine shape signal

4.5 Spatial Focusing Analysis

4.5.1 Build Spatial Focusing Profile

The temporal focusing of TR has been quantified by comparing the reconstructed signal and the original signal at the source point following the flow chart in Figure 4-8. Besides the temporal focusing analysis at a single point, we are more concerned about targeting the energy selectively over the space. As mentioned in the backward step description, the E-field needs to be solved not only at the original source point, but also within a certain range of interest. In the neck model, we are interested in energy or SAR distribution inside the entire neck region, i.e., the area inside the 2D cylinder.

So the spatial focusing profile can be built by calculating the time domain reconstructed signals at each point inside the 2D cylinder following the flow chart in Figure 4-13. The original signal $x(t)$ is transformed into the frequency domain $X(f)$ by FFT, followed by going through the forward Green's function $G^{fwd}(f)$ for each receiving antenna. Similarly, the sona signal received at each TRM is time-reversed, then reemitted back though the reverse Green's function. Different from the temporal focusing analysis, the reverse Green's function $G^{rev}(\rho, \phi, f)$ is now a function of space and frequency. So the reconstructed signal contributed from each TRM obtained is also a function of space and time. Adding these signals together in time domain, we can get the total reconstructed signal over the entire 2D cylinder.

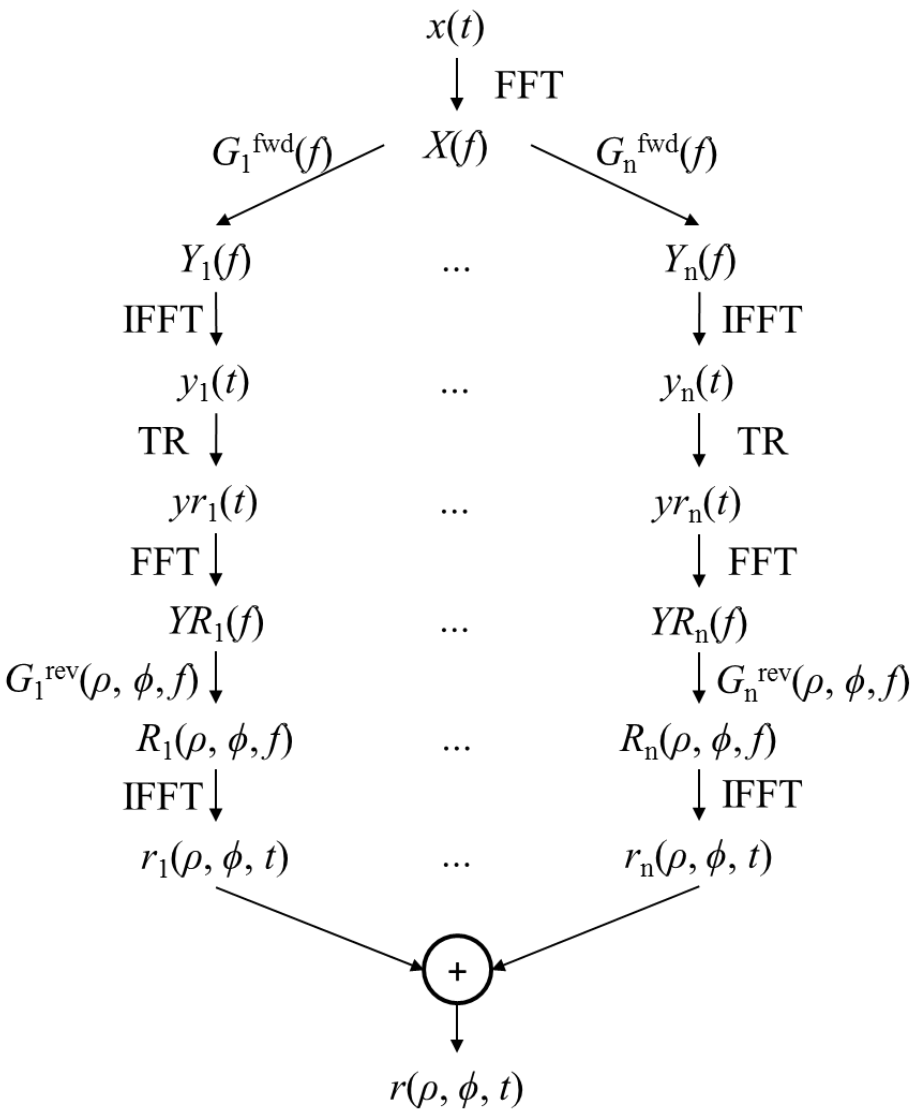

Figure 4-13 Flow chart of solving the time domain reconstructed signal over space from multiple antennas

The total energy as a function of space can be found by integrating the square of time domain reconstructed signal over time,

$$E(\rho,\phi) = \int \left| r(\rho,\phi,t) \right|^2 dt = \int \left| \sum_n r_n(\rho,\phi,t) \right|^2 dt \,. \tag{4.29}$$

If we define the density of the neck as D, the SAR over space inside the neck can be calculated from the reconstructed signal $R(\rho, \phi, f)$ in the frequency domain as

$$SAR(\rho,\phi)=\frac{\sigma E(\rho,\phi)}{2D}=\frac{\frac{\sigma}{2}\int_{-\infty}^{\infty}\left|\sum_n R_n(\rho,\phi,f)\right|^2 df}{D}. \tag{4.30}$$

The results (4.29) and (4.30) can be connected by Parseval's theorem,

$$\int_{-\infty}^{\infty}|r(t)|^2\,dt=\int_{-\infty}^{\infty}|R(f)|^2\,df\ . \tag{4.31}$$

Since the neck is taken as a homogeneous material with constant conductivity and density in the analytical model, the SAR and energy results will be differed by merely a normalization coefficient. So in the rest of this chapter, only the energy distribution will be further discussed.

4.5.2 Focusing at the Cylinder Center

If the original source is put at the center of the cylinder, and the TRMs are equally distributed in phase surrounding the cylinder, the 2D scattering problem will be downgraded to a 1D problem with no ϕ-variation. The Green's function between the source and each TRM will be the same, thus reducing the degree of freedom and giving us a way to conduct asymptotic study. Taking the advantage of the symmetry, the energy distribution from a closed TRC could be expressed in a closed form. Based on the asymptotic results, we could then discuss how to define the hot spot size and what kind of energy ratio constraints to follow in the clinical situation.

4.5.2a Asymptotic Study

The goal of the asymptotic study is to solve the limit of the energy distribution derived in (4.29) analytically as the number of TRMs *n* approaches infinity,

$$E_{asym}(\rho,\phi)=\lim_{n\to\infty}\int\left|\sum_n r_n(\rho,\phi,t)\right|^2 dt \tag{4.32}$$

or in the frequency domain from the Parseval's theorem in (4.31),

$$E_{asym}(\rho,\phi) = \lim_{n\to\infty} \int \left| \sum_n R_n(\rho,\phi,f) \right|^2 df \ . \tag{4.33}$$

It represents the spatial focusing limit as the TRMs are now distributed continuously around the cylinder to form a closed TRC as shown in Figure 4-14.

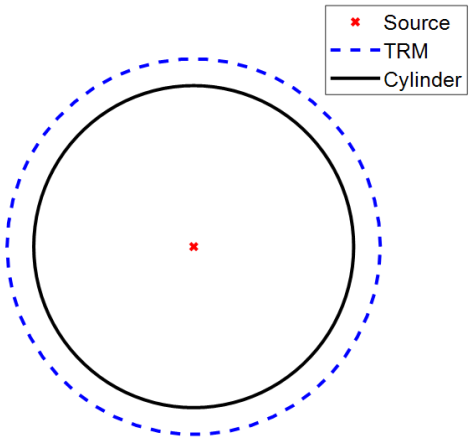

Figure 4-14 Focusing at the center with a closed TRC

Since the TRMs are placed equally around the cylinder, the field distribution will be centrosymmetric. The field can be expressed in terms of only ρ with no ϕ-variation. From the equivalence principle, we can always replace the actual sources in a region by equivalent sources at the boundary of a closed surface [104]. Therefore the radius of the closed TRC can be selected arbitrarily. If the TRC reduces to a point source at the center, the E-field inside the cylinder due to the continuous TRM can be converted into solving the Dirac Green's function of Helmholtz equation in the cylindrical coordinates,

$$\nabla^2 G(\rho) + k^2 G(\rho) = -\delta(\rho) \, . \tag{4.34}$$

The solution can be written in the closed form as

$$G(\rho) = J_0(k\rho) \, . \tag{4.35}$$

So if the radius of the TRC is d, then $G(d, f)$ is the forward Green's function, and $G(\rho, f)$ is the reverse Green's function. Following the flow chart in Figure 4-13, the asymptotic energy point density on the radial direction inside the cylinder is

$$\begin{aligned} U(\rho,\phi) &= \int \left| X(f)G(d,f)G(\rho,f) \right|^2 df \\ &= \int \left| X(f)J_0\left(k(f)\cdot d\right) \right|^2 \left| J_0\left(k(f)\cdot \rho\right) \right|^2 df. \end{aligned} \tag{4.36}$$

It proves that the radius of the TRC does not affect the normalized energy because r stays in the coefficient and the reverse Green's function is independent of r. Let $X(f)$ be a single frequency signal at 2.4 GHz, the asymptotic energy as a function of ρ is shown in Figure 4-15.

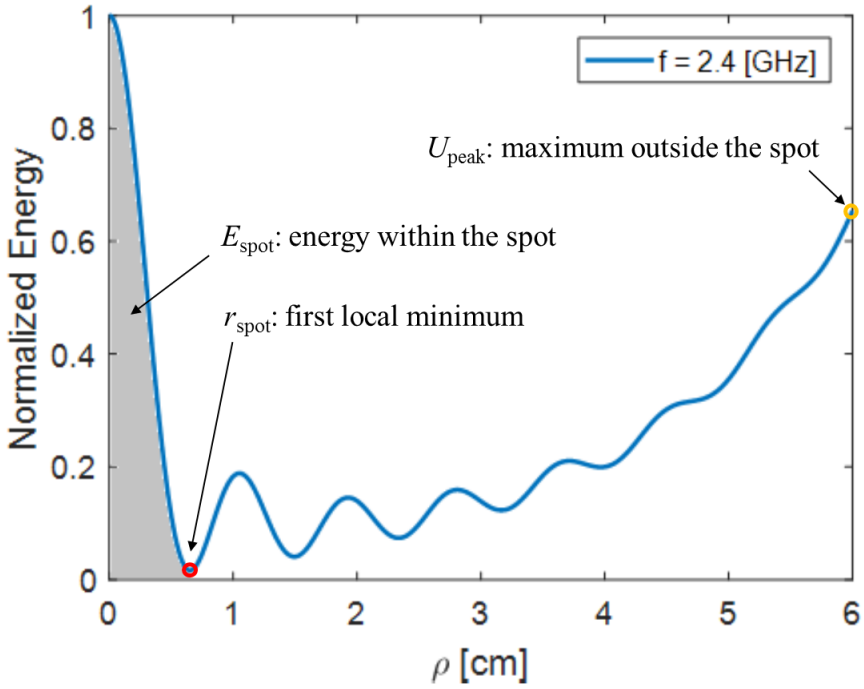

Figure 4-15 Normalized energy distribution along the radial direction

The function has the oscillating property like the Bessel function. If the cylinder is lossless, the wavenumber k is a real number, the energy will decay towards zero as the

wave propagating. However, the energy distribution will behave differently as k become complex because of the lossy cylinder, the values in the tail would rise up [105].

4.5.2b Focal Spot Size and Energy Ratio Constraints

In hyperthermia we are concerned about targeting the energy precisely on the tumor. Therefore the focal area is an important parameter to consider as it indicates how well the spatial focusing is. From Figure 4-15 we define the focal spot radius r_{spot} as the first local minimum of the energy distribution function. Based on this definition, the focal spot radius per wavelength *versus* frequency up to 5 GHz is plotted in Figure 4-16.

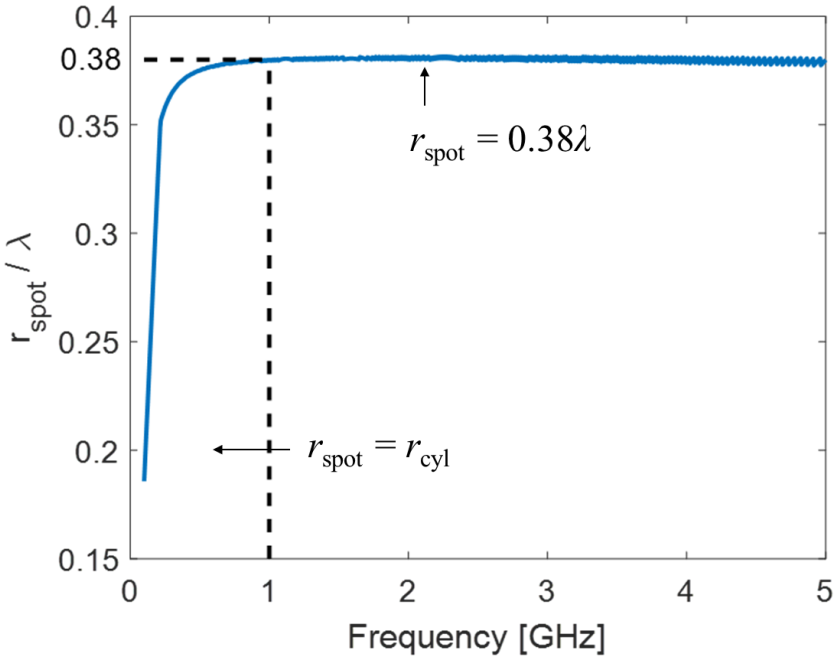

Figure 4-16 Focal spot radius per wavelength *vs* frequency

At lower frequency, the energy decreases monotonically within the cylinder range before it reaches its minimum, so the spot radius is equal to the cylinder radius. As the frequency increases, the wavelength is getting shorter. As a result, the ratio between spot size and wavelength keeps increasing to the point where the cylinder radius is equal to the first zero of the Bessel $J_0(x)$ function. After the point, the focal spot radius per wavelength

remains constant. The reason is that the spot radius r_{spot} we defined is the first local minimum of the energy distribution function, which corresponds to the first zero x_0 of the Bessel $J_0(x)$ function as it appears in the reverse Green's function. The reverse Green's function is in terms of $k\rho$, therefore the first zero can be represented as

$$x_0 = kr_{\text{spot}} = 2.4048\,. \tag{4.37}$$

We can make the assumption that k is equal to $2\pi/\lambda$ in a low loss cylinder, hence the spatial resolution from TR in the model is

$$r_{\text{spot}} = \frac{2.4048}{2\pi}\lambda = 0.38\lambda\,. \tag{4.38}$$

It is beyond the diffraction limit because the focusing is due to the near-field EM waves.

Besides increasing the spatial resolution, there are certain energy constraints that needs to follow in the real clinical applications. The desired way to conduct hyperthermia is to maximize the applied total power deposited into the tumor, at the same minimizing spurious hot spots outside of the tumor. So it gives us two perspectives to define the possible energy constraints. One way is to take a look at the proportion of energy inside the spot. Following the definition of focal spot radius shown in Figure 4-15, the total energy inside the focal spot can be expressed by an integration calculated over the r_{spot}. The total energy inside the cylinder can be found in similar way. Therefore the spot energy ratio, which is the energy inside the spot over the total energy inside the cylinder, should be higher than a certain threshold θ_{sp},

$$\frac{E_{\text{spot}}}{E_{\text{cyl}}} = \frac{\int_0^{r_{\text{spot}}} U(\rho)\rho\, d\rho}{\int_0^{r_{\text{cyl}}} U(\rho)\rho\, d\rho} > \theta_{sp}\,. \tag{4.39}$$

The other way is to reduce the peak energy outside the spot. Then the peak energy ratio between the maximum energy outside the focal spot radius and the energy at the source point should be less than a clinically specified threshold θ_p,

$$\frac{U_{\text{peak}}}{U_s} < \theta_p . \tag{4.40}$$

Now the TR spatial focusing analysis becomes a constrained optimization problem. The goal is to minimize the spot size under energy ratio constraints in (4.39) and (4.40) by optimizing the center frequency and bandwidth.

4.5.2c Optimizing the Frequency and Bandwidth

The operation frequency is the decisive factor of the spot size and energy ratio. Considering the problem in the frequency domain, the asymptotic energy at a single frequency is calculated from (4.36). A family of curves demonstrating normalized energy as a function of position at different frequencies are shown in Figure 4-17.

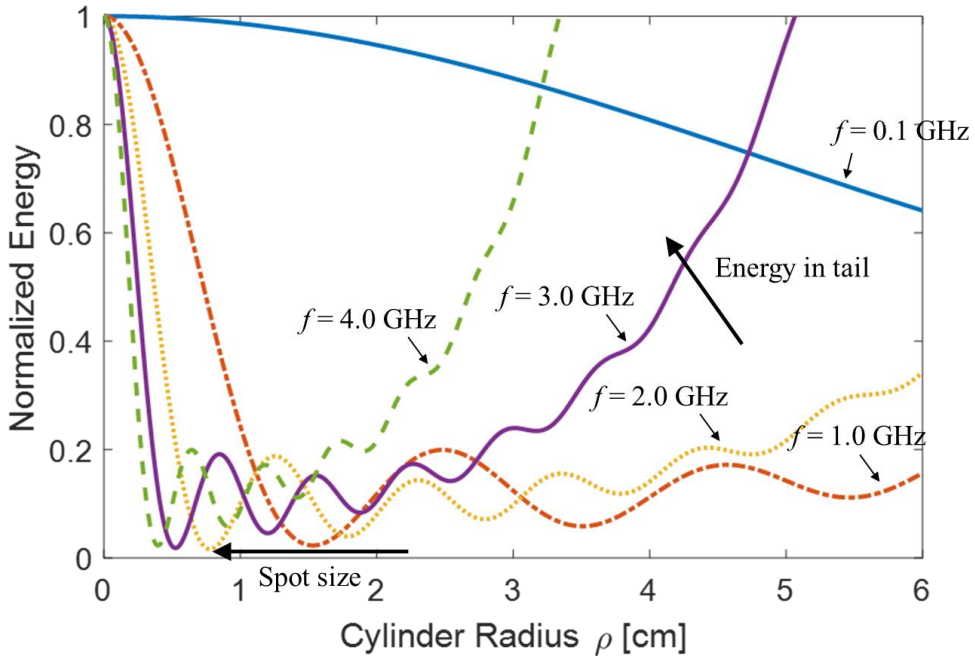

Figure 4-17 Normalized energy distribution at different frequencies

Generally all the energy distribution curves are following the oscillating properties of the Bessel $J_0(x)$ function. At lower frequencies, the loss in the neck is relatively small, consequently the curves are diminishing from the center to the boundary of the cylinder. When the frequency gets higher, the first local minimum, which is defined as the spot size following the 0.38λ spatial resolution, drops from 3 cm, nearly half the neck radius to less than 0.5 cm. On the other side, the energy in the tail is soaring as the loss starts to increase with the frequency. At approximately 3 GHz, the peak energy in the tail surpasses the hot spot in the center, which indicates the disappearance of the spatial focusing.

The ratio of spot size to cylinder radius r_{spot} / r_{cyl}, the spot energy to the total energy inside the cylinder E_{spot} / E_{cyl}, and the peak energy to the source point energy U_{peak} / U_s over frequency are shown in Figure 4-18.

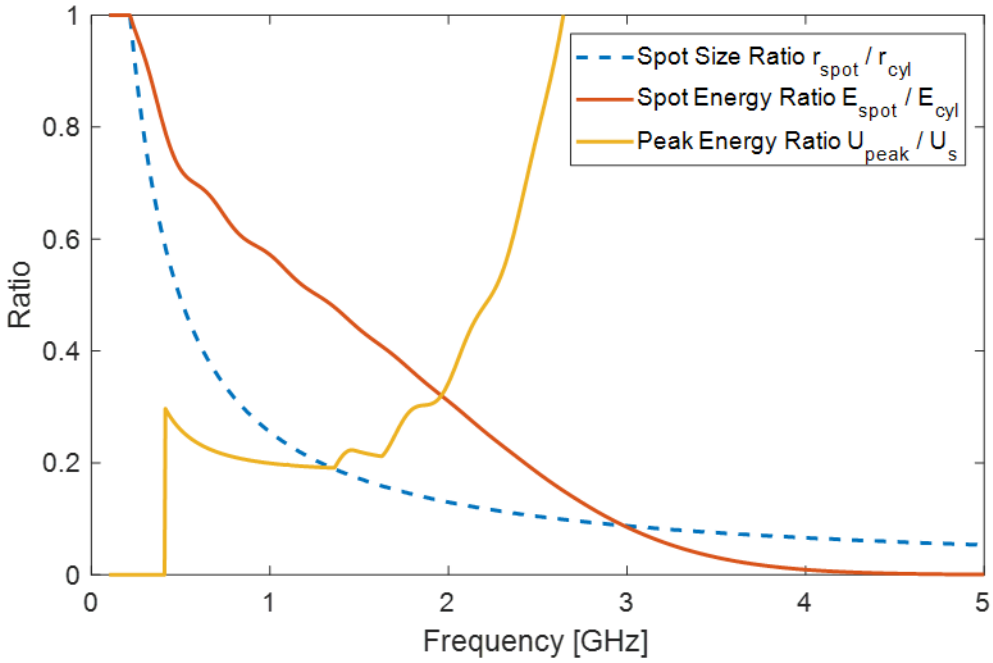

Figure 4-18 Spot size and energy ratio constraints as a function of frequency

With these three curves from the asymptotic study, the choice of frequency now turns into a constrained optimization problem. The spot size is monotonically decreasing,

hence we want to choose the largest possible frequency that satisfies the energy constraints to minimize the spot size. The spot energy ratio drops very quickly as the energy in the tail grows rapidly with frequency. The peak energy ratio starts from zero at first because there is no secondary peak in the cylinder area. Then it goes up and down before a completely shoot up at around 2 GHz which outruns the desired hot spot.

An example for the constrained optimization is shown in Figure 4-19. The spot energy ratio threshold θ_{sp} is set to be larger 50%, while peak energy ratio should be smaller than θ_p = 25%.

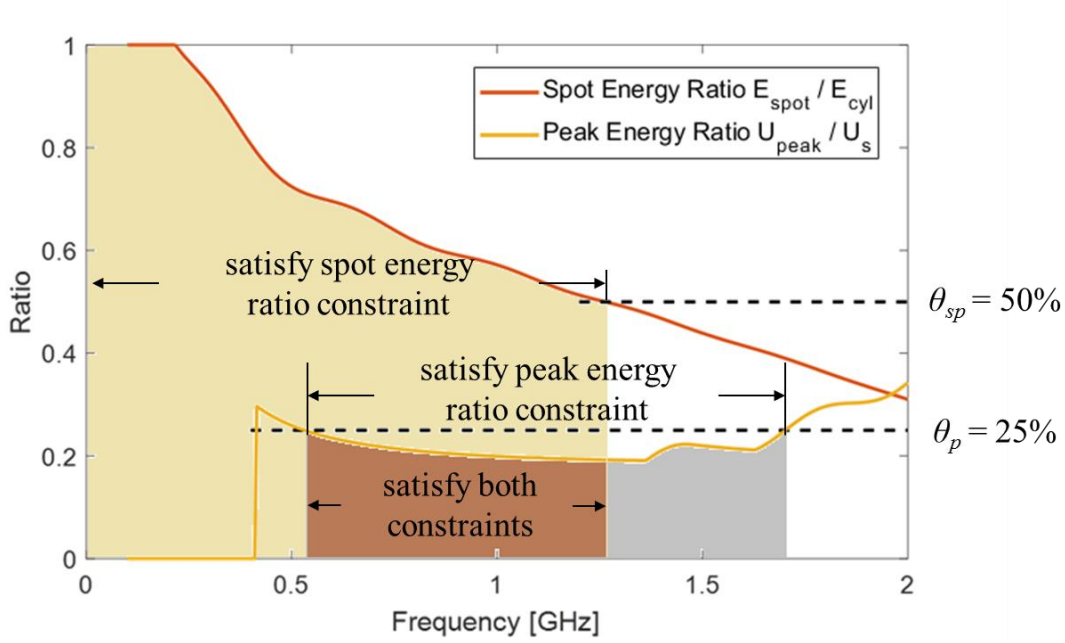

Figure 4-19 Optimizing frequency under energy constraints

The shaded area on the left colored in light brown shows a range of frequencies that satisfy the spot energy ratio greater than 50%, additionally the frequencies in grey area on the right comply with the peak energy ratio below 25%. Thus the brown area in the center highlighted the solution, which meets the requirements of both energy constraints. Furthermore, the constrained optimization should be completed by choose the optimized

frequency at the upper boundary of the solution to reduce the hot spot size. Thereby the optimized frequency is picked at 1.26 GHz.

After the optimized frequency is locked, it sets up a standard explaining the best scenario that TR could behave with a single frequency. Now it's time to step into the time domain, shape the spectrum of a time domain signal, and compare it with the standard to see if a broadband signal can achieve better results.

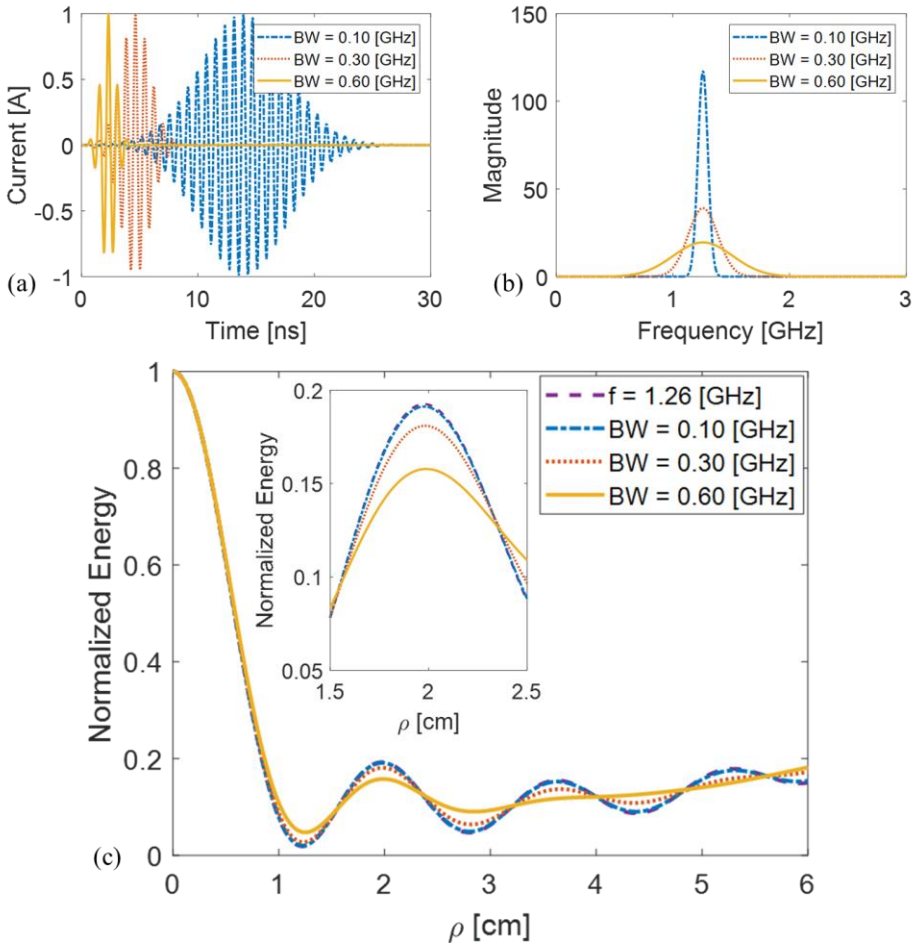

Figure 4-20 Normalized energy distribution of different bandwidths: (a) Gaussian pulses in the time domain; (b) spectrums of Gaussian pulses; (c) normalized energy distribution

To start with, we will keep the shape of the original signal a Gaussian pulse since it has a simple closed form Fourier transform. The carrier frequency of the pulse is reserved

at the optimized frequency 1.26 GHz. The 3dB bandwidth of the spectrum is considered as a variable. The asymptotic energy is hereby calculated for three different bandwidths as shown in Figure 4-20. The studied signals has 3dB bandwidths of 0.1 GHz, 0.3 GHz and 0.6 GHz, corresponding to 28 ns, 9 ns, and 5 ns Gaussian pulse width in the time domain respectively. While the bandwidth is small, the normalized energy distributions are almost identical to the single frequency one. As the bandwidth grows larger, it is observed that the peak energy outside the hot spot becomes smaller, shaping the energy distribution outside the cylinder smoother.

Similarly, to get the energy ratio constraints for further optimization, the spot size ratio, the spot energy ratio and the peak energy ratio are shown in Figure 4-21.

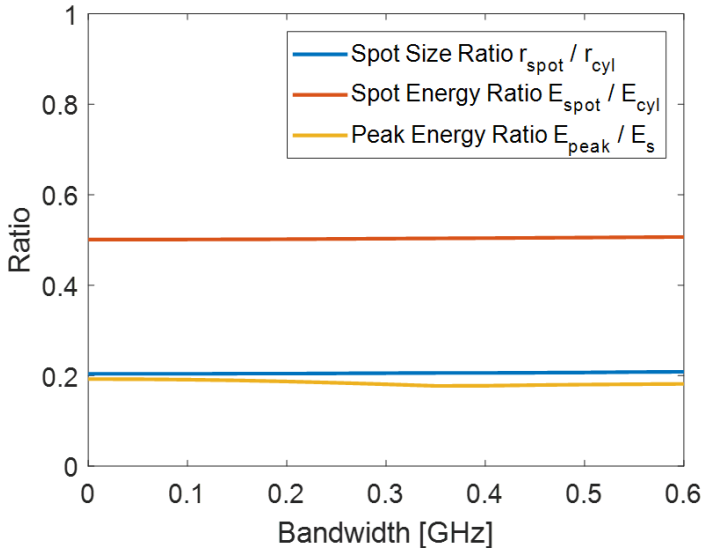

Figure 4-21 Spot size and energy ratio constraints as a function of bandwidth

Unfortunately, increasing the bandwidth does not effectively influence the spot size or spot energy ratio. Nevertheless, it is able to slightly lower the peak energy ratio, which could be useful in the removal of the spurious spots. It is safe to conclude that the broadband Gaussian pulse signal does not have a better performance than a single

frequency signal. However, there exist other time domain signal types, which are able to accomplish a better spatial focusing under the same energy constraints. For example, a spectrum with damping amplitudes at higher frequencies would improve the focusing by compensating the rising energy in the tail.

4.5.2d Approaching the Spatial Focusing Limit

The asymptotic study is based on the existence of a close TRC. However, it is not practical to build a continuous boundary using infinite number of antennas. Therefore a finite number of antennas is placed in-phase at the same radius to simulate the closed cavity configuration. The energy distribution profile is then developed following the steps in Figure 4-13. It is also a good way to evaluate how number of antennas will affect the spatial focusing profile by comparing it to the asymptotic study results.

First of all, the spatial focusing profile from a two-channel system is measured. It is the simplest TR system with the one source and the other TRM respectively put inside and outside of the cylinder. The original signal is a Gaussian pulse at the optimized frequency 1.26 GHz, with a 3dB bandwidth of 0.1 GHz. The spatial focusing after the TR process is illustrated in Figure 4-22.

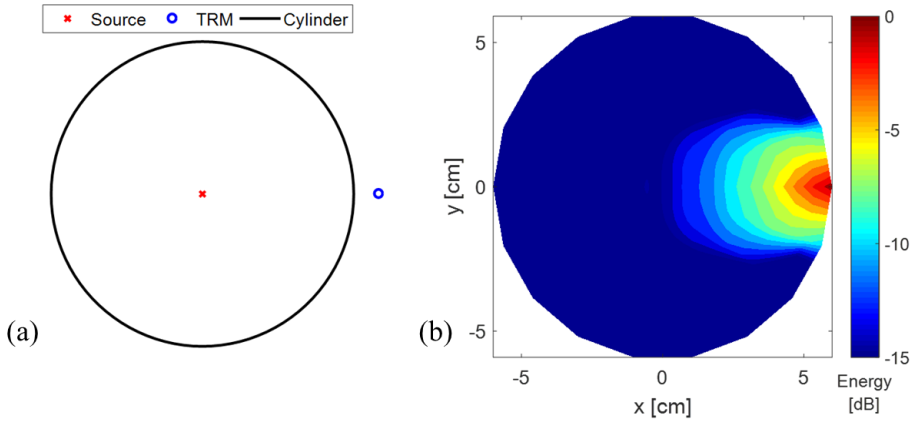

Figure 4-22 Spatial focusing from a single TRM: (a) schematic drawing of the source-TRM configuration; (b) energy distribution result

The energy is stronger on the side closer to the TRM. It is recognized that there is no hot spot at the center, meaning no spatial focusing is seen from a two-channel system in the neck model. The reason is that in a highly symmetric, homogenous, non-reverberating system, the information in the sona signal from a single antenna is not enough to record the source location.

The number of antennas *n* is increased to gather more information from the environment. The original signal is kept as a Gaussian pulse at the optimized frequency 1.26 GHz, with a 3dB bandwidth of 100 MHz. The spatial focusing from multiple TRMs are shown in Figure 4-23.

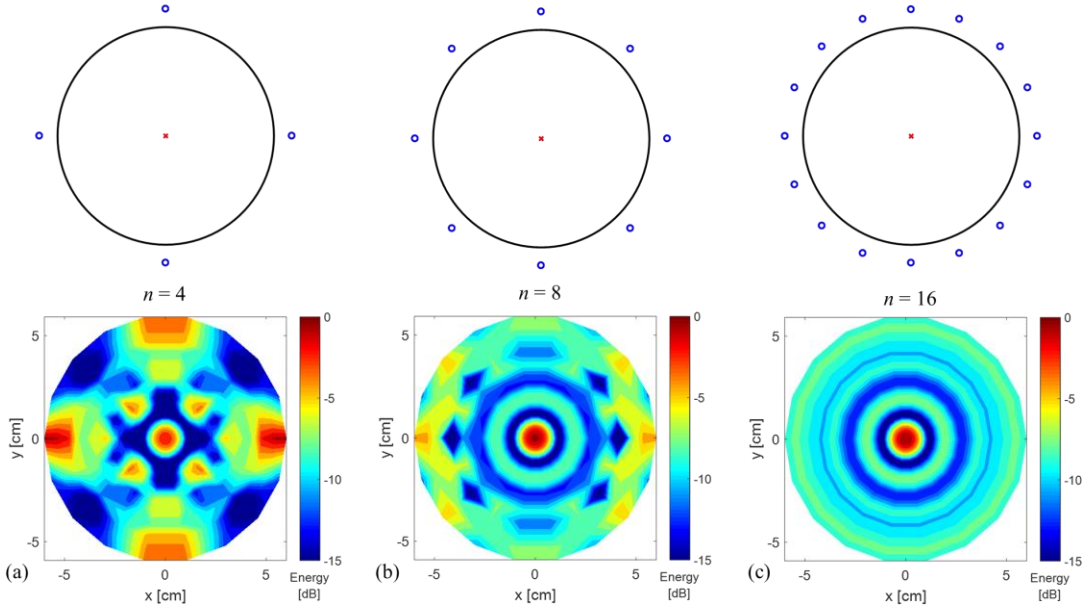

Figure 4-23 Spatial focusing profile from *n* TRMs: (a) n = 4; (b) n = 8; (c) n = 16; the figure above shows the source-TRM configurations

At *n* = 4, the hot spot at the source location is recognized, whereas the magnitude gets even higher at the position close to the TRMs. When the number of antennas is doubled to eight, the spatial focusing profile shows a more distinguished spot at the center, with the energy far greater than the spurious spots near the TRMs. With the configuration of 16

TRMs, the undesired hot spots on the boundary are completely removed. The energy distribution is following the oscillating while delaying trend of the Bessel function, approaching the spatial focusing limit. To further study the effects of the number of antennas, the normalized energy over the cylinder radius on *x*-axis is shown in Figure 4-24.

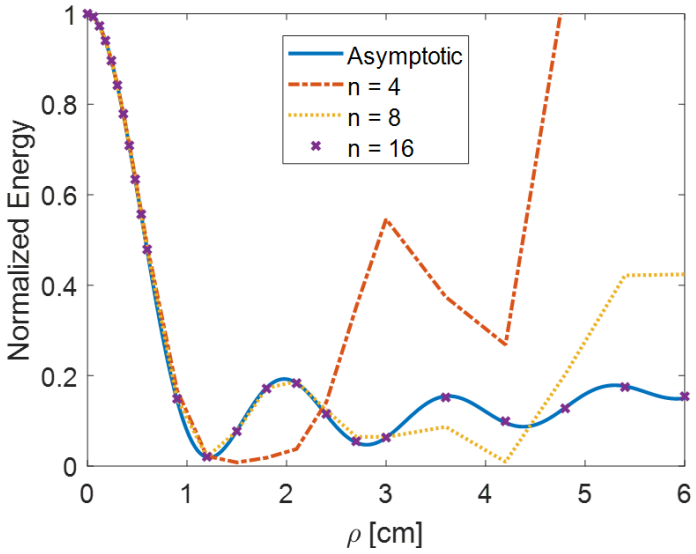

Figure 4-24 Approaching the spatial focusing limit by increasing number of antennas

All three curves behave quite similar to the theoretical one at the range close to the center. The spot size, defined by the first local minimum, are given approximately the same value from them. The energy distribution starts to diverge for 4 and 8 antennas when approaching the boundary of the cylinder. The result from 16 antennas matches the asymptotic result pretty well, illustrating that by increase the number of antennas, the spatial focusing profile is approaching the limit from the asymptotic study. We could choose $n = 16$ as a good approximation to the theoretical results.

4.5.3 Focusing at an Arbitrary Location

When the original source is placed at an arbitrary location inside the 2D cylinder surrounded by a closed time-reversal cavity, the Green's function could be found in a 2D Helmholtz equation

$$\nabla^2 G(\mathbf{r},\mathbf{r}') + k^2 G(\mathbf{r},\mathbf{r}') = -\delta(\mathbf{r}-\mathbf{r}'), \tag{4.41}$$

where **r** is the observation point, **r**' is the source point. *k* denotes the wavenumber inside the cylinder, δ is the Dirac delta function.

The solution of (4.41) is a summation of higher order Bessel functions. It is not easy to study the asymptotic energy distribution as elucidated for the center focusing case. However, we could use multiple antennas to approach the theoretical results.

To start with, keeping the problem in the frequency domain, the reconstructed signal over space at a single frequency is obtained following Figure 4-25.

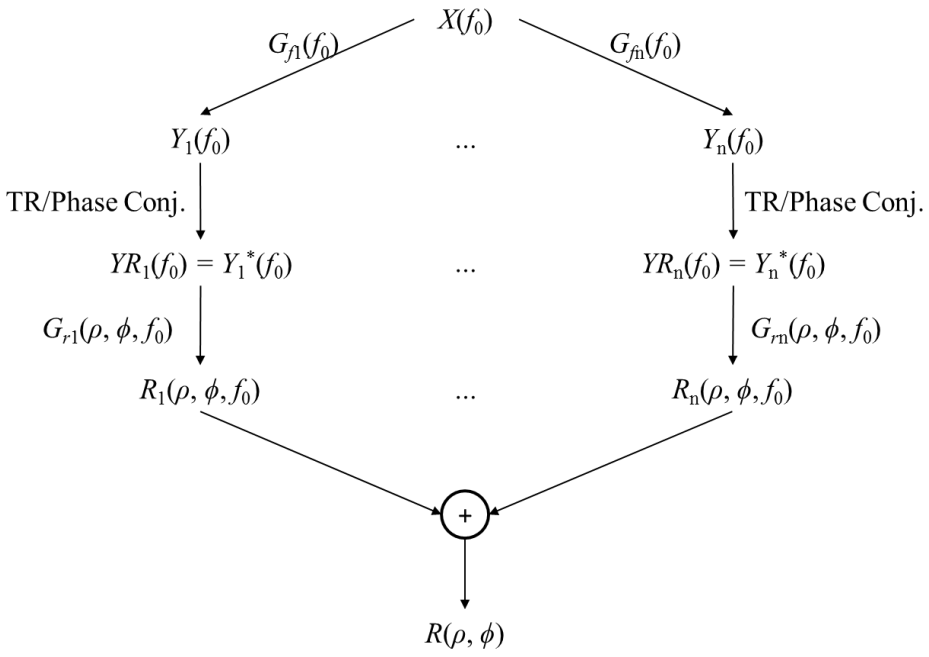

Figure 4-25 Flow chart of solving the frequency domain reconstructed signal over space from multiple antennas by phase conjugation

The procedure is similar to getting a reconstructed signal in the time domain shown in Figure 4-13, except that the phase conjugation is applied on the sona which is equivalent to a TR operator as for the electric field. The source is placed half way between the center and boundary of the cylinder on *x*-axis with the frequency set at 1.26 GHz. The spatial focusing profile is shown in Figure 4-26 after the TR process by 16 TRMs.

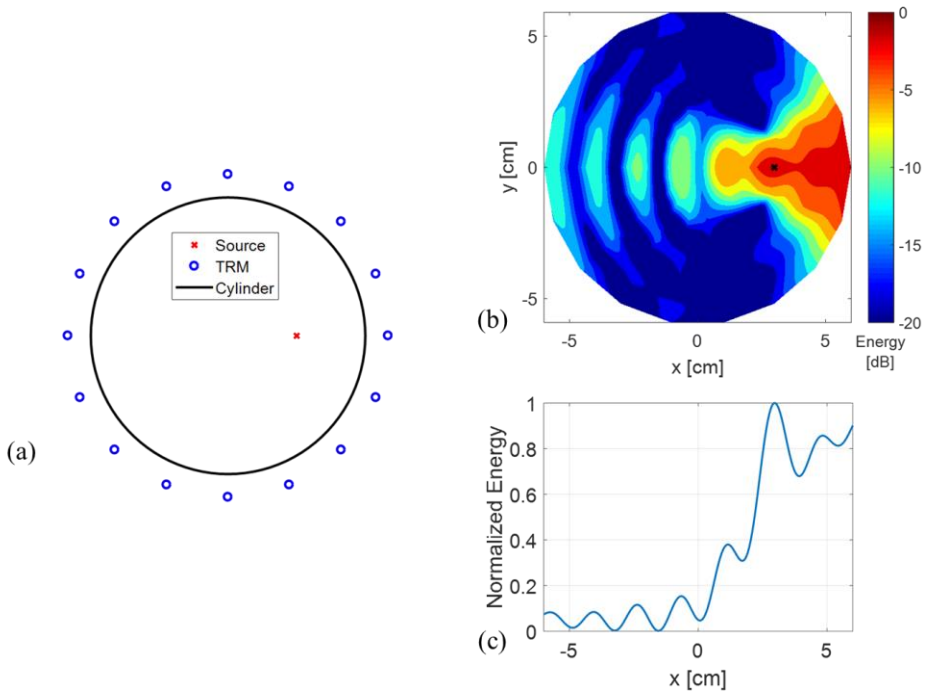

Figure 4-26 Focusing at an arbitrary location: (a) source-TRM configuration; (b) energy distribution in the cylinder; (c) normalized energy on *x*-axis

Spatial focusing is spotted at the source location, but the energy near the boundary is comparable to the focal point, with the peak power ratio as high as 0.9 on the *x*-axis. Due to the lack of selectivity, it is not applicable in the biomedical use by assigning the magnitude and phase directly from the Green's function for each element. Therefore the improvement on the selectivity from EM TR is required.

From the antenna design point of view, in a phased array, the phase of each element governs the beam direction, i.e., the where the most EM energy would propagate, and the

magnitude of them determines the shape of the beam, in other word, the weighting factor of energy in each direction [106]. Likewise, in the TR process, the phase information from forward Green's function has encoded the focusing location, while the magnitude will be shaping the spot. So the magnitude correction on the sona signal needs to be done to enhance discriminating focusing.

Intuitively thinking, there are two ways to carry out the magnitude correction: one is to set all the TRMs as having equal magnitude, since the equal magnitude configuration in the phased array gives the narrowest beam. The other method is to assign the magnitude of each element the value that is reciprocal to the magnitude from the Green's function. Since the antenna closer to the source receives stronger signals, it compensates the loss during the propagation by setting reciprocally the magnitude, thus allowing each antenna to make equal contribution to the reconstruction. The spatial focusing profile and normalized energy on *x*-axis after magnitude correction is shown in Figure 4-27.

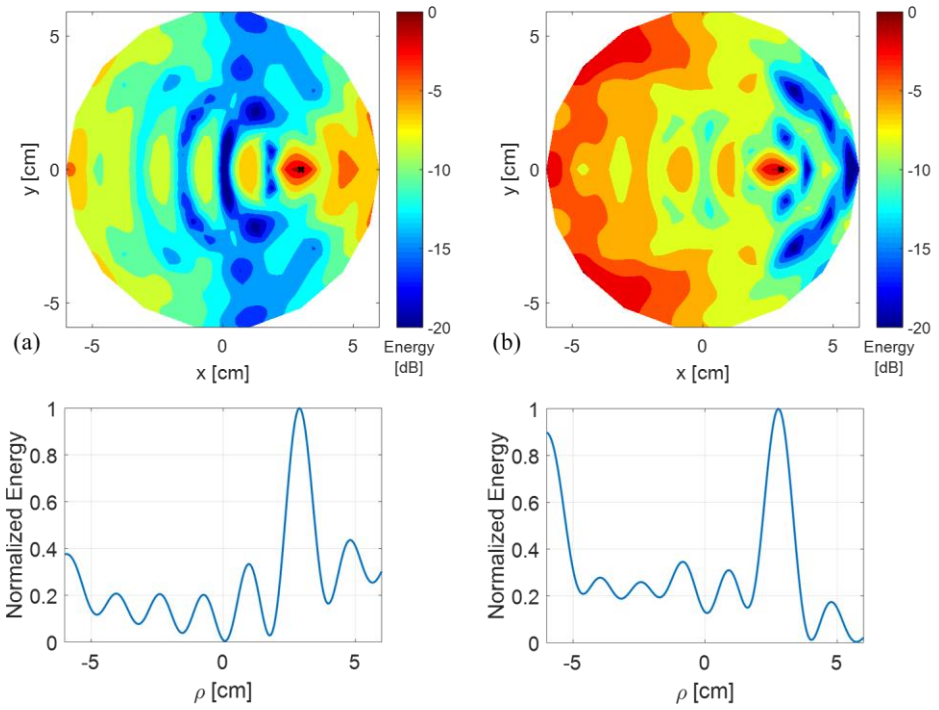

Figure 4-27 The energy distribution after magnitude correction: (a) equal magnitude; (b) magnitude reciprocal to Green's function. The plots below show the normalized energy on *x*-axis

It is generalized that the correction is done by adding a correction factor p in the power of the magnitude from the Green's function, which is described by

$$Y_R^{corr} = \left|Y_R\right|^p \cdot e^{j\angle Y_R}, \tag{4.42}$$

where Y_R is the time-reversed sona in the frequency domain and Y_R^{corr} is the signal after correction. If $p = 1$, no correction is done, the magnitude of the signal maintains what is gets from the Green's function; $p = 0$, the magnitude of each element is changed equally to 1; $p = -1$, the magnitude is set to be its reciprocal.

The peak energy ratio and the spot energy ratio are plotted in Figure 4-28 *versus* the correction factor p.

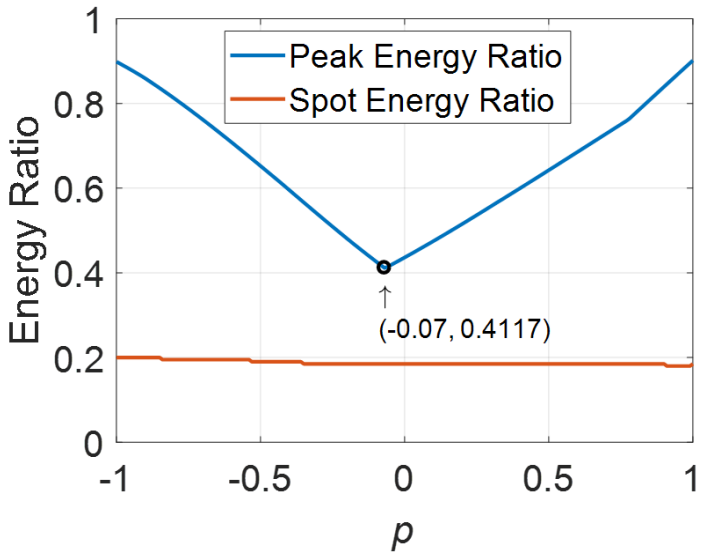

Figure 4-28 Peak energy ratio as a function of correction factor *p*

The peak power ratio reaches its minimum at approximately $p = 0$, which follows our observation from Figure 4-26 and Figure 4-27. There is a hot spot comparable to the center spot on either left or right side of the cylinder in p = 1 or p = −1 case, which makes the peak energy ratio the highest on each side. It also correlates with the antenna theory that the equal magnitude in each element would accomplish the best focusing. In this particular scenario in the neck model, the selectivity of focusing could be best enhanced by choose the correction factor p equal to −0.07. The spot energy ratio remains constant as p changes.

Chapter 5 Focusing with TR

5.1 Non-invasive Focusing Methods

In cancer therapies, we are facing a much more complicated inhomogeneous media, including both cancer and healthy tissues. According to the above discussed TR process, an EM source is required to be placed at a tumor site so as to generate waveform. It then leads to rather complex waveforms received by each of an array of antennas surrounding the body due to interactions with intervening tissues. However, such internal source could be deposited through an invasive surgery, which is costly and risky in the treatment. In order to apply TR non-invasively, it is necessary to develop methods other than open surgeries to spatially encode the target location.

One intuitive approach is to incorporate the computer-based simulations in clinical therapies [36]. For each patient, a personalized permittivity map over the lesions is established based on the existing biomedical models, such as Virtual Population (ViP) by It'Is Foundation [107], in combination with the individual computed tomography (CT) and magnetic resonance imaging (MRI)data. The permittivity map enables the full-wave EM simulation on complex during the treatment, the results of which can be utilized to manipulate the signals of the antennas in clinical therapies.

The detailed process of performing TR with a permittivity map is the following: First, the customized permittivity map is generated as shown in Figure 5-1(a). In the map there exists the cancer tissue where our heating aims at, along with the healthy tissues where the heating should be avoided. The forward step in the TR process is completed in the simulation by putting an active source, usually modelled as an electric dipole, at the tumor location. The sona signal is received by the antennas located outside the human body

acting as TRMs after the source signal travelling through the complex media as shown in Figure 5-1(b). The recorded sona signal is then time-reversed, amplified and transmitted from the real antennas in the phased array of a clinical hyperthermia system. From the time invariance property of the Maxwell's equation, the selective heating is delivered to where the active source is located.

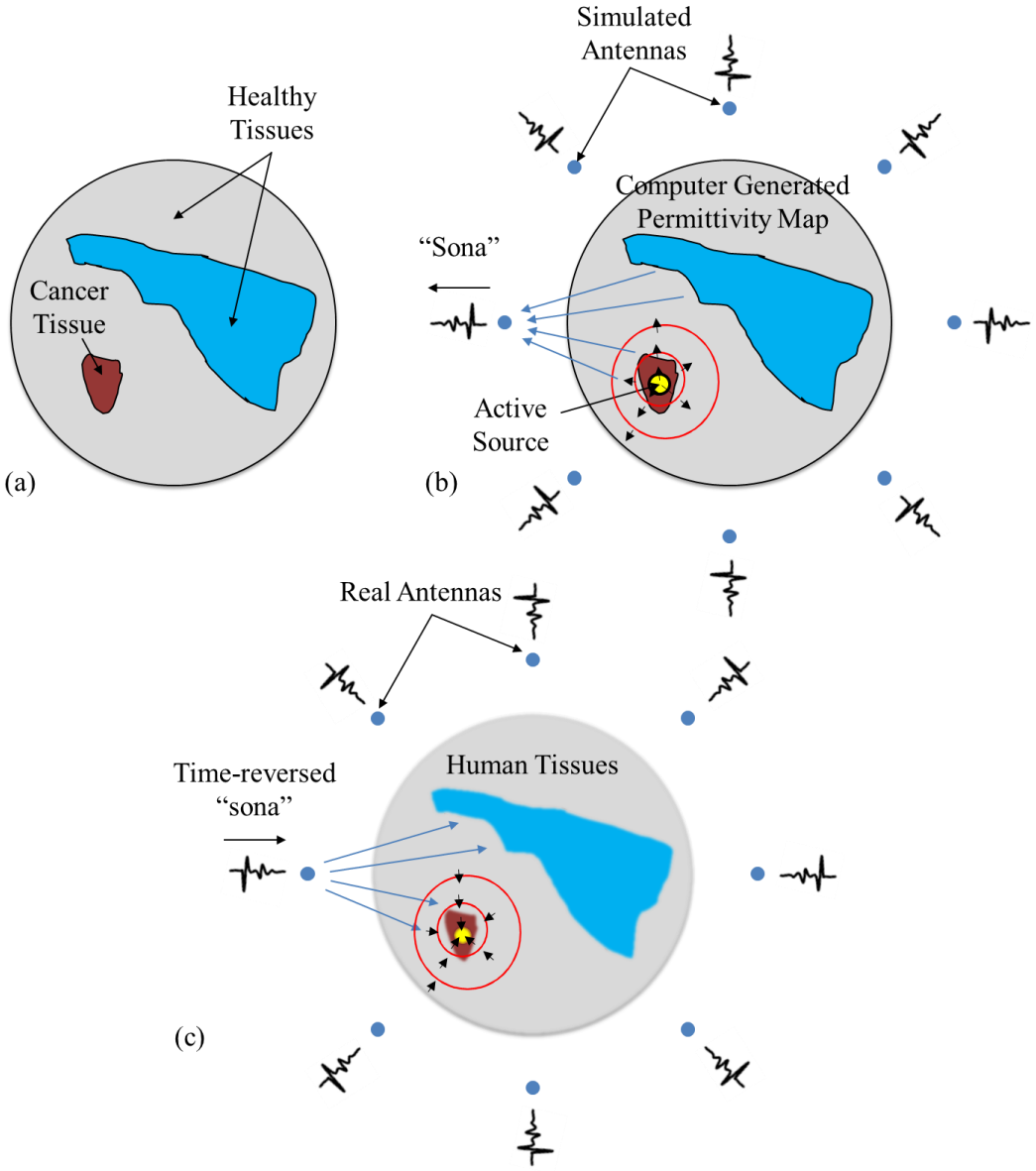

Figure 5-1 Focusing with an internal source: (a) generated permittivity map; (b) time-forward step; (c) time-reverse step

However, the placement of internal source is essential in the simulation process. It is preferable if a "beacon" is exploited to spatially encode the target location. If a passive nonlinear element is planted at the tumor site in a linear system, then the new frequency components in the system is only produced by the nonlinear element [108]. So the sona that contains the additional frequencies has encrypted the location of the nonlinear element. In this way the tumor is successfully marked by a nonlinear beacon. The nonlinear beacon method for TR has been discussed in subwavelength position sensing [109] and damage detection in solids [110].

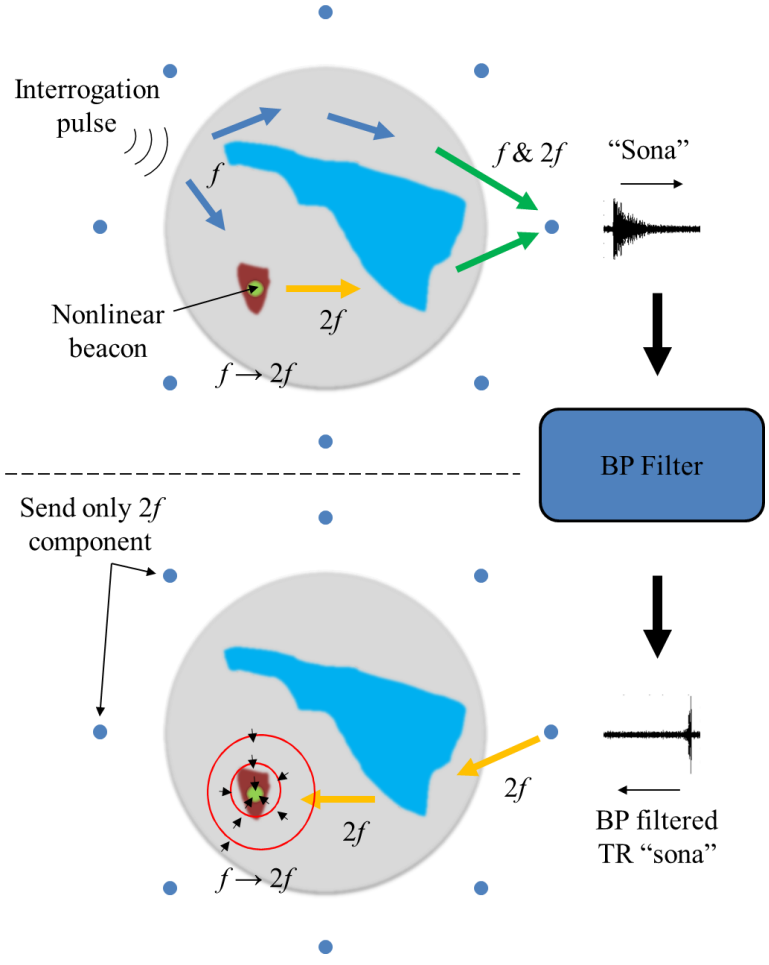

Figure 5-2 Focusing with a nonlinear beacon

The process of nonlinear TR heating in the human tissues is shown in Figure 5-2. At first, a passive nonlinear beacon, which has the property of doubling the original frequency, is implanted in the cancer tissue to tag the tumor site. After that an external interrogation signal, such as a Gaussian-modulated pulse at the carrier frequency f, is transmitted towards the lesion. When the EM waves go through the nonlinear beacon, the new frequency component is generated at twice the carrier frequency $2f$. Afterwards, the sona signal, including both f and $2f$ components, is received at the surrounding TRMs. After passing it through a band-pass filter, the filtered sona now has only the doubled frequency. Since there is no other nonlinearity in the tissue, it can be considered as the filtered sona is generated from the nonlinear beacon, which acts exactly the same as an internal active source. The focusing should be seen at where the nonlinear beacon locates, if the time-reversed BP filtered sona that has only the $2f$ part is used during the reconstruction. Hong *et al.* develops a way to isolate the $2f$ sona using pulse inversion for EM waves [111]. This offers us a new way to focus non-invasively with no internal, only external sources needed.

5.2 Reverberating Environment

Ideally a closed time-reversal cavity (TRC) should be built in order to confine all the EM energy for better focusing quality. This would require a multi-antenna system. However, when the system is enclosed in environment with highly reflecting and scattering boundaries, it is considered to be equally effective. Such reverberating cavity could reduce the time and meshing complexity in the simulation process. Hence a ray-chaotic metallic box [112], usually called 3D Gigabox, is introduced as a start for the assessment of the TR focusing properties.

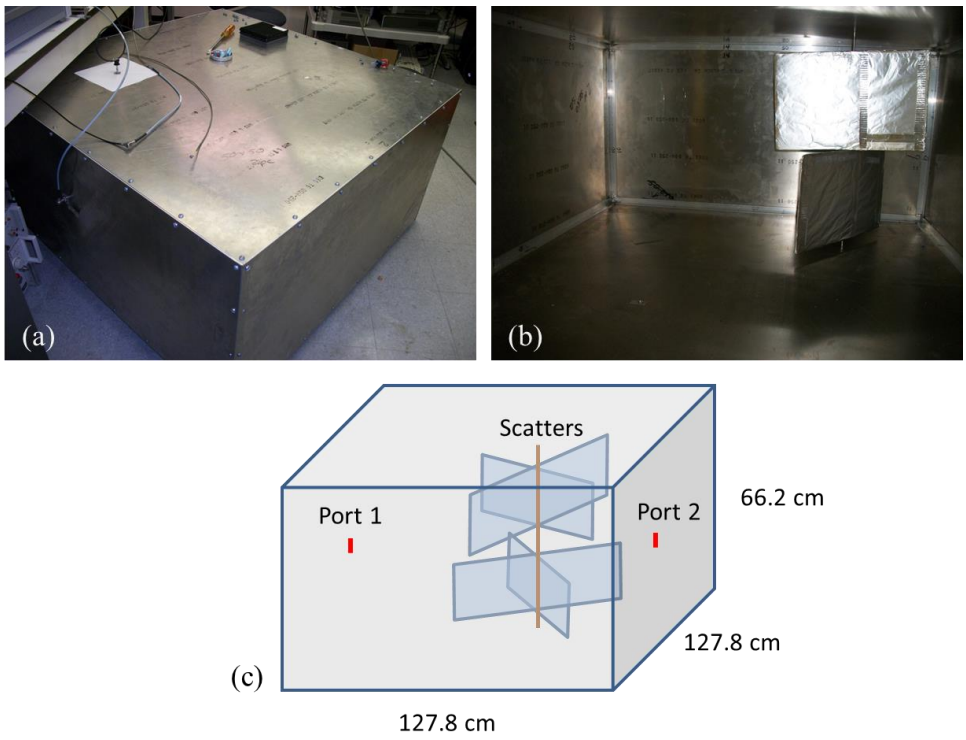

Figure 5-3 3D Gigabox with strong reverberating: (a) overview; (b) scatters inside the box; (c) schematic drawing with dimensions

The exterior dimension of the Gigabox is shown in Figure 5-3(c). Inside the box there are two scatters stirring the modes to create a reverberating environment. The walls and scatters of the box is made from high conductive metals with good reflection to EM waves. There are two antennas are located on the adjacent walls of the enclosure. When TR is performed, one antenna is used to transmit the source signal, whereas the other one functions as a TRM.

5.2.1 Focusing with Active Internal Sources

The Gigabox was drawn and imported into CST MICROWAVE STUDIO® as shown in Figure 5-4 so as to perform full-wave simulation of the TR process in a two-channel reverberating system. The transient solver, which is Finite Integration Technique

(FIT) based, is used in the following simulations to compare the reconstructed signal to the original source in the time domain.

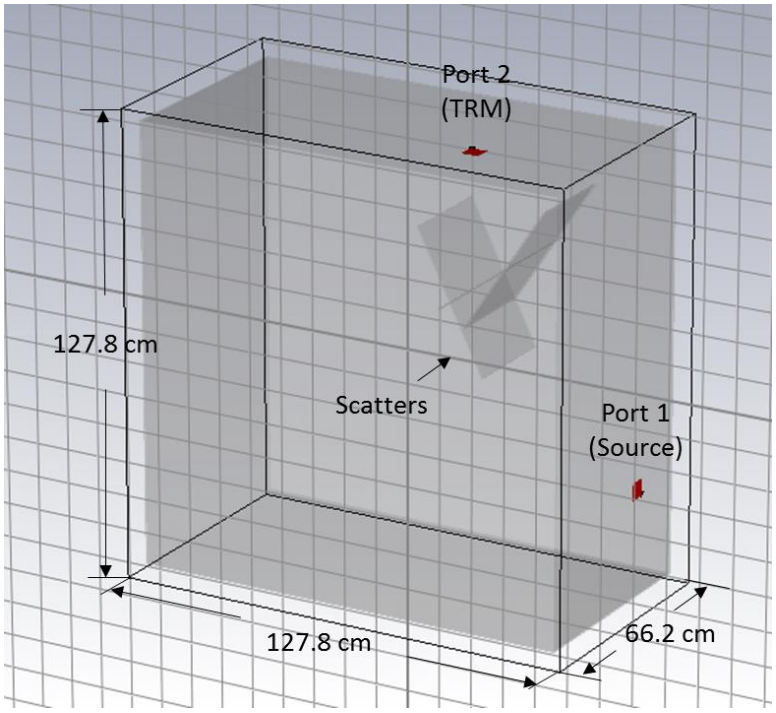

Figure 5-4 3D Gigabox in CST MICROWAVE STUDIO®

The enclosure and the scatters have a thickness of 3 mm, and are treated as perfect electric conductors (PEC) in the simulation. The box is air-filled. Port 1 and 2 are modelled as discrete ports with characteristic impedance of 50 ohms.

Figure 5-5 shows the simulation process of focusing with an active internal source. In the time-forward step, the original source signal, a 70 ns width Gaussian-modulated sinusoidal pulse, with carrier frequency of 2.4 GHz and 3dB bandwidth of 400 MHz, is transmitted from Port 1. The sona signal is recorded at Port 2. Changing the role of the antennas, the time-reversed sona is then sent from Port 2 after a 20dB amplification in the time-reverse step. The original discrete port is replaced by a voltage monitor to check the temporal reconstruction. Additionally, a 20 cm by 20 cm 2D field monitor is centered at

the Port 1 to investigate the spatial focusing. The time domain signals during the reconstruction are also shown in Figure 5-5.

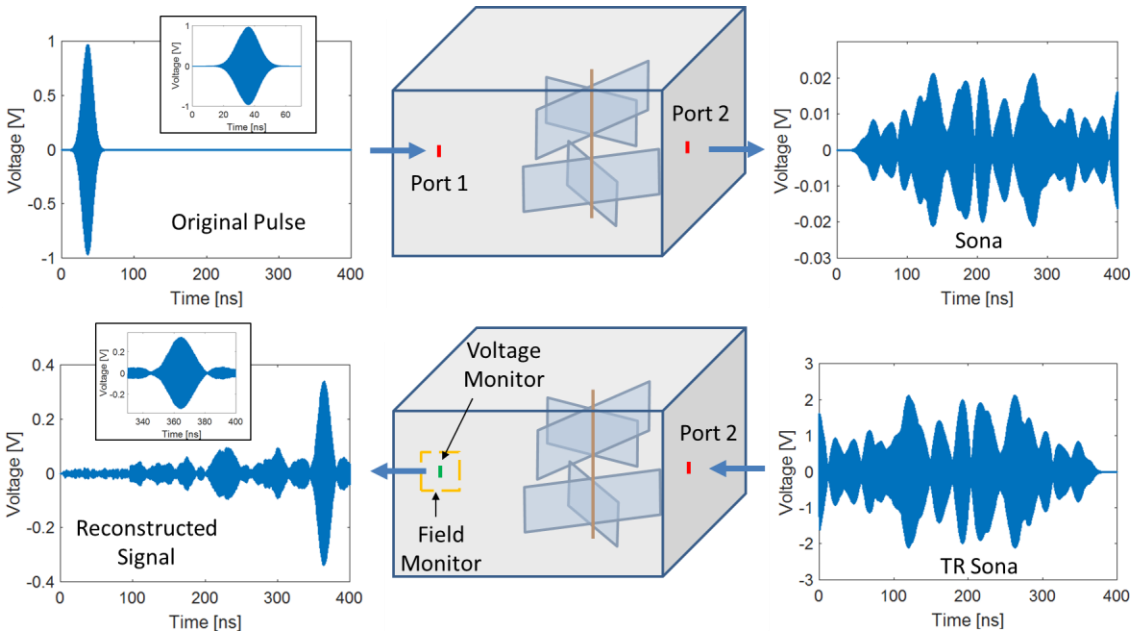

Figure 5-5 TR process of focusing with an internal active source

The maximum of the reconstruction is spotted at t = 364.3 ns, with a peak-to-peak voltage of 0.68 V. The power to noise ratio (P/N) is defined as the peak-to-peak voltage ratio of the reconstructed pulse to the largest noise pulse outside the reconstruction. In this particular configuration, the P/N is approximately 11.5 dB. It is considered as a good reconstruction of the original signal. Furthermore, the reconstructed signal is time-reversed and enlarged at the range where the original signal has non-zero values in Figure 5-6(a)(b). It is seen that the reconstructed signal has the same Gaussian modulated shape and the same width compared with the original signal. The normalized cross-correlation is also calculated between the two signals to quantify the temporal focusing as shown in Figure 5-6(c). The maximum occurs at τ = 0, which means the reconstructed signal largely resembles the original signal. The temporal focusing property of TR is hence proved.

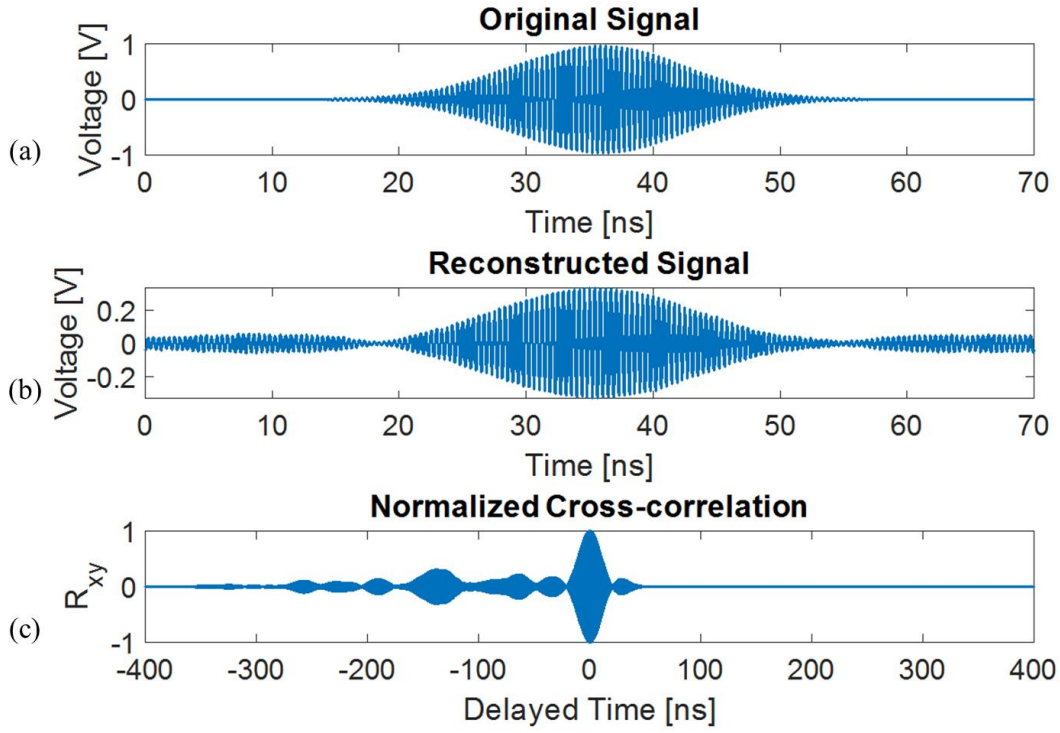

Figure 5-6 Temporal focusing analysis of the linear TR in the reverberating cavity: (a) the original signal; (b) the time-reversed reconstructed signal; (c) the normalized cross-correlation

The normalized energy distribution calculated from $|E|^2$ at the time point where the sona tops its value is shown in Figure 5-7. The highest energy which shows the spatial focusing from TR is clearly seen at the center of the field monitor, exactly where the original source locates. The half power (3 dB) focal spot size is about 4.6 cm by 4.6 cm. In the area of observation, the spurious spots are also found, but the amplitude of them is no larger than half of the amplitude in the center. It is concluded that the TR has the ability to focus selectively over the space, which is beneficial in the modern cancer therapy.

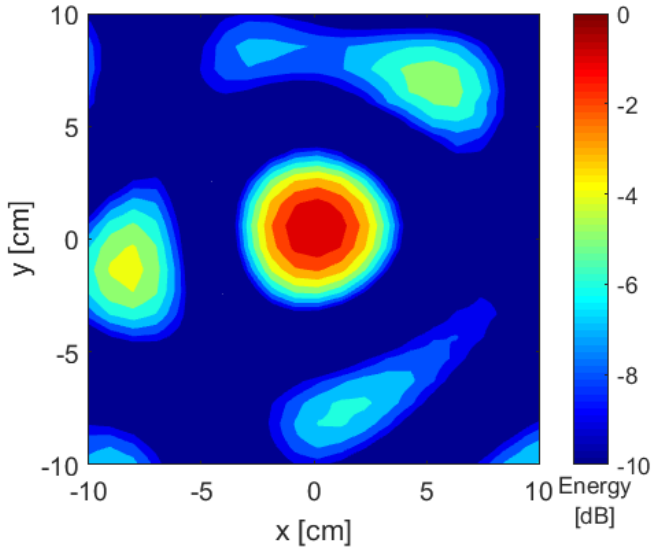

Figure 5-7 Spatial focusing analysis of the linear TR

The focusing property of TR should persist even with the presence of loss due to the time-reversal symmetry of the Maxwell's equations. To study the focusing quality from TR in a lossy and inhomogeneous environment, the material of the enclosure and the scatters are changed from PEC to copper with conductivity 5.8×10^7 S/m, followed by a 10 cm × 10 cm × 10 cm cube of tap water, which has relative permittivity of 78 and conductivity of 1.59 S/m, placed on the ground plane 20 cm away from the scatters along the *x*-axis inside the box as a perturbation to the system. The reconstruction results are shown in Figure 5-8. The same 2.4 GHz Gaussian-modulated pulse is transmitted from Port 1. The sona signal has a decaying trend in its envelope shape due to the loss in the environment. The amplitude of the sona is about 100 times weaker than the lossless case. Despite the low power, the reconstruction signal shows a similar Gaussian shape as to the original signal, with a peak-to-peak voltage of 0.0186 V. Compared to the lossless environment, the P/N is slightly better at about 12.9 dB, which indicates that the focusing is enhance from the information provided by the loss and inhomogeneity. The inset is the

E-field distribution at the peak voltage time point t = 364.6 ns in the field monitor region, a 60 cm long, 10 cm wide rectangular, showing a half power focal area of 8 cm by 8 cm. The field through the center line is plotted *versus* distance along the x-axis as shown in Figure 5-9. It follows the shape of a sinc(x) function.

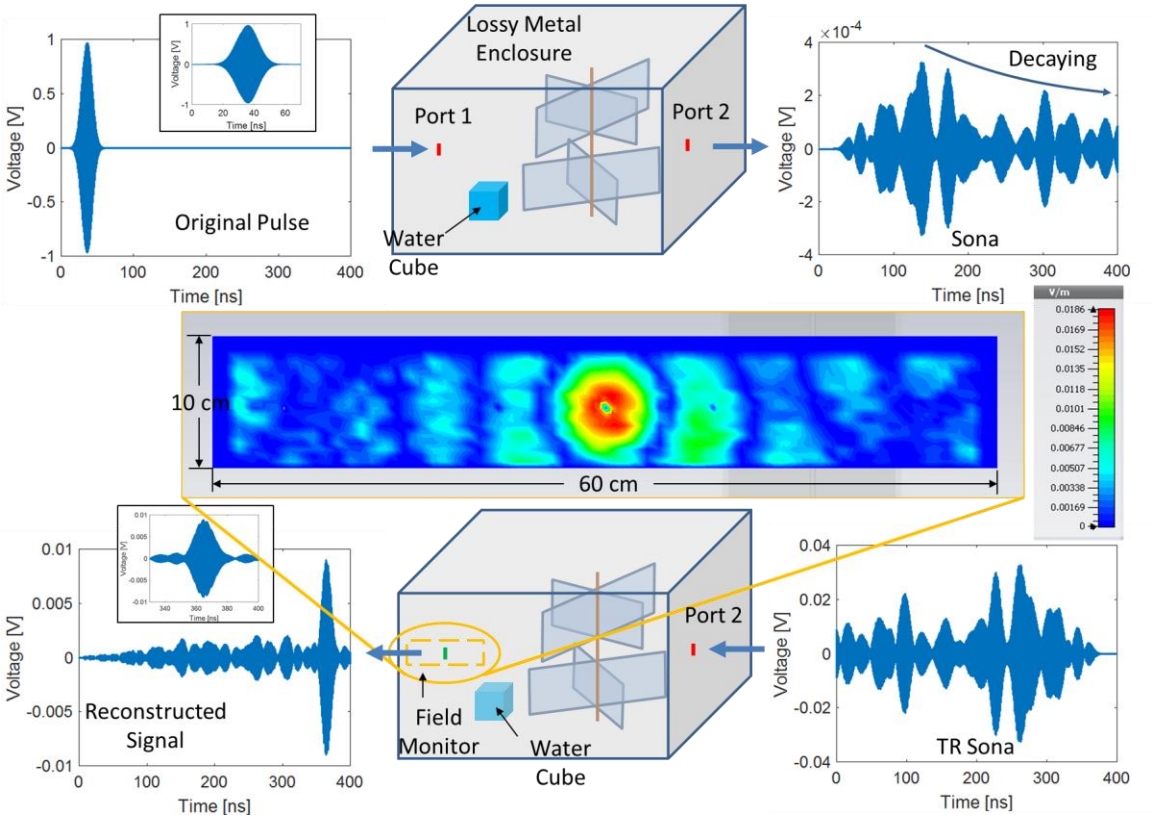

Figure 5-8 TR process in a lossy and inhomogeneous environment

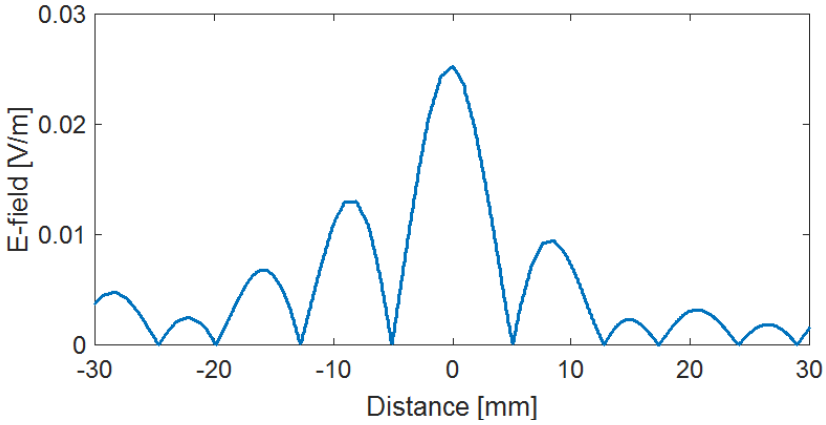

Figure 5-9 Spatial profile of TR focusing in a lossy environment

5.2.2 Focusing with Passive Nonlinear Beacons

The spatial encoding usage of passive nonlinear elements in a wave chaotic system has been described [111, 113]. It would be more beneficial to extend this method into a clinical system design. To further test the focusing property of TR with nonlinear beacons, a nonlinear port is added to the current 2-port linear system. In the simulation, the nonlinearity is introduced by connecting a rectifying circuit to the additional Port 3 as shown in Figure 5-10. An 18 ns broadband Gaussian pulse with carrier frequency 2.2 GHz first go through a 3dB power splitter. Half of the signal maintains its original form and frequency, entering the Gigabox from the linear Port 1 as the previous simulations. The other half goes into the system from the nonlinear Port 3 after passing through a rectifying circuit that generates the higher frequency. The circuit part is simulated in CST DESIGN STUDIO™, employing the S-parameters of the 3D Gigabox calculated from the simulations in CST MICROWAVE STUDIO®.

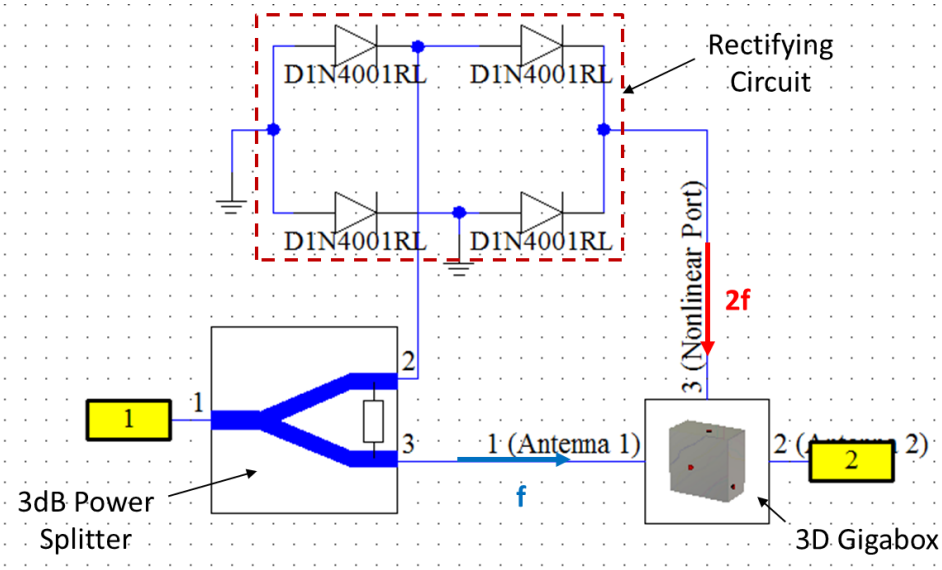

Figure 5-10 Schematic diagram of nonlinear TR simulations

The sona signal received at Port 2 contains both the original carrier frequency at 2.2 GHz and generated frequency at 4.4 GHz and higher as shown in Figure 5-11. Hence the nonlinear port can be considered as a beacon where the frequency components besides the original carrier frequency is generated.

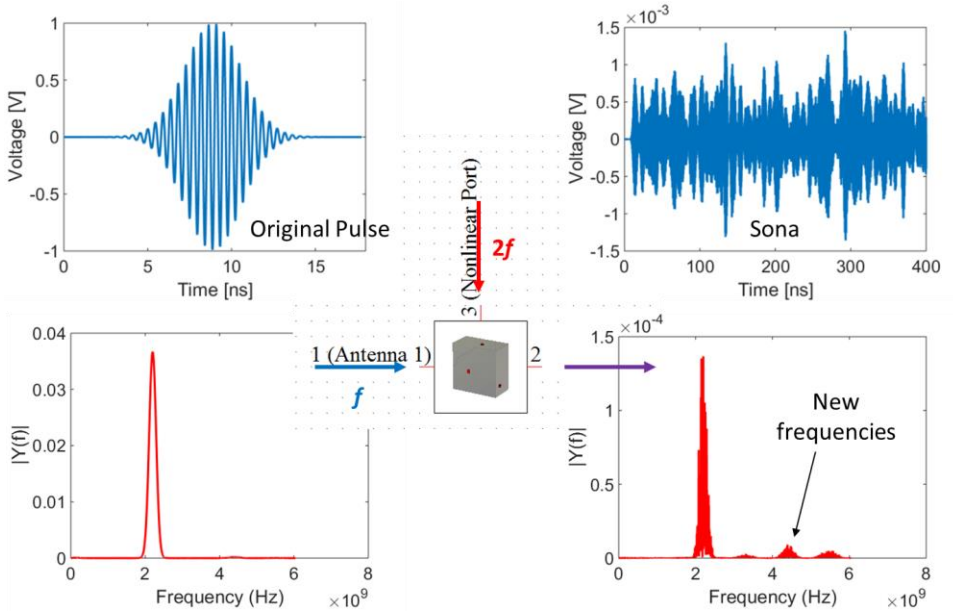

Figure 5-11 Time-forward step of the nonlinear TR

The next step is to pass the raw sona signal through a high-pass filter to get a filtered sona that keeps only the newly generated frequency components. The 9th order Butterworth high-pass filter is implemented with a MATLAB program and is considered ideal. The 2.2 GHz original carrier frequency is wiped out in the filtered sona, which is then transmitted back into the system from Port 2. These emitted new frequencies follows exactly the same way as that an active source is placed, which leads to a perfectly reconstructed signal at the nonlinear port after the TR process shown in Figure 5-12. The P/N of the reconstructed signal is about 10.9 dB. As expected, no focusing is seen at the original linear port.

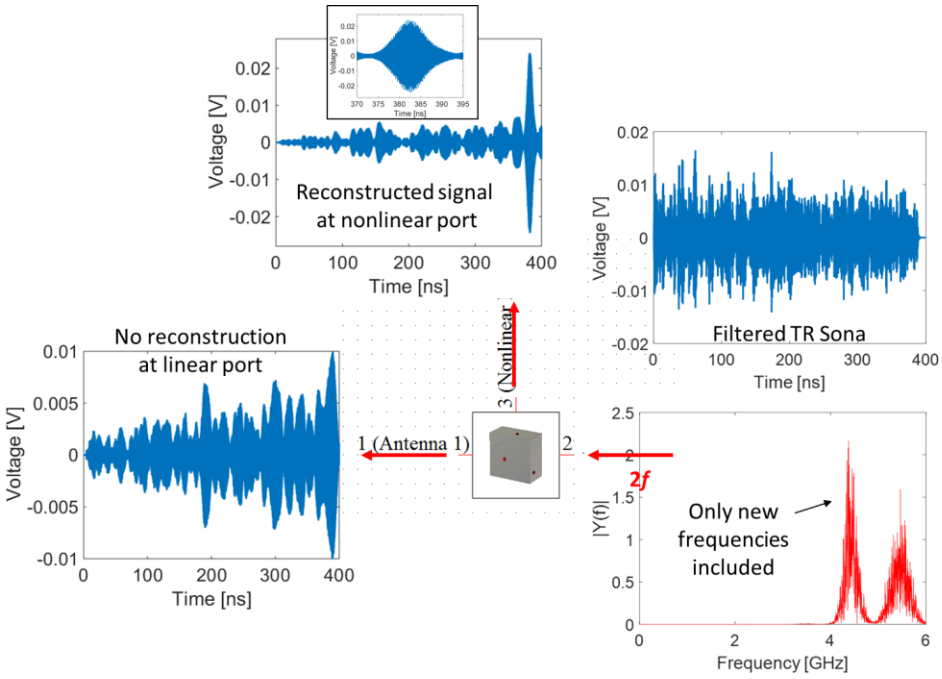

Figure 5-12 Temporal focusing analysis of the nonlinear TR

The spatial focusing is also observed as shown in Figure 5-13. The half power focal spot area is about 2.2 cm by 2.2 cm, which is highly reduced compared to the linear case because of the shorter wavelength. It is concluded that the passive nonlinear object can be successfully exploited as a beacon to spatially encode the target location.

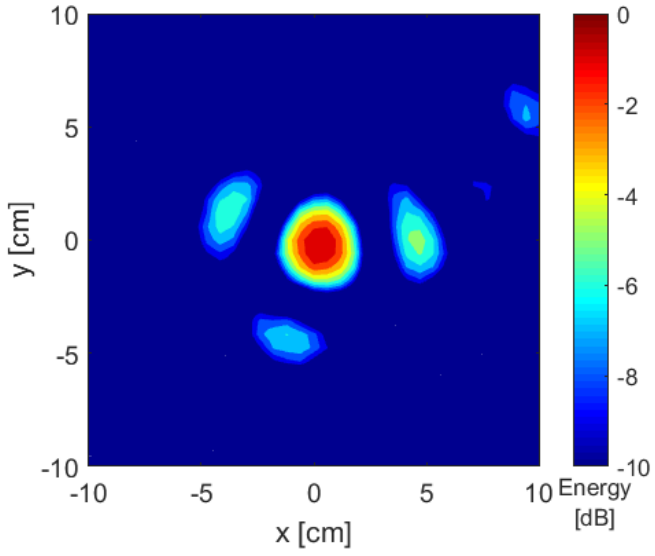

Figure 5-13 Spatial focusing analysis of the nonlinear TR

5.3 Ballistic Approach

After validating the temporal and spatial focusing properties of TR in a two-channel reverberating cavity, a more complex multi-antenna system with inhomogeneous media that simulates the human tissues should be considered next. Such system, often referred as the "ballistic" TR, utilizes the ballistic waves from each antenna without much scattering and reverberating to achieve focusing at the target location. It requires a ring of antennas surrounding the human body to form a closed TRC. The prototype of a ballistic multi-antenna TR system is shown in Figure 5-14. A multi-channel digital oscilloscope and an arbitrary wave generator is connected to several antennas around the human body to perform nonlinear TR.

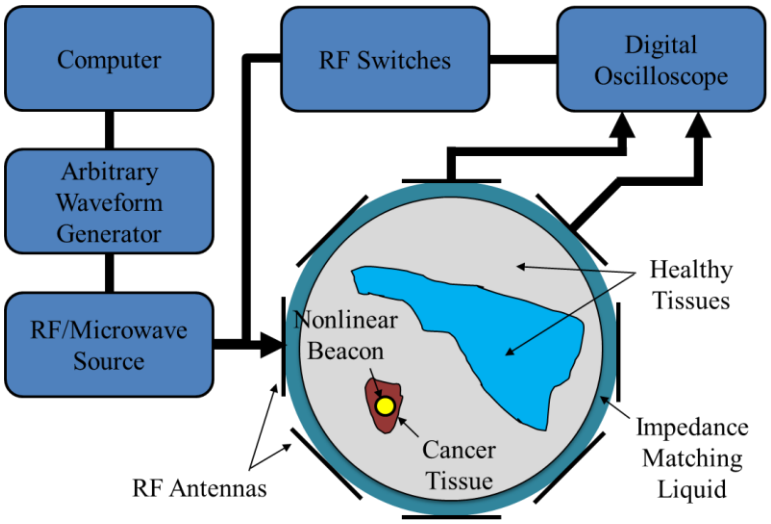

Figure 5-14 A multi-antenna TR hyperthermia system prototype

Ballistic configuration, in principle, takes place when there will be no scattering between RF source and receiver antenna. This not exactly the case shown in Figure 5-14 where we have several antennas surrounding lossy neck model and some scattering will take place on different permittivity objects. However, we wanted to stress that in contrary to the case of reverberating cavity where signal is reflected many times, here most of energy

is exchanged without major reflections. Such “ballistic” configuration should allow in future for applying similar techniques as proposed recently in optics to improve TR focusing [114]. For example, it was already reported an approach for dynamic cancellation of diffuse background in the case of focused inside of deep biological tissue high-resolution fluorescence imaging [115].

To assess the focusing quality in a ballistic TR system, the TR process with an active source placed at the tumor site is tested. As a follow-up study of the 2D neck model discussed in Chapter 4, the model is constructed and simulated in CST MICROWAVE STUDIO®. The permittivity map is built as a simplified version of the neck anatomy [116] with a variety of tissue configurations as shown in Figure 5-15. The picture on the left shows the real CT data of a young female adult, while on the right the rough area of different tissue types are marked with elliptical shapes in the simplified permittivity map used in the simulations. A malignant tumor is added to the normal anatomy to mark the focusing target.

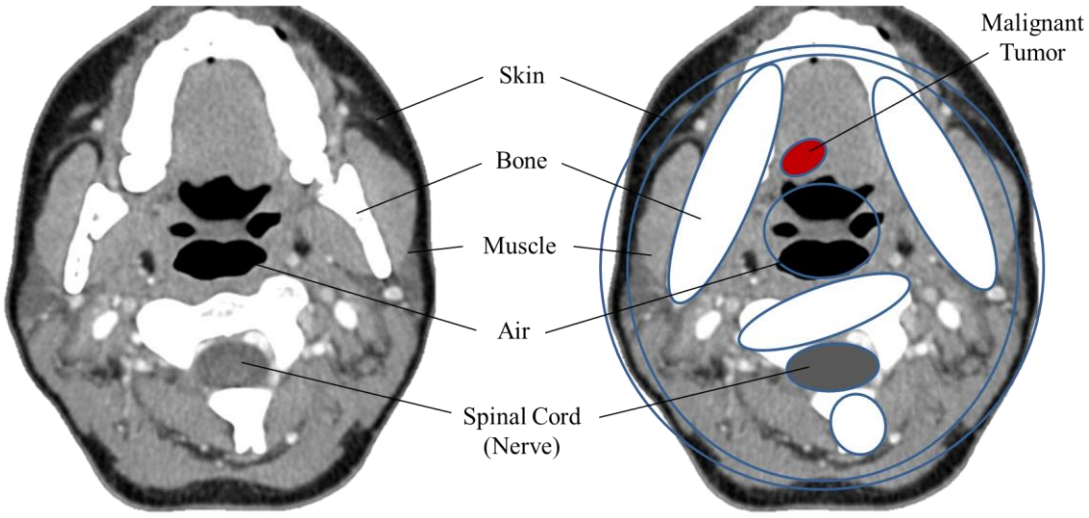

Figure 5-15 Simplified permittivity map from a normal CT of the neck

The dielectric properties of tissues are modelled by the 2nd order Cole-Cole model as shown in (4.1). In this study, we use the parameters of first two terms in the 4th order Cole-Cole model developed by Gabriel *et al.* [103] shown in Table 5-1. The real and imaginary part of the neck complex permittivity from 0 – 5 GHz is plotted in Figure 5-16.

Table 5-1 Parameters of the 2nd order Cole-Cole model for tissues in the neck

Tissue Type	ε_∞	$\Delta\varepsilon_1$	τ_1 [ps]	α_1	$\Delta\varepsilon_2$	τ_2 [ps]	α_2	σ [S/m]
Skin	4	32	7.23	0	1100	32480	0.2	0.0002
Bone	2.5	10	13.26	0.2	180	79580	0.2	0.02
Muscle	4	50	7.23	0.1	7000	353.68	0.1	0.2
Nerve	4	26	7.96	0.1	500	106100	0.15	0.006
Tumor	6.75	25.61	7.22	1	23.91	15.3	1	0.79

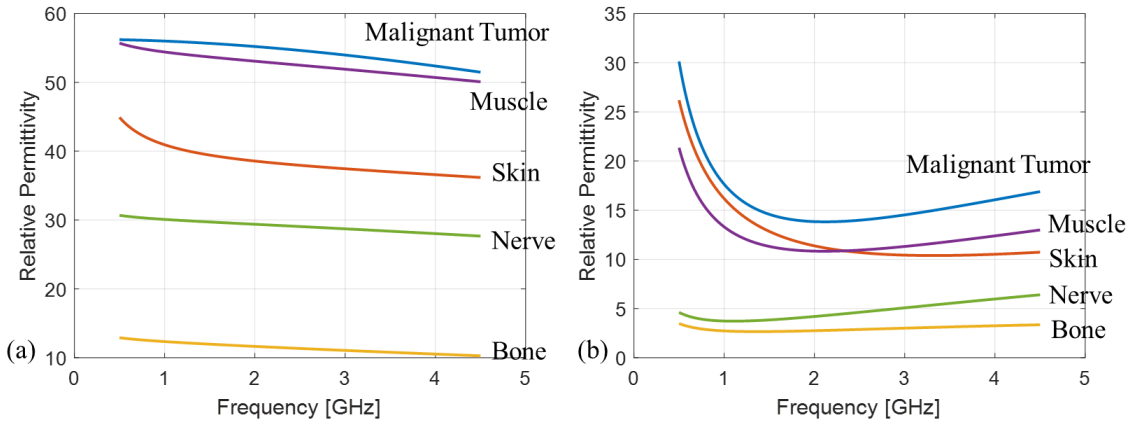

Figure 5-16 Relative permittivity of tissues in the neck model: (a) real part; (b) imaginary part

In the simulation, the radius of the round shape neck is 6 cm, surrounded by eight antennas as TRMs equally distributed in phase, each of which are placed 7 cm away from the shape center. The energy distribution is shown in Figure 5-17 after the TR is applied. A 7 ns Gaussian pulse at 2.4 GHz is used as the original signal.

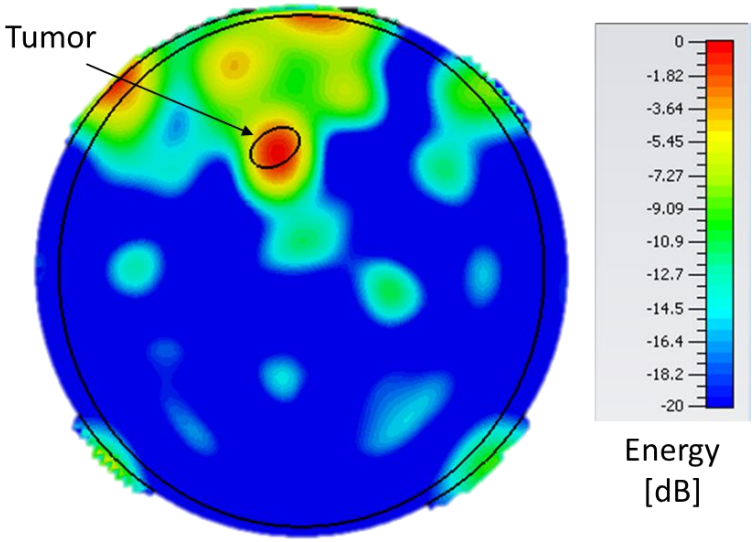

Figure 5-17 Energy distribution of the neck model after the TR process, tumor is the elliptical shape inside the circle, the other tissues are omitted

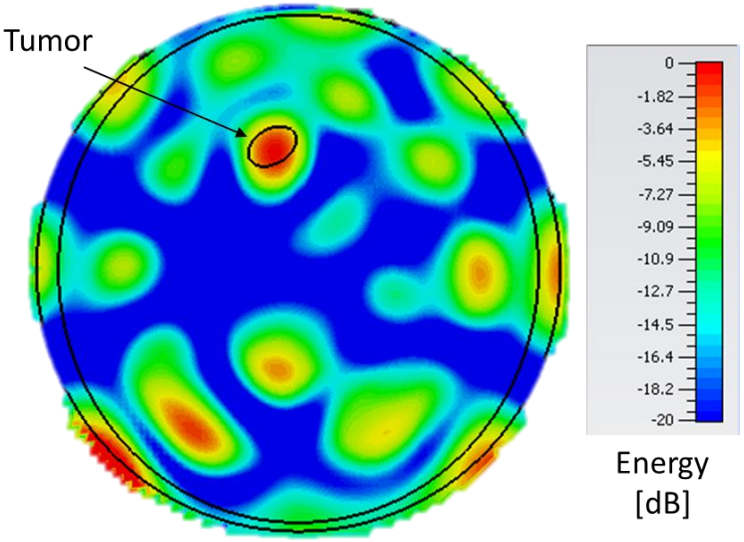

Figure 5-18 Energy distribution of the neck model after equal magnitude correction in TR

The distinctive focusing occurs at the malignant tumor site which is marked by an ellipse inside. The half power focal area size is about 1 cm by 2 cm. However, the spurious

hot spot is seen at the top left corner. Following the proposed scheme from Chapter 4, the correction is performed by setting each antenna to equal magnitude (the correction factor $p = 0$). The energy distribution after the magnitude correction is shown in Figure 5-18. Compare to $p = 1$ case, it is seen that the focal area is reduced to 1 cm by 1 cm. However, the unwanted hot spots is increased. The possible reason could be that the original pulse in the simulation is not centered at the optimum frequency. Also the wider bandwidth from broadband signal may introduce other losses to induce the spurious hot spots.

Chapter 6 Thermal Effects of TR

According to the intrinsic focusing properties of TR, the EM energy is selectively focused at the targeted location, which is proportionally converted to heat due to the loss in the tissue, resulting in an increase in local temperature. The hyperthermia requires the tissues to be heated to a certain temperature, namely 41-45 °C. At the same time the heating on the healthy tissues should be avoided. Therefore it is important to evaluate the elevated temperature and the selectivity of the heating effect from the EM TR.

Preliminary simulation results demonstrate that the electric field is discriminatively focused at the original source location in a wave-chaotic system, such as the 3D Gigabox shown in Figure 5-3. From the bioheat equation in (2.23), the temperature should rise accordingly with respect to the spatial focusing profile. To further study the heating effect in a two-channel reverberating environment, the experiments are designed and conducted to test the actual amount of the temperature rise, as well as the distribution of thermal effects.

6.1 Experimental Setup

The TR process is controlled by a MATLAB program written by the University of Maryland Gemstone TESLA team. Microwave switch assemblies are employed to shift the system between the forward and backward step. The TR system in the 3D Gigabox is set up as shown in Figure 6-1.

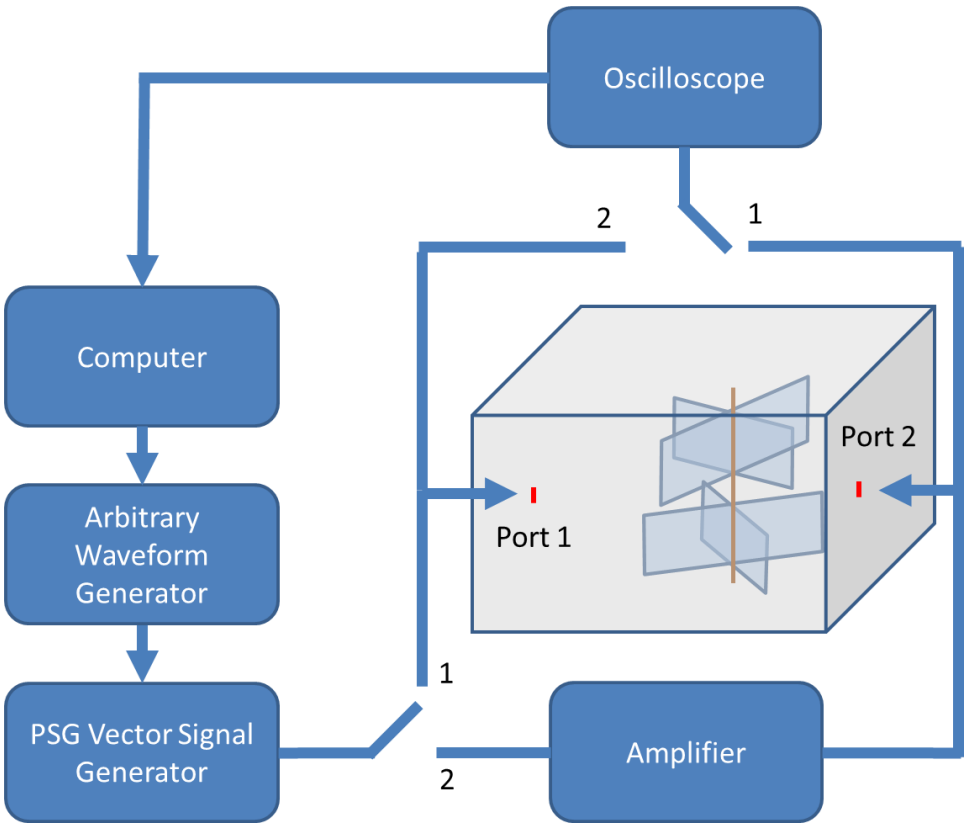

Figure 6-1 Control of TR process in the 3D Gigabox

The system performs the forward step of TR process when the switches are at position 1. The source signal read from the computer with controlled shape, duration, carrier frequency and input power, is then generated from a Tektronics AWG7052 arbitrary waveform generator and an Agilent E8267D PSG vector signal generator. The generated waveform is transmitted into the system from Port 1. After the source signal propagating through the reverberating environment, the sona signal is received at Port 2, which is connected to an Agilent Infiniium DSO91304A digital storage oscilloscope. The received sona is filtered and time-reversed through the connected computer.

The backward step is a symmetric process by changing the switches to position 2. The time-reversed sona is sent from Port 2 by the signal generator, followed by the reconstructed signal recorded by the oscilloscope at Port 1.

6.2 Water Heating

A preliminary test of the heating effect from the EM TR in the Gigabox was done to measure the temperature rise of water placed at the source location. The antennas operated in the experiment are shown in Figure 6-2.

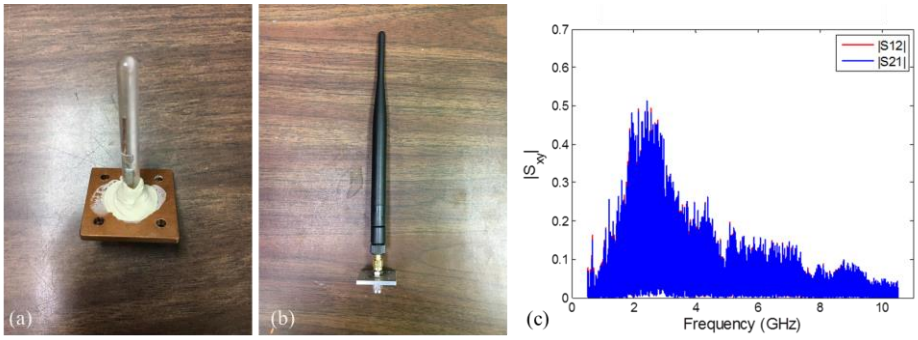

Figure 6-2 The antenna configurations for the heating experiment: (a) a 2.4GHz monopole antenna in the tube with water; (b) a 2.4 / 5GHz dual band Wi-Fi antenna; (c) transmission coefficients between these two antennas through the Gigabox

The 2.4 GHz monopole antenna depicted in Figure 6-2(a) is loaded in a 50mm long glass tube filled with tap water and mounted on the Gigabox as the original source. A tube sealing compound is used to close the open end of the tube without disturbing the EM fields. On the opposite side of the Gigabox, a 2.4 GHz and 5 GHz dual band Wi-Fi antenna in Figure 6-2(b) is installed, functioning as a TRM. The S_{21} of the Gigabox is displayed in Figure 6-2(c), showing a good transmission at the operating frequency 2.4 GHz between the two antennas.

Then the TR is performed with the water tube inside the Gigabox, transmitting a 50 ns wide Gaussian pulse at 2.4 GHz from the monopole antenna in the water. The forward incident power of the source signal is 0 dBm, while the backward incident power on the PSG to transform the time-reversed sona is increased to 25 dBm. After the TR process, the

reconstructed signal has the similar Gaussian shape as the original pulse, with an amplitude of approximately 1.1V, as shown in Figure 6-3.

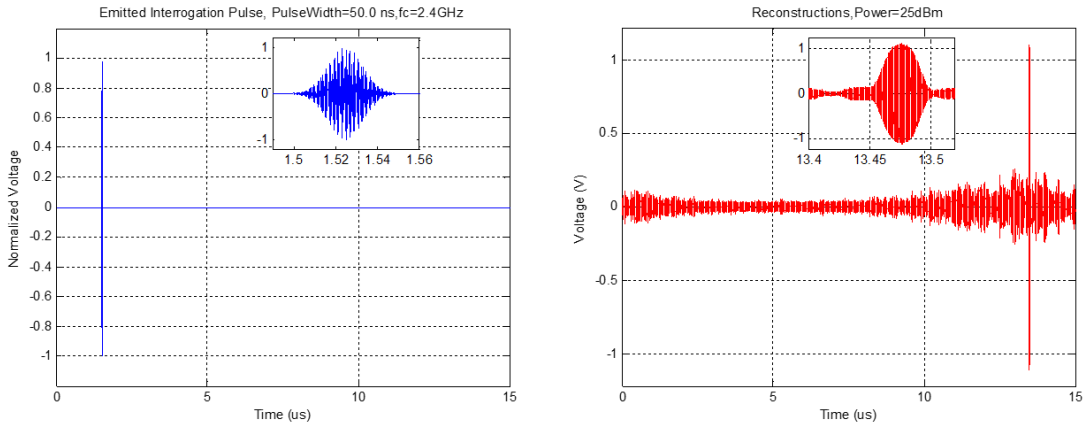

Figure 6-3 The original source and reconstructed signal in the 2.4 GHz water heating TR process

In order to measure the temperature rise, the 2.4 GHz monopole antenna inside the water is replaced by a temperature sensor. The filtered time-reversed sona recorded from the reconstruction process is sent continuously from the dual band Wi-Fi antenna in a 15 μs period, which is a 100% duty cycle. A Hewlett Packard 83020A power amplifier is utilized to boost the input power by 30 dB. The signal is turned off after it reached the equilibrium for cooling. The temperature in the water is thereby measured by an Opsense fiber optical sensor. The temperature change over time is shown in Figure 6-4. At first, the heating effect overwhelms the cooling, showing a slope $\Delta T/\Delta t$ of 5.88×10^{-3} °C/s. After about 15 minutes the equilibrium is reached. It is seen that the temperature has raised for approximately 2 degrees. After the signal is turned off, the temperature starts to drop immediately. It takes about another 15 minutes to go back to the room temperature, completing the full heating and cooling curve.

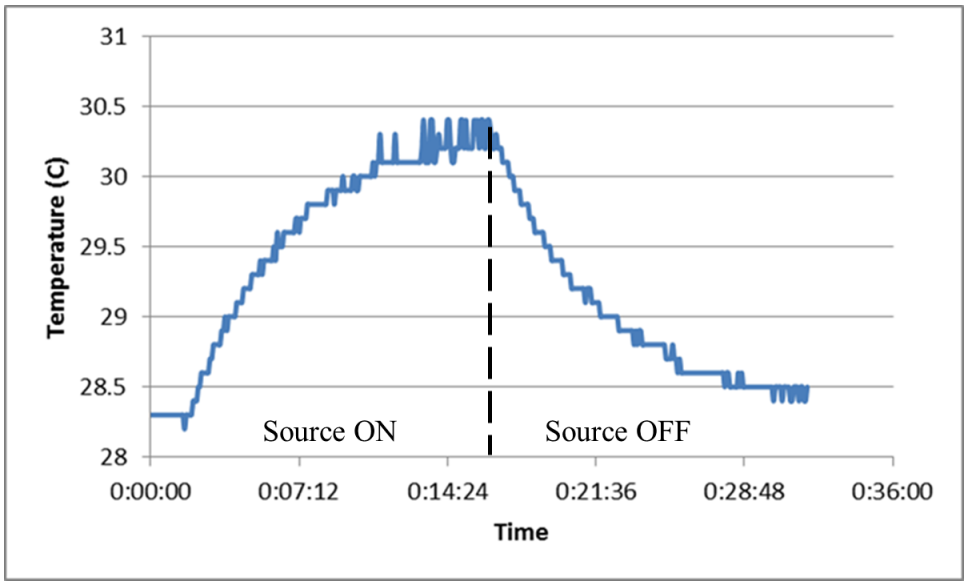

Figure 6-4 The temperature *vs* time for water heating at 2.4 GHz

The temperature rise clearly demonstrate the heating effect of the EM TR. It further proves the heating comes merely from the TR since the temperature drops immediately when the source is turned off.

6.3 Temperature Distribution

The hyperthermia for cancer treatment requires not only the elevation of temperature, but also the selectivity of heating. The former has been proved by the preliminary experiment in watering heating. Hence it is necessary to show that the heating happens the most significantly at the target location. To go one step further from the water heating experiment, temperature sensor is placed at multiple locations to build a heating profile.

A gelled phantom [117] is introduced to help establish a temperature map as it has similar permittivity and thermal conductivity properties to human tissues. The gelled phantom used in the experiment consists of 8 g/L Polyacrylic Acid partial sodium salt (PAA, part 43 636-4 from Aldrich Chemical) and 0.70 g/L Sodium Chloride (NaCl). The

2.4 GHz monopole antenna is inserted in the center of a 50mm long glass test tube filled with the gelled phantom which has a conductivity of 0.26 S/m. The material is viscous, yet stable in the test tube. The tube sealing compound is employed to fix the tube position. The TR was performed for the gelled phantom at 2.4 GHz with the reconstructed signal shown in Figure 6-5.

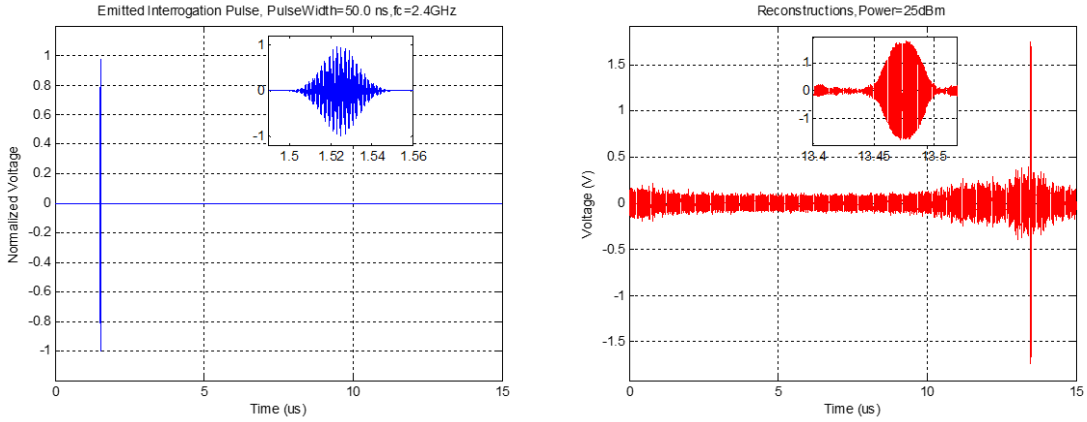

Figure 6-5 The original source and reconstructed signal in the 2.4 GHz gelled phantom heating TR process

The reconstructed signal has an amplitude of approximately 1.8V, which is better than the reconstruction in the water at the same frequency. The temperature was measured following the same procedure as the water heating experiment. A reference sensor in air was placed inside the Gigabox 2 cm to the left of the glass tube filled with gelled phantom. The temperature *versus* time plot is shown in Figure 6-6.

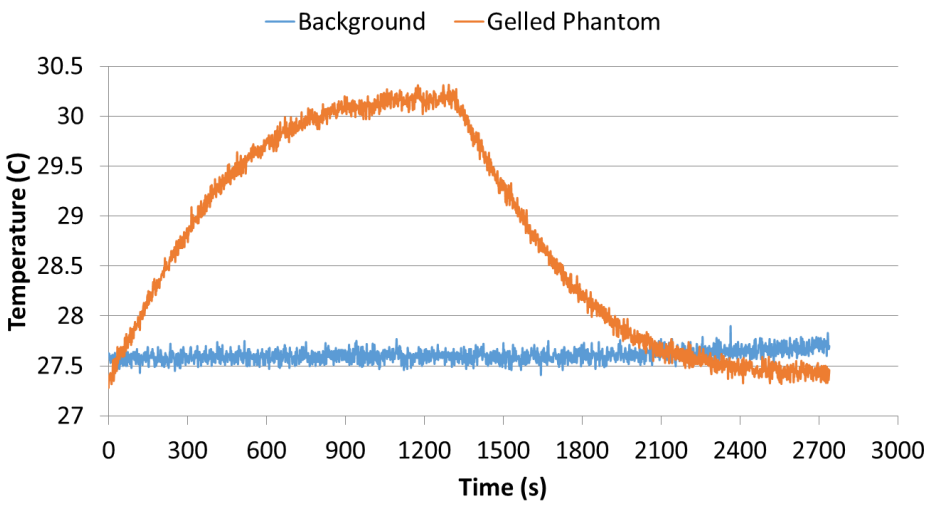

Figure 6-6 The temperature *vs* time for gelled phantom heating at 2.4 GHz

The gelled phantom has a maximum temperature rise of 2.8 °C, at the same time the background air temperature remains stable with no change during the measurement. It again proves the heating is originated from the EM TR source. The heating curve reaches the equilibrium after approximately 900 s with the slope $\Delta T/\Delta t$ about 6.5×10^{-3} °C/s Compared to tap water it has a more rapid heating performance.

We propose two ways to build a temperature map: one is to measure while moving the temperature sensor with the tube along one direction, the other is to measure temperatures at multiple positions in a broader area.

6.3.1 1D Distribution

Instead of getting the temperature at a stationary point, the temperature map could be built by moving the temperature sensor together with the glass tube. A Physik Instrumente C842 motor controller is employed to shift the tube position externally-mounted on a PI MikroMove M-415.DG translation stage as shown in Figure 6-7(a), using a program written by the University of Maryland Gemstone TESLA team. The moving

stage controls the altitude of a sliding panel which is a part of the Gigabox wall and the enclosure remains sealed during the translation.

The moving stage was initially centered at the target point where the TR reconstruction was done in Figure 6-5, marked as the reference zero point. The experiment covers an 11 cm length along *y*-axis as the stage moves from −5.5 cm to 5.5 cm as shown in Figure 6-7(b). The temperature was measured every 1 cm, so there are 12 positions in total, plus the one at the center. The stage is stabilized during the temperature measurement as the synchronization between the moving stage and the TR procedure is taken care of by another MATLAB program.

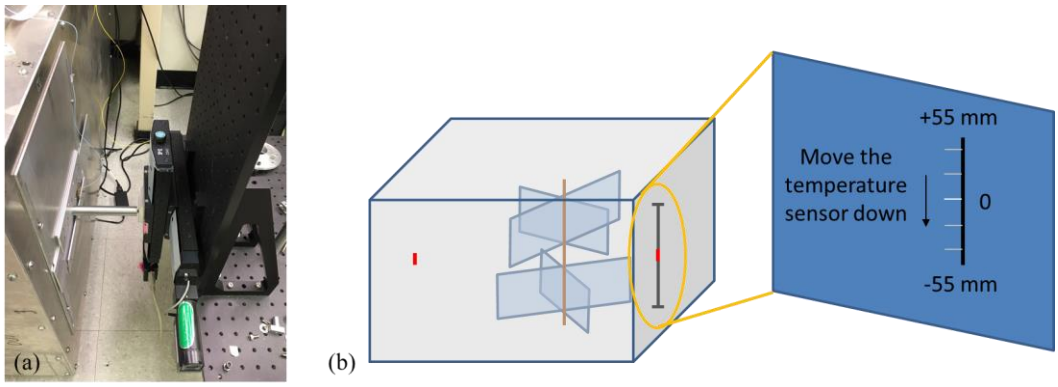

Figure 6-7 Experimental setup for measuring the temperature distribution along an axis: (a) a sliding panel controlled by the moving stage; (b) schematic drawing of the move along *y*-axis

Before the temperature measurement, the peak-to-peak reconstruction amplitude was measured as shown in Figure 6-8, following the same procedure in Cangialosi *et al*. [118] The peak-to-peak voltage tops its value at the center point, indicating the strongest reconstruction at the target location.

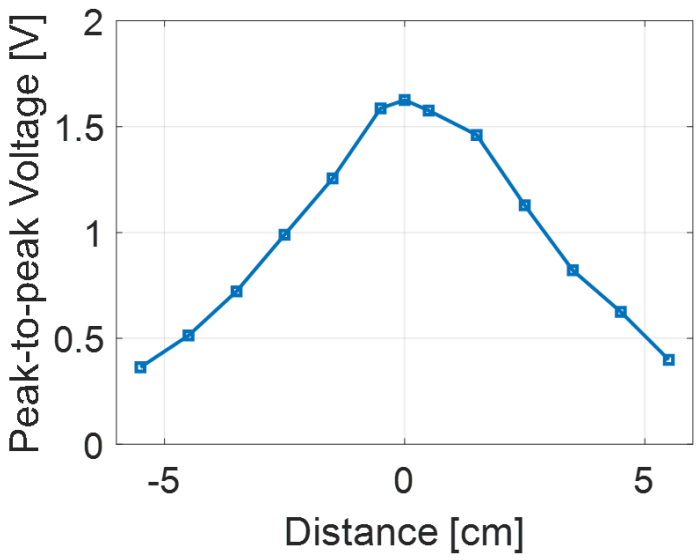

Figure 6-8 Spatial profile of peak-to-peak voltage along a line at 2.4 GHz

The build a heating profile along the *y*-axis, the experiment was done in the following steps: First, the 2.4 GHz monopole antenna was loaded into the test tube with gelled phantom and mounted on the stage, which is centered at the reference zero point. Then we performed the TR and recorded the filtered sona signal. After the TR process, the antenna was taken out from the gelled phantom and the temperature sensor was put in, keeping the environment unvarying. The filtered time-reversed sona was continually broadcast into the cavity once every 15 μs and the temperature at the center was measured. The stage was moved to the lower limit, i.e., −5.5cm, afterwards, scanning along the *y*-axis and measuring the temperature every 1 cm till it reaches the upper limit 5.5 cm. The temperature was measured by turning on the signal for 30 minutes and then shut down the signal for another 30 minutes. There was 12 temperature curves measured in total. The maximum ΔT at these measured points are shown in Figure 6-9.

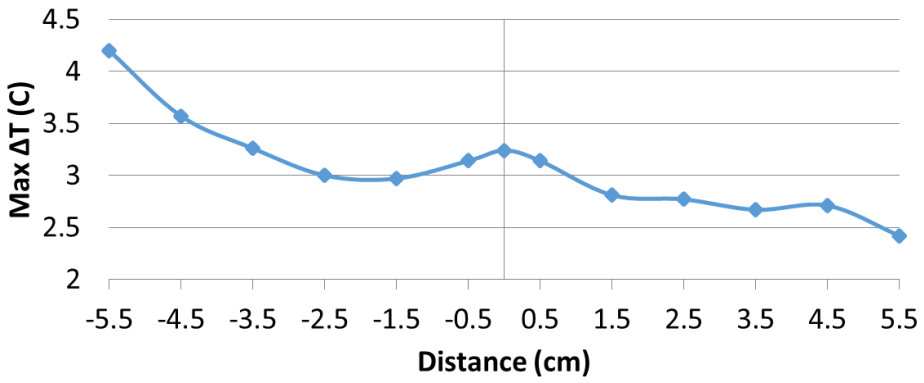

Figure 6-9 The maximum temperature rise *versus* distance

The temperature distribution does not quite follow the peak-to-peak voltage distribution. The reason could be the move of the tube perturbs the environment, resulting in the sona signal no longer adaptive to the new atmosphere. It could be also some background heating happened at around −5.5 cm from the temperature gradient of the Gigabox. Additionally, unlike the voltage in Figure 6-8, the temperature change depends on the total energy in the reconstructed signal, which is related to the integration over time. Therefore the experiment should be repeated with controlled variables and corrections.

6.3.2 2D Distribution

A major drawback of the experiment on the translating stage is that a large amount of dielectric is moving during the experiment. The environment is varying at each point, thus leading to the inaccuracy of the temperature measurement results. Hence an improved experiment is designed by keeping the gelled phantom fixed in the environment. The gelled phantom is now put inside a 2 inch by 2 inch square plastic box with 1 inch height as shown in Figure 6-10(a). The box was then taped on the wall of the Gigabox in Figure 6-10(b). On the top surface of the box, several holes were drilled with the dimension marked in Figure 6-10(c) which allows the antenna and the temperature sensor to go through.

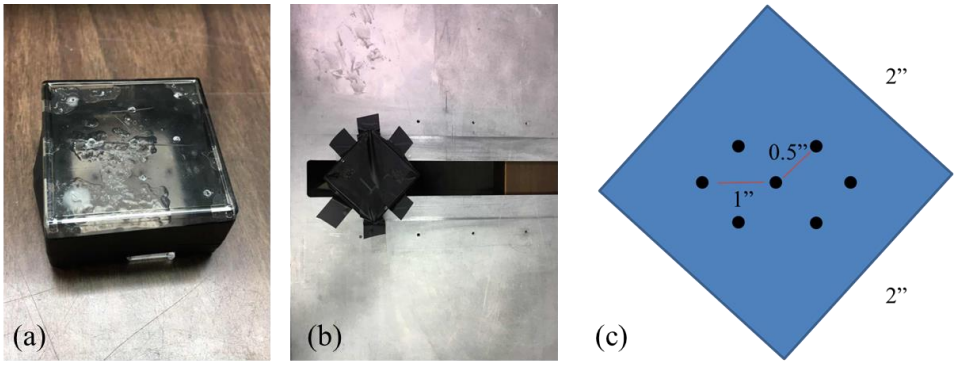

Figure 6-10 Experimental setup for measuring the temperature distribution within an area: (a) a box filled with gelled phantom; (b) the box taped on the wall of the Gigabox; (c) schematic drawing of the holes on the surface

Multiple temperature sensors are needed in building a temperature map over the box area. Ideally the temperature change over time could be accomplished by putting one sensor at the center to monitor the expected reconstruction, together with other sensors placed around for comparison. In this particular experiment, one sensor at the center and the other sensor positioned 1” to the right of the center were used to qualitatively compare the difference. Because of the large volume of the gelled phantom, it takes longer to reach equilibrium, so the temperature is measured with the sona signal turned on for 2 hours and off for another 2 hours. The temperature *versus* time dependence are shown in Figure 6-11.

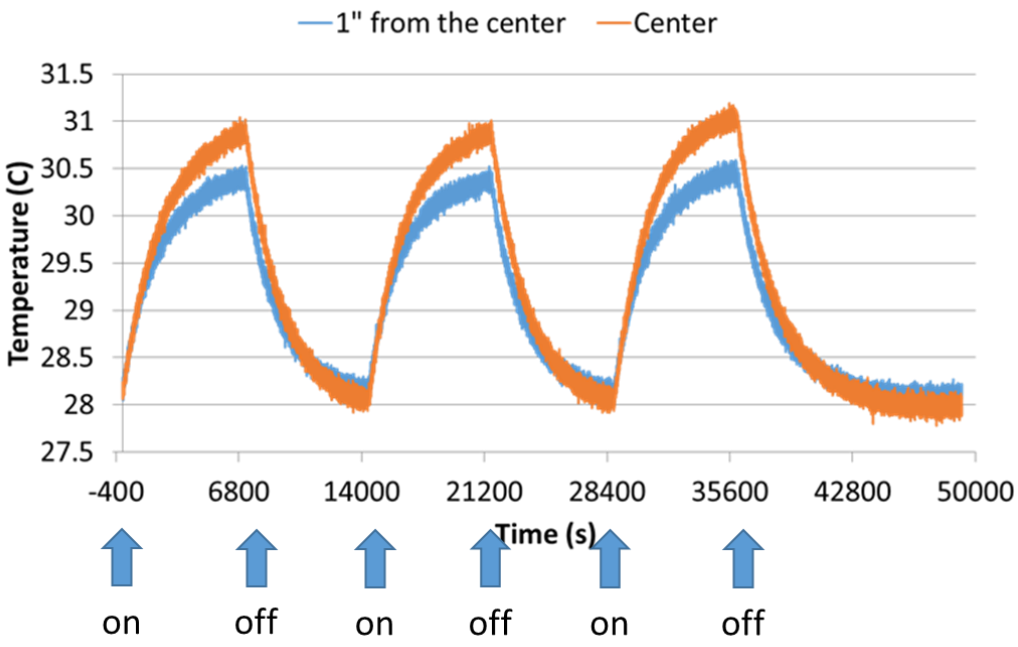

Figure 6-11 Temperature *vs* time for two sensors at different place

The result shows that the temperature rise at the center is approximately 0.5 °C larger than on the side. This experiment proves both the intensity and selectivity of the heating effects from EM TR, proposing a promising application of TR in hyperthermia.

6.4 Clinical Prospects

By employing more antennas, a complete EM TR system will ultimately be able to focus RF power instantaneously and precisely at each tumor location. The two non-invasive focusing methods proposed in this dissertation, would both lead to encouraging future clinical prospects. The MRI-guided TR will be developed in order to generate customized permittivity maps. Depending on the simulation of real-time MRI data, it allows TR to instantaneously adjust the phase and amplitude of the antennas, which is improvement in personalized treatment. At the same time, the nonlinear beacon candidates, such as ferromagnetic materials or nanoparticles, could be placed during biopsy or injected. It opens a promising way to spatially encode the internal tumor site. A key step forward is

to test the *in vivo* performance of TR in animal tumor models before the system is applied clinically for non-invasive ablation, thermal drug delivery, and permeability control of blood brain barrier (BBB). Thanks to its advantages of noninvasiveness, low ionizing radiation, and selectivity in destroying cancer cells, the development of larger-scale clinical TR systems will likely improve survival rates and quality of life for cancer patients, especially those afflicted by late-stage cancers.

Chapter 7 Conclusions and Future Work

7.1 Conclusions

Time reversal (TR) is a promising method for targeted thermal cancer treatment due to its intrinsic focusing concept. This dissertation presents a thorough assessment of TR techniques to-be-used for RF hyperthermia using the analytical model, full-wave EM simulations and experimental approaches.

First, a simple analytical model was developed for the neck tumor. The neck is modeled as an infinite length dielectric cylinder filled with muscle as a homogeneous medium. The TR process is converted into a 2D line current source scattering problem. Both the time-forward and time-reversed Green's function were solved analytically from the Helmholtz equation. Temporal focusing was quantified by calculating the cross-correlation between the reconstructed signal and the original signal. It is proved that the quality of the reconstruction is good, given that the maximum cross-correlation occurs at zero delayed time.

The spatial focusing issue was converted into an optimization problem of basic parameters with several energy constraints compiled from clinically relevant criteria. Based on an asymptotic study in a closed time-reversal cavity (TRC), the focal spot size is defined and spatial resolution is hence calculated. The best possible spatial resolution, found here for the cylinder shape, is 0.38 wavelength, which is beyond the diffraction limit because the focusing is achieved at near-field. The influence of the center frequency of the source signal was investigated, indicating that higher frequency leads to smaller focal spot size, however, it was also found that some of the energy constraints might not be satisfied. The optimization process was elaborated to find the optimum frequency and 1.26 GHz was

selected. Moreover, it was concluded that for a source signal with Gaussian-modulated shape, the spatial focusing from a broadband signal cannot triumph that from a single frequency signal.

Additionally, the spatial focusing profile from a finite number of TRMs is analyzed. The position of the focal point was found as dependent on the phase of each TRM, while the magnitude as controlling the shape of the spot. By multiplying a correction factor in the power of the magnitude, the quality of spatial focusing is improved.

Secondly, simulation tools such as CST MICROWAVE STUDIO® have been used to study the feasibility of TR in hyperthermia. Dimensions and parameters of the reverberating cavity (GigaBox) system [112] were used for simulations. Two approaches on how to avoid insertion of the real transmit signal antenna into the tumor were proposed and analyzed. The first method was to put into a tumor location an internal virtual source, which could provide a signal. Both the temporal and spatial focusing from TR was observed when carrying out full-wave simulations in a two-channel reverberating system. The second approach was to place a nonlinear beacon into the tumor to spatially encode its site. A nonlinear port with rectifying circuit was added to the linear cavity as a beacon. It is proved that the spatial focusing is spotted at the nonlinear beacon without using any internal sources. Furthermore, a simplified neck model that consists of different tissue types is built to test the ballistic TR. The results show that the EM energy is focused at the tumor site. The focusing is further improved by setting an equal magnitude on each TRM.

Finally, experiments with a reverberating cavity system were designed and conducted to test the temperature change and the selectivity of the heating effects from EM TR. First, heating of a water-filled quartz tube placed at the original source location was

tested in the GigaBox. The temperature rise of about 2 degrees clearly demonstrate the heating effect of the EM TR technique. To go one step further, a gelled phantom, which has similar permittivity, conductivity and thermal conductivity properties to human tissues, is employed to build a temperature profile over the original source location. The 1D and 2D temperature distribution is measured and analyzed in the gelled phantom. The temperature at the original source location is about a half degree higher than the temperature on the edge, which confirms the selectivity of TR based heating.

Spatio-temporal focusing of TR has been demonstrated by employing the theoretical model analysis and finite element method simulation. It was also confirmed by experimental results. Experiments carried out in a wave-chaotic cavity have clearly demonstrated the thermal effects initiated by TR technique, as well as RF focusing effects.

TR introduced RF focusing seems to be very well suited for thermally released drug delivery technique. There is no need for high RF power when using this modality because only 1 or 2 degrees increase of temperature is needed what makes requirements for suppression of spurious hot spots not that strict. Drug delivery process should maximize both delivered dosage and toxicity to the cancer, but at the same time normal cells should not be affected. Required selectivity of such process depends on delivery of local heat to the tumor, which requires heat source to be focused onto the tumor side only. Such technique in most of cases relies on thermally responsive liposomes [119] or nanoparticles working as heat enhancers [120, 121].

It is concluded that time reversal is a reliable method to apply focused RF hyperthermia in the cancer treatment.

7.2 Comparison

There are similarities between the TR technique and the traditional adaptive phased array as they both make adjustments to the magnitude and phase of antenna signals to achieve focusing. However, the TR technique has the following advantages: (i) TR calculates the field distribution based on only the information of the source location and the complex media. It does not require the iterative runs of an optimization procedure, in which individual field distribution for each antenna of the array is computed. So the TR technique significantly accelerates the speed of adapting to environmental changes, which is important in the case of complex tumor shapes or movement of the patient; (ii) Compared to the narrowband excitation in the traditional phased array, TR is applicable for both continuous and pulsed, broadband and narrowband waves due to its intrinsic focusing property. The extra degree of freedom in the source signal type allows the focusing profile to be manually built. The spectrum of the source signal could be manipulated based on the Green's function of the media to achieve better focusing, which is beneficial to develop cancer type specific and patient specific therapies.

7.3 Future Work

As for the analytical model, based on the Green's function from the asymptotic study, the source signal spectrum should be manipulated to get better focusing in this particular configuration. The magnitude correction methods should be better studied by employing the generalized Rayleigh quotient to optimize the energy distribution. Additionally, another energy constraint, the tumor energy ratio, should be considered. It is defined as the energy deposited in a given region, e.g., the tumor region acquired from the pretherapeutic MRI or CT scan, relative to the total energy inside the cylinder. Using this

energy constraint, the optimum frequency would depend on the tumor size. Finally, the 3D model can be solved similarly to better guide the choice of the TR source signal.

Thermal simulations, showing the temperature rise or SAR, can be carried out for the 3D Gigabox as a verification to the experimental results. The nonlinear beacon methods can be simulated in the ballistic TR. More specific performance indicators can be defined to quantify the spatial focusing in the ballistic approach. Corresponding experiments should also be conducted.

The ultimate goal for this research is to build a multi-antenna prototype of the TR hyperthermia system. It would likely be combined with MRI to get instantaneous and personalized focusing. The *in vivo* performance should first be tested on animal tumor models. Finally, the system could be employed for selected applications, such as permeability control of blood brain barrier (BBB), thermally induced drug delivery, hyperthermia, and non-invasive ablation.

References

11[1] World Health Organization. *Cancer*. Available: http://www.who.int/cancer/en/

[2] J. Ferlay, I. Soerjomataram, R. Dikshit, S. Eser, C. Mathers, M. Rebelo, D. M. Parkin, D. Forman, and F. Bray, "Cancer incidence and mortality worldwide: sources, methods and major patterns in GLOBOCAN 2012," *International journal of cancer*, vol. 136, 2015.

[3] American Cancer Society. *Key Statistics for Lung Cancer*. Available: https://www.cancer.org/cancer/non-small-cell-lung-cancer/about/key-statistics.html

[4] N. Howlader, A. M. Noone, M. Krapcho, D. Miller, K. Bishop, S. F. Altekruse, C. L. Kosary, M. Yu, J. Ruhl, and Z. Tatalovich, "SEER Cancer Statistics Review, 1975-2013, National Cancer Institute. Bethesda, MD," ed, 2016.

[5] A. B. Miller, B. Hoogstraten, M. Staquet, and A. Winkler, "Reporting results of cancer treatment," *cancer*, vol. 47, pp. 207-214, 1981.

[6] G. Housman, S. Byler, S. Heerboth, K. Lapinska, M. Longacre, N. Snyder, and S. Sarkar, "Drug resistance in cancer: an overview," *Cancers*, vol. 6, pp. 1769-1792, 2014.

[7] J. van der Zee, "Heating the patient: a promising approach?," *Ann Oncol*, vol. 13, pp. 1173-84, Aug 2002.

[8] P. Wust, B. Hildebrandt, G. Sreenivasa, B. Rau, J. Gellermann, H. Riess, R. Felix, and P. M. Schlag, "Hyperthermia in combined treatment of cancer," *Lancet Oncol*, vol. 3, pp. 487-97, Aug 2002.

[9] A. Chicheł, J. Skowronek, M. Kubaszewska, and M. Kanikowski, "Hyperthermia–description of a method and a review of clinical applications," *Reports of Practical Oncology & Radiotherapy,* vol. 12, pp. 267-275, 2007.

[10] J. van der Zee, D. González, G. C. van Rhoon, J. D. P. van Dijk, W. L. J. van Putten, and A. A. M. Hart, "Comparison of radiotherapy alone with radiotherapy plus hyperthermia in locally advanced pelvic tumours: a prospective, randomised, multicentre trial," *The Lancet,* vol. 355, pp. 1119-1125, 2000.

[11] C. A. Quinto, P. Mohindra, S. Tong, and G. Bao, "Multifunctional superparamagnetic iron oxide nanoparticles for combined chemotherapy and hyperthermia cancer treatment," *Nanoscale,* vol. 7, pp. 12728-12736, 2015.

[12] S. A. Meenach, J. Z. Hilt, and K. W. Anderson, "Poly (ethylene glycol)-based magnetic hydrogel nanocomposites for hyperthermia cancer therapy," *Acta Biomaterialia,* vol. 6, pp. 1039-1046, 2010.

[13] S. N. Goldberg, "Radiofrequency tumor ablation: principles and techniques," *European Journal of Ultrasound,* vol. 13, pp. 129-147, 2001.

[14] P. F. Turner, "Regional hyperthermia with an annular phased array," *IEEE Trans Biomed Eng,* vol. 31, pp. 106-14, Jan 1984.

[15] D. Sullivan, "Mathematical-Methods for Treatment Planning in Deep Regional Hyperthermia," *Ieee Transactions on Microwave Theory and Techniques,* vol. 39, pp. 864-872, May 1991.

[16] F. Bardati, A. Borrani, A. Gerardino, and G. A. Lovisolo, "SAR optimization in a phased array radiofrequency hyperthermia system," *IEEE Transactions on biomedical engineering,* vol. 42, pp. 1201-1207, 1995.

[17] A. J. Fenn and G. A. King, "Experimental investigation of an adaptive feedback algorithm for hot spot reduction in radio-frequency phased-array hyperthermia," *Ieee Transactions on Biomedical Engineering,* vol. 43, pp. 273-280, Mar 1996.

[18] K. D. Paulsen, S. Geimer, J. W. Tang, and W. E. Boyse, "Optimization of pelvic heating rate distributions with electromagnetic phased arrays," *International Journal of Hyperthermia,* vol. 15, pp. 157-186, May-Jun 1999.

[19] H. Kroeze, J. B. Van de Kamer, A. A. C. De Leeuw, and J. J. W. Lagendijk, "Regional hyperthermia applicator design using FDTD modelling," *Physics in Medicine and Biology,* vol. 46, pp. 1919-1935, Jul 2001.

[20] P. Wust, M. Seebass, J. Nadobny, P. Deuflhard, G. Monich, and R. Felix, "Simulation studies promote technological development of radiofrequency phased array hyperthermia," *International Journal of Hyperthermia,* vol. 12, pp. 477-494, Jul-Aug 1996.

[21] M. Seebass, R. Beck, J. Gellermann, J. Nadobny, and P. Wust, "Electromagnetic phased arrays for regional hyperthermia: optimal frequency and antenna arrangement," *International Journal of Hyperthermia,* vol. 17, pp. 321-336, Jul-Aug 2001.

[22] S. K. Das, E. A. Jones, and T. V. Samulski, "A method of MRI-based thermal modelling for a RF phased array," *International Journal of Hyperthermia,* vol. 17, pp. 465-482, Nov-Dec 2001.

[23] T. Kohler, P. Maass, P. Wust, and M. Seebass, "A fast algorithm to find optimal controls of multiantenna applicators in regional hyperthermia," *Physics in Medicine and Biology,* vol. 46, pp. 2503-2514, Sep 2001.

[24] M. E. Kowalski and J. M. Jin, "A temperature-based feedback control system for electromagnetic phased-array hyperthermia: theory and simulation," *Physics in medicine and biology,* vol. 48, p. 633, 2003.

[25] L. Y. Wu, R. J. McGough, O. A. Arabe, and T. V. Samulski, "An RF phased array applicator designed for hyperthermia breast cancer treatments," *Physics in Medicine and Biology,* vol. 51, pp. 1-20, Jan 7 2006.

[26] M.-G. Di Benedetto, *UWB communication systems: a comprehensive overview* vol. 5: Hindawi Publishing Corporation, 2006.

[27] M. Converse, E. J. Bond, S. C. Hagness, and B. D. Van Veen, "Ultrawide-band microwave space-time beamforming for hyperthermia treatment of breast cancer: A computational feasibility study," *Ieee Transactions on Microwave Theory and Techniques,* vol. 52, pp. 1876-1889, Aug 2004.

[28] M. Converse, E. J. Bond, B. D. Veen, and C. Hagness, "A computational study of ultra-wideband versus narrowband microwave hyperthermia for breast cancer treatment," *IEEE transactions on microwave theory and techniques,* vol. 54, pp. 2169-2180, 2006.

[29] M. Fink, C. Prada, F. Wu, and D. Cassereau, "Self Focusing in Inhomogeneous-Media with Time-Reversal Acoustic Mirrors," *Ieee 1989 Ultrasonics Symposium : Proceedings, Vols 1 and 2,* pp. 681-686, 1989.

[30] G. F. Edelmann, T. Akal, W. S. Hodgkiss, S. Kim, W. A. Kuperman, and H. C. Song, "An initial demonstration of underwater acoustic communication using time reversal," *IEEE journal of oceanic engineering,* vol. 27, pp. 602-609, 2002.

[31] J. L. Thomas, F. Wu, and M. Fink, "Time reversal focusing applied to lithotripsy," *Ultrasonic Imaging,* vol. 18, pp. 106-121, Apr 1996.

[32] R. C. Qiu, C. Zhou, N. Guo, and J. Q. Zhang, "Time reversal with MISO for ultrawideband communications: Experimental results," *IEEE Antennas and Wireless Propagation Letters,* vol. 5, pp. 269-273, 2006.

[33] T. Strohmer, M. Emami, J. Hansen, G. Papanicolaou, and A. J. Paulraj, "Application of time-reversal with MMSE equalizer to UWB communications," pp. 3123-3127.

[34] D. Liu, G. Kang, L. Li, Y. Chen, S. Vasudevan, W. Joines, Q. H. Liu, J. Krolik, and L. Carin, "Electromagnetic time-reversal imaging of a target in a cluttered environment," *IEEE transactions on antennas and propagation,* vol. 53, pp. 3058-3066, 2005.

[35] B. Guo, L. Z. Xu, and J. Li, "Time reversal based microwave hyperthermia treatment of breast cancer," *Microwave and Optical Technology Letters,* vol. 47, pp. 335-338, Nov 20 2005.

[36] H. D. Trefna, J. Vrba, and M. Persson, "Time-reversal focusing in microwave hyperthermia for deep-seated tumors," *Physics in Medicine and Biology,* vol. 55, pp. 2167-2185, Apr 21 2010.

[37] K. A. Mauritz. *Dielectric Spectroscopy*. Available: https://web.archive.org/web/20010307184808/http://www.psrc.usm.edu:80/mauritz/dilect.html

[38] L. Sha, E. R. Ward, and B. Stroy, "A review of dielectric properties of normal and malignant breast tissue," in *SoutheastCon, 2002. Proceedings IEEE*, pp. 457-462.

[39] H. P. Schwan and K. R. Foster, "RF-field interactions with biological systems: electrical properties and biophysical mechanisms," *Proceedings of the IEEE,* vol. 68, pp. 104-113, 1980.

[40] A. J. Surowiec, S. S. Stuchly, J. R. Barr, and A. Swarup, "Dielectric properties of breast carcinoma and the surrounding tissues," *IEEE Transactions on Biomedical Engineering,* vol. 35, pp. 257-263, 1988.

[41] F. Ali and S. Ray, "SAR Analysis for handheld mobile phone using DICOM based voxel model," *Journal of Microwaves, Optoelectronics and Electromagnetic Applications,* vol. 12, pp. 363-375, 2013.

[42] H. Q. Woodard and D. R. White, "The composition of body tissues," *The British journal of radiology,* vol. 59, pp. 1209-1218, 1986.

[43] W. H. Hayt and J. A. Buck, *Engineering electromagnetics* vol. 6: McGraw-Hill New York, 1981.

[44] R. Severns. *Skin depth and wavelength in soil*. Available: http://www.antennasbyn6lf.com/files/ground_skin_depth_and_wavelength.pdf

[45] C. Furse, D. A. Christensen, and C. H. Durney, *Basic introduction to bioelectromagnetics*: CRC press, 2009.

[46] International Electrotechnical Commission, "Medical electrical equipment - Part 2-33: Particular requirements for the basic safety and essential performance of magnetic resonanceequipment for medical diagnosis," *IEC 60601-2-33:2010+AMD1:2013+AMD2:2015,* 2015.

[47] J. W. Hand, K. Hynynen, P. N. Shrivastava, and T. K. Saylor, *Methods of external hyperthermic heating*: Springer Science & Business Media, 2012.

[48] M. H. Repacholi, "Health risks from the use of mobile phones," *Toxicology letters*, vol. 120, pp. 323-331, 2001.

[49] S. Aalto, C. Haarala, A. Brück, H. Sipilä, H. Hämäläinen, and J. O. Rinne, "Mobile phone affects cerebral blood flow in humans," *Journal of Cerebral Blood Flow & Metabolism*, vol. 26, pp. 885-890, 2006.

[50] N. D. Volkow, D. Tomasi, G.-J. Wang, P. Vaska, J. S. Fowler, F. Telang, D. Alexoff, J. Logan, and C. Wong, "Effects of cell phone radiofrequency signal exposure on brain glucose metabolism," *Jama*, vol. 305, pp. 808-813, 2011.

[51] K. K. Kesari, M. Siddiqui, R. Meena, H. N. Verma, and S. Kumar, "Cell phone radiation exposure on brain and associated biological systems," 2013.

[52] G. C. Brainard, R. Kavet, and L. I. Kheifets, "The relationship between electromagnetic field and light exposures to melatonin and breast cancer risk: a review of the relevant literature," *Journal of pineal research*, vol. 26, pp. 65-100, 1999.

[53] T. Wessapan and P. Rattanadecho, "Specific absorption rate and temperature increase in the human eye due to electromagnetic fields exposure at different frequencies," *International Journal of Heat and Mass Transfer*, vol. 64, pp. 426-435, 2013.

[54] Y. Liu, J. Chen, F. G. Shellock, and W. Kainz, "Computational and experimental studies of an orthopedic implant: MRI-related heating at 1.5-T/64-MHz and 3-T/128-MHz," *Journal of Magnetic Resonance Imaging*, vol. 37, pp. 491-497, 2013.

[55] I. Hilger, W. Andrä, R. Hergt, R. Hiergeist, H. Schubert, and W. A. Kaiser, "Electromagnetic heating of breast tumors in interventional radiology: in vitro and

in vivo studies in human cadavers and mice," *Radiology,* vol. 218, pp. 570-575, 2001.

[56] ASTM International, "Standard Test Method for Measurement of Radio Frequency Induced Heating Near Passive Implants During Magnetic Resonance Imaging," *ASTM F2182-09,* 2009.

[57] H. H. Pennes, "Analysis of tissue and arterial blood temperatures in the resting human forearm," *Journal of applied physiology,* vol. 1, pp. 93-122, 1948.

[58] R. Habash, *Bioeffects and therapeutic applications of electromagnetic energy*: CRC press, 2007.

[59] R. D. Issels, "Hyperthermia adds to chemotherapy," *Eur J Cancer,* vol. 44, pp. 2546-54, Nov 2008.

[60] J. L. Roti Roti, "Cellular responses to hyperthermia (40–46 C): Cell killing and molecular events," *International Journal of hyperthermia,* vol. 24, pp. 3-15, 2008.

[61] M. L. Van der Gaag, M. De Bruijne, T. Samaras, J. Van Der Zee, and G. C. Van Rhoon, "Development of a guideline for the water bolus temperature in superficial hyperthermia," *International journal of hyperthermia,* vol. 22, pp. 637-656, 2006.

[62] P. Wust, M. Seebass, J. Nadobny, and R. Felix, "Electromagnetic deep heating technology," in *Thermoradiotherapy and thermochemotherapy*, ed: Springer, 1995, pp. 219-251.

[63] A. L. Feldman, S. K. Libutti, J. F. Pingpank, D. L. Bartlett, T. H. Beresnev, S. M. Mavroukakis, S. M. Steinberg, D. J. Liewehr, D. E. Kleiner, and H. R. Alexander, "Analysis of factors associated with outcome in patients with malignant peritoneal

mesothelioma undergoing surgical debulking and intraperitoneal chemotherapy," *Journal of Clinical Oncology,* vol. 21, pp. 4560-4567, 2003.

[64] F. K. Storm, "Clinical hyperthermia and chemotherapy," *Radiologic clinics of North America,* vol. 27, pp. 621-627, 1989.

[65] M. Nikfarjam, V. Muralidharan, and C. Christophi, "Mechanisms of focal heat destruction of liver tumors," *Journal of Surgical Research,* vol. 127, pp. 208-223, 2005.

[66] D. Haemmerich and P. F. Laeseke, "Thermal tumour ablation: devices, clinical applications and future directions," *International journal of hyperthermia,* vol. 21, pp. 755-760, 2005.

[67] M. R. Williams, M. Garrido, M. C. Oz, and M. Argenziano, "Alternative energy sources for surgical atrial ablation," *Journal of cardiac surgery,* vol. 19, pp. 201-206, 2004.

[68] C. L. Brace, "Radiofrequency and microwave ablation of the liver, lung, kidney, and bone: what are the differences?," *Current problems in diagnostic radiology,* vol. 38, pp. 135-143, 2009.

[69] D. Haemmerich and F. T. Lee, "Multiple applicator approaches for radiofrequency and microwave ablation," *International journal of hyperthermia,* vol. 21, pp. 93-106, 2005.

[70] Available: http://www.pyrexar.com/hyperthermia

[71] C. J. Simon, D. E. Dupuy, and W. W. Mayo-Smith, "Microwave ablation: principles and applications," *Radiographics,* vol. 25, pp. S69-S83, 2005.

[72] C. L. Brace, "Microwave tissue ablation: biophysics, technology, and applications," *Critical Reviews™ in Biomedical Engineering,* vol. 38, 2010.

[73] I. D. McRury and D. E. Haines, "Ablation for the treatment of arrhythmias," *Proceedings of the IEEE,* vol. 84, pp. 404-416, 1996.

[74] A. J. Fenn, "Adaptive hyperthermia for improved thermal dose distribution," *Radiation Research: A Twentieth-Century Perspective,* vol. 1, p. 290, 1991.

[75] E. M. Staderini, "UWB radars in medicine," *IEEE Aerospace and Electronic Systems Magazine,* vol. 17, pp. 13-18, 2002.

[76] M. Fink, "Time reversal of ultrasonic fields. I. Basic principles," *IEEE Trans Ultrason Ferroelectr Freq Control,* vol. 39, pp. 555-66, 1992.

[77] F. Wu, J. L. Thomas, and M. Fink, "Time reversal of ultrasonic fields. Il. Experimental results," *IEEE Trans Ultrason Ferroelectr Freq Control,* vol. 39, pp. 567-78, 1992.

[78] D. Cassereau and M. Fink, "Time-reversal of ultrasonic fields. III. Theory of the closed time-reversal cavity," *IEEE Trans Ultrason Ferroelectr Freq Control,* vol. 39, pp. 579-92, 1992.

[79] J. L. Thomas and M. A. Fink, "Ultrasonic beam focusing through tissue inhomogeneities with a time reversal mirror: application to transskull therapy," *IEEE Transactions on Ultrasonics, Ferroelectrics, and Frequency Control,* vol. 43, pp. 1122-1129, 1996.

[80] G. Lerosey, J. De Rosny, A. Tourin, A. Derode, G. Montaldo, and M. Fink, "Time reversal of electromagnetic waves," *Physical review letters,* vol. 92, p. 193904, 2004.

[81] R. Carminati, R. Pierrat, J. de Rosny, and M. Fink, "Theory of the time reversal cavity for electromagnetic fields," *Opt Lett*, vol. 32, pp. 3107-9, Nov 01 2007.

[82] A. P. Mosk, A. Lagendijk, G. Lerosey, and M. Fink, "Controlling waves in space and time for imaging and focusing in complex media," *Nature Photonics*, vol. 6, pp. 283-292, May 2012.

[83] G. Lerosey, J. de Rosny, A. Tourin, and M. Fink, "Focusing beyond the diffraction limit with far-field time reversal," *Science*, vol. 315, pp. 1120-2, Feb 23 2007.

[84] N. Chakroun, M. A. Fink, and F. Wu, "Time reversal processing in ultrasonic nondestructive testing," *IEEE transactions on ultrasonics, ferroelectrics, and frequency control*, vol. 42, pp. 1087-1098, 1995.

[85] R. K. Ing and M. Fink, "Time recompression of dispersive Lamb waves using a time reversal mirror-application to flaw detection in thin plates," pp. 659-663.

[86] H. Sohn, H. W. Park, K. H. Law, and C. R. Farrar, "Damage detection in composite plates by using an enhanced time reversal method," *Journal of Aerospace Engineering*, vol. 20, pp. 141-151, 2007.

[87] C. H. Wang, J. T. Rose, and F.-K. Chang, "A synthetic time-reversal imaging method for structural health monitoring," *Smart materials and structures*, vol. 13, p. 415, 2004.

[88] M. Fink, G. Montaldo, and M. Tanter, "Time-reversal acoustics in biomedical engineering," *Annual review of biomedical engineering*, vol. 5, pp. 465-497, 2003.

[89] M. Pernot, J.-F. Aubry, M. Tanter, A.-L. Boch, F. Marquet, M. Kujas, D. Seilhean, and M. Fink, "In vivo transcranial brain surgery with an ultrasonic time reversal mirror," *Journal of neurosurgery*, vol. 106, pp. 1061-1066, 2007.

[90] R. J. Barton, J. Chen, K. Huang, and D. G. Wu, "Cooperative time-reversal communication in wireless sensor networks," *2005 IEEE/SP 13th Workshop on Statistical Signal Processing (SSP), Vols 1 and 2*, pp. 1075-1080, 2005.

[91] C. Larmat, J. P. Montagner, M. Fink, Y. Capdeville, A. Tourin, and E. Clévédé, "Time-reversal imaging of seismic sources and application to the great Sumatra earthquake," *Geophysical Research Letters*, vol. 33, 2006.

[92] M. Fink, "Time-reversal acoustics in complex environments," *Geophysics*, vol. 71, pp. SI151-SI164, 2006.

[93] P. Kosmas and C. M. Rappaport, "Time reversal with the FDTD method for microwave breast cancer detection," *Ieee Transactions on Microwave Theory and Techniques*, vol. 53, pp. 2317-2323, Jul 2005.

[94] H. D. Trefna, P. Togni, R. Shiee, J. Vrba, and M. Persson, "Design of a wideband multi-channel system for time reversal hyperthermia," *Int J Hyperthermia*, vol. 28, pp. 175-83, 2012.

[95] C. Prada, S. Manneville, D. Spoliansky, and M. Fink, "Decomposition of the time reversal operator: Detection and selective focusing on two scatterers," *The Journal of the Acoustical Society of America*, vol. 99, pp. 2067-2076, 1996.

[96] J. d. Rosny, G. Lerosey, and M. Fink, "Theory of Electromagnetic Time-Reversal Mirrors," *IEEE Transactions on Antennas and Propagation*, vol. 58, pp. 3139-3149, 2010.

[97] H. D. Trefna, A. Fhager, and P. Takook, "Microwave hyperthermia for cancer treatment."

[98] M. Fink, "Time Reversed Acoustics," *Physics Today*, vol. 50, pp. 34-40, 1997.

[99] S. E. Martin, R. Mathur, I. Marshall, and N. J. Douglas, "The effect of age, sex, obesity and posture on upper airway size," *European Respiratory Journal*, vol. 10, pp. 2087-2090, 1997.

[100] M. M. Paulides, J. F. Bakker, and G. C. van Rhoon, "Electromagnetic head-and-neck hyperthermia applicator: experimental phantom verification and FDTD model," *International Journal of Radiation Oncology* Biology* Physics*, vol. 68, pp. 612-620, 2007.

[101] K. Ito, K. Furuya, Y. Okano, and L. Hamada, "Development and characteristics of a biological tissue-equivalent phantom for microwaves," *Electronics and Communications in Japan (Part I: Communications)*, vol. 84, pp. 67-77, 2001.

[102] S. Gabriel, R. W. Lau, and C. Gabriel, "The dielectric properties of biological tissues: II. Measurements in the frequency range 10 Hz to 20 GHz," *Phys Med Biol*, vol. 41, pp. 2251-69, Nov 1996.

[103] S. Gabriel, R. W. Lau, and C. Gabriel, "The dielectric properties of biological tissues: III. Parametric models for the dielectric spectrum of tissues," *Phys Med Biol*, vol. 41, pp. 2271-93, Nov 1996.

[104] R. F. Harrington, *Time-harmonic electromagnetic fields*: Mcgraw-Hill, 1961.

[105] M. Abramowitz and I. A. Stegun, *Handbook of mathematical functions: with formulas, graphs, and mathematical tables* vol. 55: Courier Corporation, 1964.

[106] A. B. Constantine, "Antenna theory: analysis and design," *MICROSTRIP ANTENNAS, third edition, John wiley & sons*, 2005.

[107] M. C. Gosselin, E. Neufeld, H. Moser, E. Huber, S. Farcito, L. Gerber, M. Jedensjo, I. Hilber, F. Di Gennaro, B. Lloyd, E. Cherubini, D. Szczerba, W. Kainz, and N.

Kuster, "Development of a new generation of high-resolution anatomical models for medical device evaluation: the Virtual Population 3.0," *Physics in Medicine and Biology,* vol. 59, pp. 5287-5303, Sep 21 2014.

[108] T. J. Ulrich, P. A. Johnson, and R. A. Guyer, "Interaction Dynamics of Elastic Waves with a Complex Nonlinear Scatterer through the Use of a Time Reversal Mirror," *Physical Review Letters,* vol. 98, p. 104301, March 1, 2007 2007.

[109] S. D. Cohen, H. L. D. de S. Cavalcante, and D. J. Gauthier, "Subwavelength Position Sensing Using Nonlinear Feedback and Wave Chaos," *Physical Review Letters,* vol. 107, p. 254103, December 1, 2011 2011.

[110] A. S. Gliozzi, M. Griffa, and M. Scalerandi, "Efficiency of time-reversed acoustics for nonlinear damage detection in solids," *The Journal of the Acoustical Society of America,* vol. 120, pp. 2506-2517, 2006.

[111] S. K. Hong, V. M. Mendez, T. Koch, W. S. Wall, and S. M. Anlage, "Nonlinear electromagnetic time reversal in an open semireverberant system," *Physical Review Applied,* vol. 2, p. 044013, 2014.

[112] S. M. Anlage, J. Rodgers, S. Hemmady, J. Hart, T. M. Antonsen, and E. Ott, "New Results in Chaotic Time-Reversed Electromagnetics: High Frequency One-Recording-Channel Time-Reversal Mirror," *Acta Physica Polonica A,* vol. 112, p. 569, October 1, 2007 2007.

[113] M. Frazier, B. Taddese, T. Antonsen, and S. M. Anlage, "Nonlinear Time Reversal in a Wave Chaotic System," *Physical Review Letters,* vol. 110, Feb 7 2013.

[114] X. Xu, H. Liu, and L. V. Wang, "Time-reversed ultrasonically encoded optical focusing into scattering media," *Nature photonics,* vol. 5, pp. 154-157, 2011.

[115] Y. M. Wang, B. Judkewitz, C. A. DiMarzio, and C. Yang, "Deep-tissue focal fluorescence imaging with digitally time-reversed ultrasound-encoded light," *Nature communications,* vol. 3, p. 928, 2012.

[116] *Normal CT of the neck*. Available: https://radiopaedia.org/cases/normal-ct-of-the-neck

[117] S. Park, J. Nyenhuis, C. Smith, E. Lim, K. Foster, K. Baker, G. Hrdlicka, A. Rezai, P. Ruggieri, and A. Sharan, "Gelled versus nongelled phantom material for measurement of MRI-induced temperature increases with bioimplants," *IEEE transactions on magnetics,* vol. 39, pp. 3367-3371, 2003.

[118] F. Cangialosi, T. Grover, P. Healey, T. Furman, A. Simon, and S. M. Anlage, "Time reversed electromagnetic wave propagation as a novel method of wireless power transfer," in *2016 IEEE Wireless Power Transfer Conference (WPTC)*, 2016, pp. 1-4.

[119] T. Ta and T. M. Porter, "Thermosensitive liposomes for localized delivery and triggered release of chemotherapy," *Journal of controlled release,* vol. 169, pp. 112-125, 2013.

[120] O. Taratula, A. Kuzmov, M. Shah, O. B. Garbuzenko, and T. Minko, "Nanostructured lipid carriers as multifunctional nanomedicine platform for pulmonary co-delivery of anticancer drugs and siRNA," *Journal of Controlled Release,* vol. 171, pp. 349-357, 2013.

[121] H. Oliveira, E. Pérez-Andrés, J. Thevenot, O. Sandre, E. Berra, and S. Lecommandoux, "Magnetic field triggered drug release from polymersomes for cancer therapeutics," *Journal of Controlled Release,* vol. 169, pp. 165-170, 2013.

Appendix: TE_z - TM_z Decomposition

In a homogeneous source-free region, the field satisfies the Maxwell's equation,

$$\begin{aligned} \nabla \times \mathbf{E} &= -j\omega\mu\mathbf{H} \\ \nabla \times \mathbf{H} &= j\omega\varepsilon\mathbf{E} \\ \nabla \cdot \mathbf{E} &= 0 \\ \nabla \cdot \mathbf{H} &= 0. \end{aligned} \tag{A.1}$$

Assume we express part of the field in terms of a magnetic vector potential **A** and the rest of the field in terms of an electric vector potential **F**, the general equation of the vector potentials are derived as

$$\begin{aligned} \mathbf{E} &= \frac{1}{j\omega\varepsilon}\nabla \times \left(\frac{1}{\mu}\nabla \times \mathbf{A}\right) - \frac{1}{\varepsilon}\nabla \times \mathbf{F} \\ \mathbf{H} &= \frac{1}{\mu}\nabla \times \mathbf{A} - \frac{1}{j\omega\mu}\nabla \times \left(-\frac{1}{\varepsilon}\nabla \times \mathbf{F}\right). \end{aligned} \tag{A.2}$$

Choose Lorenz Gauge, the equations reduce to

$$\begin{aligned} \nabla^2\mathbf{A} + k^2\mathbf{A} &= 0 \\ \nabla^2\mathbf{F} + k^2\mathbf{F} &= 0. \end{aligned} \tag{A.3}$$

Each rectangular components satisfy the scalar Helmholtz equation,

$$\nabla^2\psi + k^2\psi = 0\,. \tag{A.4}$$

If we take **F** = 0 and

$$\psi = A_z\,. \tag{A.5}$$

The fields can be found in the cylindrical coordinates shown as

$$
\begin{aligned}
E_z &= \frac{1}{j\omega\mu\varepsilon}\left(\frac{\partial^2}{\partial z^2}+k^2\right)\psi & H_z &= 0 \\
E_\rho &= \frac{1}{j\omega\mu\varepsilon}\frac{\partial^2\psi}{\partial\rho\partial z} & H_\rho &= \frac{1}{\mu\rho}\frac{\partial\psi}{\partial\phi} \\
E_\phi &= \frac{1}{j\omega\mu\varepsilon\rho}\frac{\partial^2\psi}{\partial\phi\partial z} & H_\phi &= -\frac{1}{\mu}\frac{\partial\psi}{\partial\rho}.
\end{aligned}
\tag{A.6}
$$

The fields have no H_z component, which is called transverse magnetic to z (TM_z).

According to duality, if we choose $\mathbf{A} = 0$ and

$$\psi = F_z . \tag{A.7}$$

The fields in the cylindrical coordinates are expressed as

$$
\begin{aligned}
H_z &= \frac{1}{j\omega\mu\varepsilon}\left(\frac{\partial^2}{\partial z^2}+k^2\right)\psi & E_z &= 0 \\
H_\rho &= \frac{1}{j\omega\mu\varepsilon}\frac{\partial^2\psi}{\partial\rho\partial z} & E_\rho &= -\frac{1}{\varepsilon\rho}\frac{\partial\psi}{\partial\phi} \\
H_\phi &= \frac{1}{j\omega\mu\varepsilon\rho}\frac{\partial^2\psi}{\partial\phi\partial z} & E_\phi &= \frac{1}{\varepsilon}\frac{\partial\psi}{\partial\rho}.
\end{aligned}
\tag{A.8}
$$

The fields have no E_z component, which is called transverse electric to z (TE_z).

An arbitrary field in a homogeneous source-free region can be expressed as the combination of a TM field and a TE field. Hence by choosing wisely the z direction, any EM problem in a source-free region reduces to solving two scalar Helmholtz equations, one for TM_z, the other for TE_z. The decomposition gives us a systematic way to solve the EM fields in a homogeneous source-free region.